The Sentinel-Arlington Volcanic Field, Arizona

by

Shelby Renee Cave

A Dissertation Presented in Partial Fulfillment
of the Requirements for the Degree
Doctor of Philosophy

Approved April 2015 by the
Graduate Supervisory Committee:

Amanda Clarke, Chair
Donald Burt
Stephen Reynolds
Mark Schmeeckle
Steven Semken

ARIZONA STATE UNIVERSITY

May 2015

ABSTRACT

The Sentinel-Arlington Volcanic Field (SAVF) is the Sentinel Plains lava field and associated volcanic edifices of late Cenozoic alkali olivine basaltic lava flows and minor tephra deposits near the Gila Bend and Painted Rock Mountains, 65 km-100km southwest of Phoenix, Arizona. The SAVF covers ~600 km^2 and consists of 21+ volcanic centers, primarily low shield volcanoes ranging from 4-6 km in diameter and 30-200 m in height. The SAVF represents plains-style volcanism, an emplacement style and effusion rate intermediate between flood volcanism and large shield-building volcanism. Because of these characteristics, SAVF is a good analogue to small-volume effusive volcanic centers on Mars, such as those seen the southern flank of Pavonis Mons and in the Tempe Terra region of Mars. The eruptive history of the volcanic field is established through detailed geologic map supplemented by geochemical, paleomagnetic, and geochronological analysis.

Paleomagnetic analyses were completed on 473 oriented core samples from 58 sites. Mean inclination and declination directions were calculated from 8-12 samples at each site. Fifty sites revealed well-grouped natural remanent magnetization vectors after applying alternating field demagnetization. Thirty-nine sites had reversed polarity, eleven had normal polarity. Fifteen unique paleosecular variation inclination and declination directions were identified, six were represented by more than one site with resultant vectors that correlated within a 95% confidence interval. Four reversed sites were radiometrically dated to the Matuyama Chron with ages ranging from 1.08 ± 0.15 Ma to 2.37 ± 0.02 Ma; and one normal polarity site was dated to the Olduvai normal excursion at 1.91 ± 0.59 Ma. Paleomagnetic correlations within a 95% confidence interval were used to extrapolate radiogenic dates. Results reveal 3-5 eruptive stages over ~1.5 Ma in the early Pleistocene and that the SAVF dammed and possibly diverted the lower Gila River multiple times. Preliminary modeling of the median clast size of the terrace deposits suggests a maximum discharge of ~11300 cms (~400,000 cfs) was necessary to transport observed sediment load, which is larger than the historically recorded discharge of the modern Gila River.

DEDICATION

In memory of Dr. Ronald Greeley, who originally steered me towards researching the Sentinel-Arlington Volcanic Field as a terrestrial analog for planetary volcanism. Ron taught me many things about good geological mapping, how to approach a scientific problem in a clear, concise, and intellectually rigorous manner, and the difference between activity and achievement. I would like to also acknowledge the grace and dignity of Cindy Greeley in helping Ron watch after his extensive student 'family'.

ACKNOWLEDGEMENTS

There are many people I would like to thank for their help and support. I would like to thank my parents, friends, and fiancé for their constant and unwavering support and encouragement. This project would never have been published without them and I will always be grateful. I need to acknowledge the gracious support and intellectual involvement of my advisor, Dr. Amanda Clarke, and my doctoral supervisory committee, Drs. Don Burt, Mark Schmeeckle, Stephen Reynolds, and Steve Semken. I would also like to thank the Arizona Geological Survey for support, especially Dr. Jon Spencer. I would like to thank the United States Geologic Survey at Menlo Park Rock Magnetics Laboratory for support and granting access to their facility, especially Dr. Duane Champion. I would like to thank the members of the Planetary Geology Group (PGG) at the School of Earth and Space Exploration (SESE) at Arizona State University that intellectually and logistically supported this project with their many talents, especially Dr. Jacob Bleacher, Dr. Dave Williams, Stephanie Holaday, Charles Bradbury, and Dan Ball. I would like to also thank the members of the PGG group and SESE community at large who ventured out into the field with me, including Shane Thompson, Dr. Rachael Teasdale, Ramses Ramirez, Jennifer McNeil, and Zackary Bowles. I would like to also thank the National Speleological Society Central Arizona Grotto for also supporting field components of this project. Personnel at the Barry M. Goldwater Air Force Range granted access, safety training and support with professionalism and alacrity for mapping the region of the SAVF that is on the active bombing range, and the U.S. Army Corp of Engineers dam keepers were a pleasure to work with while mapping the region of SAVF in the Painted Rock Reservoir area. I will always remember morning coffee and conversation year after year with Sandy and Bob, the delightful BLM campground hosts at the Painted Rock Campground. Many private property landowners granted me access (and watched after me) along the Gila and Hassayampa River areas, especially the De La Peña's and the Gable's. This project was partially funded by the NASA Planetary Geology and Geophysics Grant, the Townsend Endowment, and Freeport-McMoRan Copper & Gold, Inc.

TABLE OF CONTENTS

Page

LIST OF FIGURES ---------- V

CHAPTER

1 INTRODUCTION ---------- 1

PREVIOUS INVESTIGATIONS---------- 1

GEOLOGIC SETTING ---------- 2

2 GEOLOGIC MAP ---------- 6

UNIT DESCRIPTIONS---------- 6

STRUCTURE ---------- 9

3 PHYSICAL VOLCANOLOGY ---------- 17

4 PALEOMAGNETISM AND RADIOGENIC DATING ---------- 29

METHODS ---------- 30

RESULTS ---------- 34

5 PALEOHYDROLOGY OF LOWER GILA RIVER ---------- 41

METHODS ---------- 41

RESULTS ---------- 45

6 SUMMARY AND CONCLUSIONS ---------- 56

REFERENCES ---------- 58

APENDICES

A – PALEOMAGNETIC DATA TABLE ---------- 64

B – AGE SPECTRA AND ISOCHRON PLOTS ---------- 67

C – $^{40}AR/^{39}AR$ GEOCHROOLOGY RESULTS FROM SOUTHWESTERN ARIZONA BASALTS--70

D - CIPW NORM AND VISCOSITY CALCULATIONS FROM XFR RESULTS ----------82

LIST OF FIGURES

Figure Page

1. PLAINS-STYLE VOLCANISM ---------- 1
2. SIMPLIFIED PHASE DIAGRAMS FOR THE THREE PRIMARY MECHANISMS THAT CAN FORM PARTIAL MELT FROM PERIDOTITE IN THE UPPER MANTLE----------4
3. LOCATION MAP AND 1:100,000 GEOLOGIC MAP---------- 6
4. HEIGHT TO DIAMETER PLOTS FOR LOW SHIELD VOLCANOS IN THE SAVF----------19
5. PLOT OF PERCENTAGE VERSES COUNT OF BINNED SLOPE VALUES FOR EACH LOW SHIELD ---------- 19
6. AERIAL PHOTOGRAPHS OF LOW SHIELD SUMMIT TYPES ---------- 20
7. CROSS-SECTIONS OF LOW SHIELD SUMMIT TYPES ---------- 20
8. XRF ANALYSES OF THE SAVF ---------- 21
9. XRF ANALYSES OF A SINGLE MONOGENETIC SAVF EDIFICE AND OF TERTIARY CINDER CONE ON EDGE OF SAVF ---------- 25
10. BASE ELONGATION OF SUMMIT AND MIDFLANK REGIONS OF SAVF LOW SHIELD VOLCANOES ---------- 26
11. SAVF VENT ALIGNMENTS ---------- 26
12. PALEOMAGNETIC DATA COLLECTION SI---------- 28
13. THE RESULTANT PALEO-MAGNETIC VECTORS FOR EACH SAMPLING SITE DISPLAYED WITHIN THEIR RESPECTIVE A_{95} CONFIDENCE INTERVALS ---------- 28
14. SAVF AR-AR DATES PLOTTED ON PLEISTOCENE POLARITY SCALE ---------- 31
15. PSV VECTOR PLOTS AND MAP OF SELECTED CORRELATIVE VOLCANIC EVENTS --35
16. DRAINAGE BASIN AND LONGITUDINAL PROFILE OF THE GILA RIVER ---------- 37
17. SAVF LAVA DAMS MAP ---------- 39
18. LOCATION AND CROSS-SECTIONAL PROFILE OF CANYON GEOMETRY USED IN RECONSTRUCTIONS ---------- 42

19. PALEOCHANNELS OF THE LOWER GILA RIVER PRESERVED BY THE SAVF ---------- 44
20. POSSIBLE PALEOLAKES ON THE LOWER GILA RIVER CAUSED BY LAVA DAMS FROM THE SAVF ---------- 47

LIST OF TABLES

Table Page

1. XFR SAMPLE LOCATIONS ---------- 22

2. XRF RESULTS FOR SAVF ----------23

Chapter 1

INTRODUCTION

The location and scale of basaltic volcanic fields can reveal information about magma source zone and local tectonic setting. Basaltic magmas have been shown from laboratory experiments to be potentially derived from mantle peridotite through partial melts (Wyllie, 1984). Alkalic basaltic magmas often contain xenoliths of peridotite and other mantle rocks. Shear waves transmit through the mantle indicating it is not molten, but partial melts of the peridotite mixture can initiate in three basic ways (Figure 1) increased heat transfer, decrease in over-riding lithostatic pressure (adiabatic decompression beneath mid-ocean ridges or in mantle plumes), and volatile infusion, particularly H_2O in subduction zones. Peridotite is a mixture so the components will melt at different temperatures. The partial melt coalesces and rises buoyantly. Partial melt often forms from an upwelling of solid but ductily behaving mantle, often beneath zones of active or passive crustal extension; in zones of shear or in response to convective heating; in relation to influx of mantle fluids; or some combination of the above.

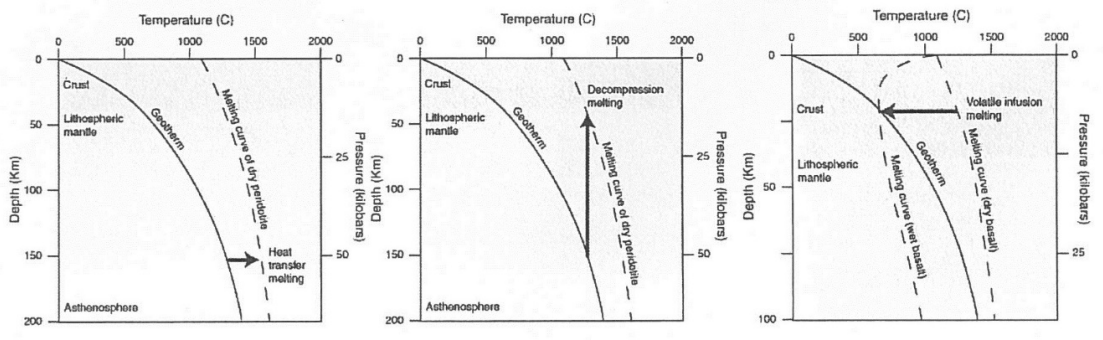


Figure 1: Simplified phase diagrams for the three primary mechanisms that can form partial melt from peridotite in the upper mantle: increased heat transfer, adiabatic decompression, or volatile infusion (adapted from Marshak, 2004).

The tectonic setting of most intraplate alkaline magmatism is in extensional regimes (i.e., such as abortive rifting, successful rifting, broad extensional regimes, back arc) and hotspots

(Sørensen, 1974). Basaltic eruptions are typically 1100° C or higher, indicating a probable mantle source based on current understanding of the thermal gradients of the crust and upper mantle. The volumes are normally relatively small. There are no recognized Archean alkaline rocks, though there are numerous Proterozoic examples starting at ~1.2 Ga (Philpotts, 1990). Formation of volcanic fields verses central volcanoes from low rates of magma production in areas of high rates of extension (Conner and Conway, 2000).

Extrusive igneous rocks represent the late stage of a long history of magma melt, transport, differentiation, country rock assimilation, and eruption. Eruptive style and resultant edifice types are further influenced by inter-related eruption processes. Major basaltic terranes include: 1) flood basalt plateaus with possibly very high rates of effusion, linear vent systems and flows great than 10-30 m thick and covering 5-10 km3; 2) and large shield volcanoes with a single central vent and low rates of effusion, lava flows typically 3-5 m thick, and extensive lava tube systems; and 3) 'plains-style' volcanism with moderate effusion rates that combines elements of both flood basalts and large shield volcanoes (Greeley, 1977; Greeley, 1982). The type locality of 'plains-style' volcanism is the Eastern Snake River Plain, Idaho, and is composed of plains of coalescing low shield volcanoes, fissure flows, and lava tube networks. Low shield volcanoes have a very low aspect (height to diameter) ratios even compared to large shield volcanoes (following examples as measured for this thesis):

Average aspect ratio for Hawai'i large shield volcanoes:	0.254
Average aspect ratio for Eastern Snake River Plain low shield volcanoes:	0.013
Average aspect ratio for Sentinel-Arlington Volcanic Field low shield volcanoes:	0.012

Low shield volcanoes can have a small crater or cinder cone at the summit, typically have volumes less than 5-10 km^3, and diameter of 5-15 km. Low shield often align along vent in rift zones (Greeley, 1977; Greeley, 1982). Sentinel-Arlington Volcanic Field represents 'plains-style'

volcanism, but with less fissure fed eruptions and tensional fractures as compared to ESRP (Please see chapter for more in depth discussion of 'plains-style' volcanism).

The Sentinel Plains lava field and associated small shields are early Pleistocene-age, mantle-derived alkali olivine basaltic lavas in the vicinity of the Gila Bend and Painted Rock Mountains, 65 km to 100 km southwest of Phoenix, Arizona (Figure 1). These volcanic centers are collectively referred to as the Sentinel-Arlington Volcanic Field (SAVF). The SAVF covers ~600 km^2 and consists of more than 2 dozen volcanic centers ranging from 4-6 km in diameter and 30-200 m in height. The lavas are partially eroded and dissected by peripheral ephemeral washes, the Hassayampa River, and the Gila River, as well as lightly mantled by aeolian dust, pedogenic calcium carbonate, and basaltic rubble, with a few areas covered by alluvium.

PREVIOUS INVESTIGATIONS

The Sentinel-Arlington Volcanic Field has been mapped at 1:1,000,000 scale on the geologic map of Arizona (Richard et al., 2000; Reynolds, 1988); 1:375,000 scale on Maricopa and Yuma county maps (Wilson et al., 1960; Wilson et al., 1957); and 1:100,000 scale on 30' by 60' quadrangle geologic and surficial maps (Spencer, 1995; Reynolds and Scotnicki, 1993; Demsey, 1990, 1989). Several peripheral low shields were partially mapped at 1:50,000 to 1:24,000 scale (Scotnicki 1994, 1993a, 1993b; Peterson et al., 1989). The Sentinel Plains and the Warford Ranch, Woolsey, Gillespie, and Arlington small shields were dated as Pliocene to early Pleistocene by K-Ar methods in the late 1970's (Reynolds et al., 1986; Shafiquallah et al., 1980; Schoustra et al., 1976; Spencer, 2013), though the data often exhibit a range of 2-3 Ma for the same lava flow or a single edifice assumed to be monogenetic due to lack of intercalated paleosols or weathering horizons between units (Cave, 2004; Cave and Greeley, 2004; Cave et al., 2007; Greeley and Cave, 2007). The Sentinel Plains and the associated low shields were mentioned briefly in descriptions of Arizona

Cenozoic tectonism and/or volcanism (Lynch, 1989; Reynolds et al., 1986; Morrison, 1985; Damon et al., 1984; Lee and Bell, 1975).

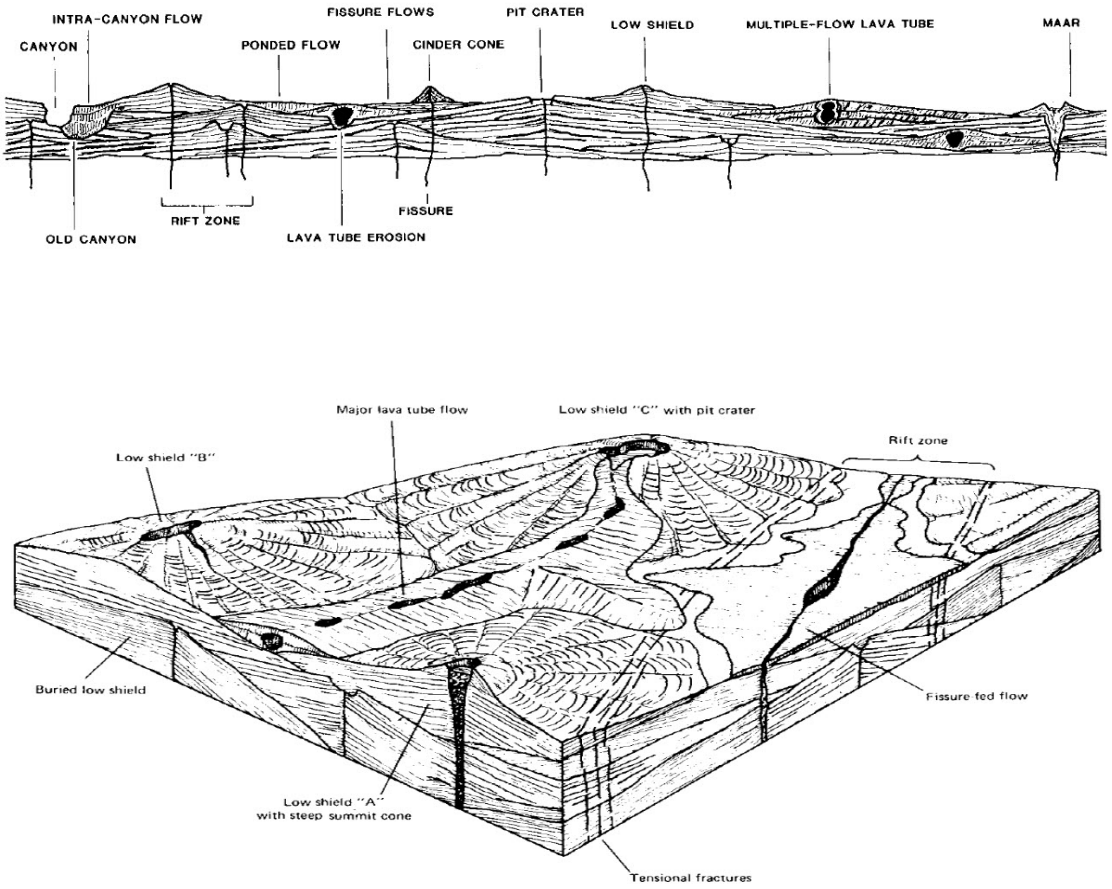


Figure 2: Upper: Vertically exaggerated schematic cross-section of major features of basaltic "plains" style volcanism, as characterized by Greeley (1982) in Eastern Snake River Plain, Idaho. The majority of the lava flows is typically pahoehoe and seldom exceed ~10 m in thickness except where ponded in topographic lows. The Sentinel-Arlington Volcanic Field exhibits the same style of volcanism, but over a smaller area and cumulative thickness, and the flows have been subsequently weathered, incised, and mantled by aeolian fines and discontinuous alluvium. Lower:

Block diagram showing typical development of terrain in basaltic "plains" style volcanism as characterized by Greeley (1982) in the eastern Snake River Plain, Idaho.

GEOLOGIC SETTING

SAVF lies on the eastern terminus of the Gila River trough (Eberly and Stanley, 1978). Northwest trending normal faults cut the surrounding terrain (Richard et al., 2000; Skotnicki, 1993a, 1993b, 1994; Reynolds and Scotnicki, 1993; Reynolds, 1988; Scarborough et al., 1986). SAVF potentially represents basaltic plains-style volcanism (Greeley, 1982, 1977), an emplacement style of volcanism intermediate between classic flood volcanism and large shield-building volcanism (Figure 2). The SAVF basal contact rests on mid-Tertiary volcanic deposits in the Painted Rock and Gila Bend Mountains, alluvium, alluvial/colluvial pediment deposits, or on a QTg gravel terrace in lower elevations. The latter is typically a conglomerate of rounded polymictic gravels and cobbles, with laminar interstitial calcrete cementing and partially brecciating the clasts (similar to Stage IV calcrete morphologic development of Machette, 1985; Bachman and Machette, 1977; after Gile et al., 1966). The basal contact is up to ~30 m above the modern Gila River channel. K-Ar and $^{40}Ar/^{39}Ar$ dating indicate the field is ~1-3 Ma in age (Table 1; Spencer, 2013; Cave et al., 2007).

Recent studies of young mafic volcanism in the southwestern United States patterns of deep to moderate source regions driving volcanism through decompression melting of a chemical boundary laye, or related to localized lithospheric thinning and extension accompanying foundering of the lithosphere (Gogus and Pysklywec, 2008; Reid et al., 2012) possibly influenced by edge effects and local convection from lithospheric removal (Allison et al., 2013).

Chapter 2

GEOLOGIC MAP

The Sentinal-Arlington Volcanic Field was mapped at 1:10,000 scale from 2002-2006. It was distinguished from previous Tertiary basaltic terrains in the region by similar eruptive style, landscape degradation, and lack of obvious tectonic tilting or disruption. Please see Figure 3 for location map and 1:100,000 geologic map: http://repository.azgs.az.gov/sites/default/files/dlio/files/nid1587/cm-14-a_sentinel-arlington_volcanic_field_v1.00_map_250dpi.pdf

GENERAL UNIT DESCRIPTIONS

EXTRUSIVE AND HYPABYSSAL IGNEOUS ROCKS

SUMMIT REGION LAVA FLOWS AND TEPHRA DEPOSITS

Description: Summit regions are defined by a distinct surface texture in the aerial photographs that corresponds to a steeper surface gradient (typically >6°); conical and radial, 0.5 m to 1.5 m thick, sub-vertical dikes, often exposed at up to 2-3 m positive relief; relatively short, thin lava flows 0.5 to 2 m thick; and limited exposures of oxidized spatter or tephra. Summit regions typical have 1 to 2 mm phenocrysts of needle-like, translucent plagioclase feldspar.

Interpretation: Possible extent of pyroclastic deposits and shelly pahoehoe lava flows that have been weathered, often revealing the vent-area feeder dikes.

MIDFLANK LAVA FLOWS

Description: The midflank stratigraphic units are composed of lava flows with moderate surface angles and occasional relict flow festooning at 25 m to 75 m spacing that is visible in aerial photographs. There are rare skylights formed from collapse of partially drained lava tubes.

Interpretation: The midflank units are interpreted to be an accumulation of edifice-building lava flows. The majority of these flows are interpreted to be typically pahoehoe flows, with some a'a flows (sometimes with transverse flow buckling) where flows encountered steep paleoslopes or pre-existing topographic barriers during emplacement that caused the flows to at least locally have evidence of higher internal shear.

DISTAL LAVA FLOWS

Description: The lowest stratigraphic units are broad, flat (>2° grade) lava flows forming the base of the shields. In the very flat topographic saddles between shields there are typically 5 to 8 m high hills and ridges as well as circular high-albedo features ~20 m in diameter. The distal units are usually 3 to 8 m thick, with a 0.5 m frothy vesicular capping layer underlain by a massive interior with dispersed vesicles, vesicle pipes, and discontinuous basal breccias. Where the distal units are ponded in pre-existing topographic lows they can be 10-12 m thick and form 0.5 to 1 m diameter columnar jointing, with rare basal palagonitic rinds and sub-meter pillow lavas. Cross-sectional exposures of distal units also reveal rare 1 to 2 m diameter lava tubes (typically completely filled with cooled lava).

Interpretation: The distal units are interpreted to be degassed pahoehoe lava flows fed by a system of lava-tube conduits. This unit can develop inflationary features such as tumuli, pressure ridges, and collapse pits when crossing very flat regions. Along the margins of the field where these flows are deposited onto alluvium and not subsequently capped by later lava flows, they often typically exhibit reverse topography. In areas where the original flows form long thin fingers of lava, with a high length to width ratio in plan view (indicating that it may have followed a pre-existing surface drainage and a topographic low) it now typically creates a ridgeline

as the surrounding base level drops and the less resistant alluvium weathers away or deflates, leaving the lava flow as a more-resistant topographic high.

KIPUKAS

Description: Completely embayed basaltic islands with textures, phenocryst assemblages, etc., that do not match the embaying lava flow.

Interpretation: Underlying basaltic units that can represent a pre-existing SAVF volcanic unit or an older Miocene to Pliocene-age basaltic remnant.

LATE TERTIARY BASALTIC ROCKS AND CINDER DEPOSITS

Description: Dark-gray, fine-grained basaltic lava flows and rare welded agglutinate and tephra deposits that have not been tectonically altered (unlike the faulted Miocene basaltic units of the Painted Rock Mountains). Typically exhibits vesicular flow exteriors and massive or vuggy interiors, typically porphyritic with varying phenocryst assemblages, rarely exhibits diktytaxitic texture.

Interpretation: Very dissected Pliocene-age (?) cinder cones and lava flows.

SEDIMENTARY UNITS

MANTLING FINES

Description: Silt and clay, sometimes indurated by pedogenic calcium carbonate.

Interpretation: Aeolian fines and locally derived clays, sometimes asymmetrically accumulated on edifice related to dominant wind patterns, with varying stages of pedogenic calcium carbonate accumulation. Often an active component of desert pavement, and clay swelling may slowly loft surface basalt rubble as mantle accumulates (Anderson et al., 2002; Wells et al., 1985, Gile et al., 1966).

SURFICIAL DEPOSITS

Description: Sand and sub-angular polymictic gravel on top of SAVF basaltic units.

Interpretation: Pleistocene-Holocene alluvial cover, including both active washes and some reworked stranded deposits from the Hassayampa and Gila Rivers.

GILA RIVER GRAVELS

Description: Rounded polymictic gravel and cobble-sized river gravels and polymictic conglomerates cemented by laminar interstitial calcrete at base of the SAVF or forming heavily-varnished lag terraces ~15 to 30 m above current river channel bottom.

Interpretation: Paleo-channel terraces of the Gila River.

STRUCTURE

SAVF lava flows exhibit no obvious tectonic post-emplacement offset, though there are strong NW-trending erosional re-entrants that correspond to mapped faults in nearby terrain. Also SAVF vent locations sometimes exhibit NE or NW alignment, especially in the Oatman and Painted Rock Mountains pediment areas. This alignment could potentially represent the influence of pre-existing structures crossing the underlying bedrock, similar to structural control of vent alignments observed in other basaltic fields in Arizona (Conway et al., 1997; Crumpler et al., 1994; Connor et al., 1992).

SPECIFIC UNIT DESCRIPTIONS

Qo Surficial deposits - Pleistocene-Holocene alluvial cover overlying SAVF units

Qba Tephra deposits - Remnant basaltic ash, lapilli and cinder as intercalated lenses or remnant phreatomagmatic cones and cinder cones.

QBSNs Sentinel Peak low shield secondary vent summit - Basaltic pahoehoe flows and near-vent pyroclastic deposits and intercalated tephra deposits with 6º-22º slope angle of the secondary Sentinel Peak vent +/- radial and concentric feeder dikes

QbSSs	Sentinel Peak low shield summit - Basaltic pahoehoe flows and near-vent pyroclastic deposits and intercalated tephra deposits with 6º-22º slope angle of the Sentinel Peak vent +/- radial and concentric feeder dikes
QbSSm	Sentinel Peak low shield midflank - Basaltic pahoehoe flows with ~2º-5º slope of the Sentinel Peak vent
QbSSd	Sentinel Peak low shield distal - Basaltic pahoehoe flows of the Sentinel Peak vent with <0-2º slope angle and alluvial cover
QbMLs	Malpais low shield summit - Basaltic pahoehoe flows and near-vent pyroclastic deposits and intercalated tephra deposits with 6º-22º slope angle +/- radial and concentric feeder dikes of the Malpais vent
QbMLm	Malpais low shield midflank - Basaltic pahoehoe flows with ~2º-5º slope of the Malpais vent, 40Ar/39Ar radiogenic age of 1.08 ± 0.15 Ma
QbMld	Malpais low shield distal - Basaltic pahoehoe flows of the Malpais vent with <0-2º slope angle
QbSEd	Sent 774 low shield distal - Basaltic pahoehoe flows with ~0º-5º slope of the Sent 774 vent, possible fissure style eruption, very low aspect ratio, lacking typical low shield edifice
QbMEs	Midway low shield secondary summit - Basaltic pahoehoe flows and near-vent pyroclastic deposits and intercalated tephra deposits with 6º-22º slope angle of the secondary Midway vent +/- radial and concentric feeder dikes
QbMWs	Midway low shield summit - Basaltic pahoehoe flows and near-vent pyroclastic deposits and intercalated tephra deposits with 6º-22º slope angle of the Midway vent +/- radial and concentric feeder dikes
QbMWm	Midway low shield midflank - Basaltic pahoehoe flows with ~2º-5º slope angle of the Midway vent

QbMWd Midway low shield distal - Basaltic pahoehoe flows of the Midway vent with <0-2º slope angle and possible alluvial cover

QbSTs Stanwix low shield summit - Basaltic pahoehoe flows and near-vent pyroclastic deposits and intercalated tephra deposits with 6º-22º slope angle of the Stanwix vent +/- radial and concentric feeder dikes

QbSTm Stanwix low shield midflank - Basaltic pahoehoe flows with ~2º-5º slope of the Stanwix vent

QbSTd Stanwix low shield distal - Basaltic pahoehoe flows of the Stanwix vent with <0-2º slope angle

QbCTs Control Tower low shield summit - Basaltic pahoehoe flows and near-vent pyroclastic deposits and intercalated tephra deposits with 6º-22º slope angle of the Control Tower vent +/- radial and concentric feeder dikes

QbCTm Control Tower low shield midflank - Basaltic pahoehoe flows with ~2º-5º slope of the Control Tower vent

QbCTd Control Tower low shield distal - Basaltic pahoehoe flows of the Control Tower vent with <0-2º slope angle and alluvial cover

QbWSs Wild Horse low shield secondary summit - Basaltic pahoehoe flows and near-vent pyroclastic deposits and intercalated tephra deposits with 6º-22º slope angle of the southeastern Wild Horse vent +/- radial and concentric feeder dikes

QbWNs Wild Horse low shield summit - Basaltic pahoehoe flows and near-vent pyroclastic deposits and intercalated tephra deposits with 6º-22º slope angle of the northwestern Wild Horse vent +/- radial and concentric feeder dikes, one dike 40Ar/39Ar radiogenically dated as 1.25 ± 0.024 Ma

QbWNm Wild Horse low shield midflank - Basaltic pahoehoe flows with ~2º-5º slope of the Wild Horse vent

QbWNd Wild Horse low shield distal - Basaltic pahoehoe flows of the Wild Horse vent with <0-2º slope angle and alluvial cover

QbTMs Ten Mile low shield summit - Basaltic pahoehoe flows and near-vent pyroclastic deposits and intercalated tephra deposits with 6º-22º slope angle of the Ten Mile vent +/- radial and concentric feeder dikes +- underlying tuff ring

QbTMm Ten Mile low shield midflank - Basaltic pahoehoe flows with ~2º-5º slope of the Ten Mile vent

QbTMd Ten Mile low shield distal - Basaltic pahoehoe flows of the Ten Mile vent with <0-2º slope angle and alluvial cover

QbTHs Theba low shield summit - Basaltic pahoehoe flows and near-vent pyroclastic deposits and intercalated tephra deposits with 6º-22º slope angle of the Theba vent +/- radial and concentric feeder dikes

QbTHm Theba low shield midflank - Basaltic pahoehoe flows with ~2º-5º slope of the Theba vent

QbTHd Theba low shield distal - Basaltic pahoehoe flows of the Theba vent with <0-2º slope angle and alluvial cover, 40Ar/39Ar radiogenically dated at 1.71 ± 0.054 Ma

QbTRs Tartron low shield summit - Basaltic pahoehoe flows and near-vent pyroclastic deposits and intercalated tephra deposits with 6º-22º slope angle of the Tartron vent +/- radial and concentric feeder dikes

QbTRm Tartron low shield midflank - Basaltic pahoehoe flows with ~2º-5º slope of the Tartron vent

QbTRd Tartron low shield distal - Basaltic pahoehoe flows of the Tartron vent with <0-2º slope angle and alluvial cover

QbWTs White Hills low shield summit - Basaltic pahoehoe flows and near-vent pyroclastic deposits and intercalated tephra deposits with 6º-22º slope angle of the White Hills vent +/- radial and concentric feeder dikes

QbWTm White Hills low shield midflank - Basaltic pahoehoe flows with ~2º-5º slope of the White Hills vent

QbBGs Black Gap low shield summit - Basaltic pahoehoe flows and near-vent pyroclastic deposits and intercalated tephra deposits with 6º-22º slope angle of the Black Gap vent +/- radial and concentric feeder dikes

QbBGm Black Gap low shield midflank - Basaltic pahoehoe flows with ~2º-5º slope of the Black Gap vent

QbSCm Sauceda tuff ring lava pond/flows - Late-stage basaltic lava flows and remnant lava pond partially covering or infilling the phreatomagmatic Sauceda tuff ring (most of the tuff deposit(s) subsequently weathered away)

QbWRs Warford Ranch low shield summit - Basaltic pahoehoe flows and near-vent pyroclastic deposits and intercalated tephra deposits with 6º-22º slope angle of the Warford Ranch vent +/- radial and concentric feeder dikes

QbWRm Warford Ranch low shield midflank - Basaltic pahoehoe flows with ~2º-5º slope of the Warford Ranch vent

QbWRd Warford Ranch low shield distal - Eroded and undercut basaltic pahoehoe flows of the Warford Ranch vent with <0-2º slope angle and possible alluvial cover

QbGLs Gillespie low shield summit - Basaltic pahoehoe flows and near-vent pyroclastic deposits and intercalated tephra deposits with 6º-22º slope angle of the Gillespie vent +/- radial and concentric feeder dikes

QbGLm Gillespie low shield midflank - Basaltic pahoehoe flows with ~2º-5º slope angle +/- possible festooned a'a flows around granitoid kipuka, of the Gillespie vent,

	the latter evidenced by partially concealed ~25 m to 75 m wavelength transverse flow buckling
QbGLd	Gillespie low shield distal - Basaltic pahoehoe flows of the Gillespie vent with <0-2º slope angle and alluvial cover
QbOVs	Overlook low shield summit - Basaltic pahoehoe flows and near-vent pyroclastic deposits and intercalated tephra deposits with 6º-22º slope angle of the Overlook vent +/- radial and concentric feeder dikes
QbOVm	Overlook low shield midflank - Basaltic pahoehoe flows with ~2º-5º slope of the Overlook vent
QbWLs	Woolsey low shield summit - Basaltic pahoehoe flows and near-vent pyroclastic deposits and intercalated tephra deposits with 6º-22º slope angle of the Woolsey vent +/- radial and concentric feeder dikes
QbWLm	Woolsey low shield midflank - Basaltic pahoehoe flows with ~2º-5º slope +/- possible a'a flows as evidenced by remnant ~10-50 m wavelength transverse buckling of the Woolsey vent
QbWLd	Woolsey low shield distal - Basaltic pahoehoe flows of the Wild Horse vent with <0-2º slope angle and possible alluvial cover
QbRTs	Radio Tower low shield summit - Basaltic pahoehoe flows and near-vent pyroclastic deposits and intercalated tephra deposits with 6º-22º slope angle of the Radio Tower vent +/- radial and concentric feeder dikes
QbRTm	Radio Tower low shield midflank - Basaltic pahoehoe flows with ~2º-5º slope of the Radio Tower vent
QBPSs	Painted Rock low shield secondary vent summit - Basaltic pahoehoe flows and near-vent pyroclastic deposits and intercalated tephra deposits with 6º-22º slope angle of the southern Painted Rock vent +/- radial and concentric feeder dikes

QbPNs Painted Rock low shield summit - Basaltic pahoehoe flows and near-vent pyroclastic deposits and intercalated tephra deposits with 6º-22º slope angle of the northern Painted Rock vent +/- radial and concentric feeder dikes, 40Ar/39Ar radiogenically dated at 1.91 ± 0.59 Ma

QbPNm Painted Rock low shield vent midflank - Basaltic pahoehoe flows with ~2º-5º slope angle of the northern Painted Rock vent

QbPNd Painted Rock low shield distal - Basaltic pahoehoe flows of the Painted Rock vent with <0-2º slope angle and alluvial cover

QbONs Oatman low shield secondary vent summit - Basaltic pahoehoe flows and near-vent pyroclastic deposits and intercalated tephra deposits with 6º-22º slope angle of the northern Oatman vent +/- radial and concentric feeder dikes

QbOSs Oatman low shield summit - Basaltic pahoehoe flows and near-vent pyroclastic deposits and intercalated tephra deposits with 6º-22º slope angle of the southern Oatman vent +/- radial and concentric feeder dikes

QbOSm Oatman low shield midflank - Basaltic pahoehoe flows with ~2º-5º slope angle of the southern Oatman vent

QbOTd Oatman low shield distal - Basaltic pahoehoe flows of the Oatman vent with <0-2º slope angle and alluvial cover

QbALd Arlington low shield distal - Basaltic pahoehoe flows of the Arlington vent with <0-2º slope angle and stranded alluvial cover on northern and southern flanks

QbALm Arlington low shield midflank - Basaltic pahoehoe flows with ~2º-5º slope angle +/- possible festooned a'a flows of the Arlington vent, the latter evidenced by partially concealed ~25 m to 75 m wavelength transverse flow buckling

QbALs Arlington low shield summit - Basaltic pahoehoe flows and near-vent pyroclastic deposits and intercalated tephra deposits of the Arlington vent with 6º-22º slope

	angle +/- radial and concentric feeder dikes, radiogenically dated as 2.37 +- 0.03 Ma
QTg	Gila River Gravels - Plio-Pleistocene Gila River deposits/terraces ~30 m above current river profile
Tb	Tertiary basaltic units - Basaltic to basaltic andesite tephra and lava

Chapter 3

PHYSICAL VOLCANOLOGY

Slope analysis was performed on the edifices of the Sentinel-Arlington Volcanic Field. Slopes were calculated from SRTM 1 arc-second data (30 m by 30 m), the slope values tallied, slope counts normalized to percentage of counts, and binned per whole degree increments. Margins were defined from geologic map. The slope calculations excluded canyons, distal erosional scarps, and kipukas.

The primary control on basaltic edifice style is viscosity. Viscosity is the property of a fluid that describes the rate at which deformation takes place when shear stress is applied, defined as shear stress divided by the rate of shear strain. Magma viscosity values are extremely important for emplacement rates, styles, and shapes of igneous bodies. A common range of viscosity values for erupting basalts at 1200° C are 10-100 Pa s (Shaw, 1969). More viscous flows tend to be shorter, stratigraphically thicker, and have smaller slow-length to flow width ratio. Less viscous flows tend to be longer, stratigraphically thinner, more controlled by pre-existing topography, and more likely to have digitate margins.

The most important factor influencing lava flow viscosity is temperature. Most basalts are erupted between approximately 1100° to 1250° C. Silicate melt viscosity is strongly dependent on composition, the most important component being SiO_2 (Wallace and Anderson, 2000). Basalt by definition is a mafic volcanic rock with weight percent of SiO_2 less than 52% typically with a mineral assemblage of olivine, pyroxene, and plagioclase feldspar with minor accessory phases. Sentinel-Arlington Volcanic Field has SiO_2 values ranging from 43 to 52 weight percent, with calculated of CIPW norm of olivine to alkali olivine basalt (Figure 7). Composition in turn can influence the behavior of crystals in the magma shifting the bulk composition. The amount of assimilation of wall rock and resultant changes to bulk composition that is possible by a magma depends on its thermal energy. Magmas above the liquidus can assimilate more material than magmas below the liquidus. Archean komatiites potentially could assimilate three times the crustal material as modern

basalts (Sparks, 1986). However, the heat required to raise wall rock temperature to melting point and supply the latent heat of fusion would come from crystallization of primary minerals in a subliquidus magma. Therefore large quantities of magma containing a large fraction of assimilated crust are unlikely (Philpotts, 1990).

The addition of dissolved H_20 decreases viscosity, probably because H_20 weakens or breaks apart the aluminosilicate framework of the melt (Shaw, 1972; Bottinga and Weill, 1972, Wallace and Anderson, 2000). Available experimental data suggests that dissolved CO_2 reduces the viscosity of silicate melts, but the effect is much smaller than for H_20 (Wallace and Anderson, 2000). Dissolved F is rare but when present (for example in certain topaz bearing rhyolites) it can a strong effect lowering the viscosity of silicate melts (Wallace and Anderson, 2000)

Most magmas above the liquidus behave as a Newtonian fluid. However, magmas begin to behave more like a Bingham fluid (i.e., resisting deformation until a minimum amount of shear strain is applied) the more entrained bubbles or suspended crystals are present (Shaw, 1969). However, when shear rates are increased sufficiently, bubbles can begin to deform and decrease viscosity, acting as internal slip faces. The boundary from non-deformable to deformable is a function of bubble radius. Small bubbles hold spheroidal shape at higher shear stress because the ratio of deforming forces to melt-vapor interfacial tension is lower (Spera, 2000).

The presence of different size fractions at a given volume fraction instead of a unimodal size distribution can result in a smaller increase in viscosity, as well as whether crystals are lath or equant-shaped, because smaller particles can fit between larger ones (Spera, 2000).

For basalts with viscosities of 10-15 Pa s behaving as a Newtonian fluid, conduit widths of 0.2 to 0.6 m are required to allow eruptions from depths down to 20 km and minimum corresponding eruption rates of 10-300 kg/s for isolated central conduits (BVSP, 1981). Rise speeds in the crust must be greater than 0.5 to 1 m/s to maintain relatively steady fire-fountaining (BVSP, 1981)

Planetary variables that can influence volcano morphology include gravity, planet size, mantle chemistry, atmospheres, the presence or absence of plate tectonics, and hydrospheres (Whitford-Stark, 1982). These can affect vertical stresses and lithospheric pressure within the mantle and crust, distribution of pyroclastic deposits, caldera collapse, and perhaps size, shape, and distribution of volcanic vents (Whitford-Stark, 1982). For example, asymmetric weathering of the Canary Island shield volcanoes from trade winds is thought to influence flank collapse and dormancy intervals (Schmincke, 2000).

RESULTS

The geologic map was supplemented by analyses to further define eruptive edifice style and eruptive history. These data include measuring aspect ratios, slope analysis, vent alignment and elongation measurements, and major and trace element chemistry in order to constrain viscosity and source characteristics

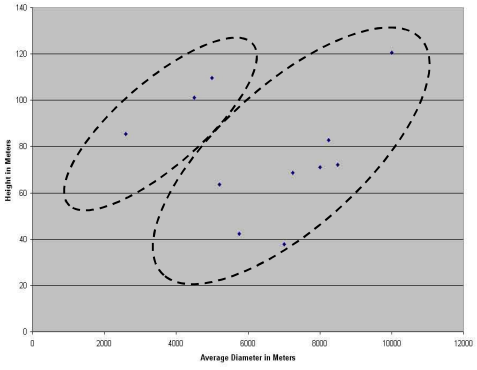


Figure 4: Height to diameter plots for low shield volcanoes in the Sentinel-Arlington Volcanic Field.

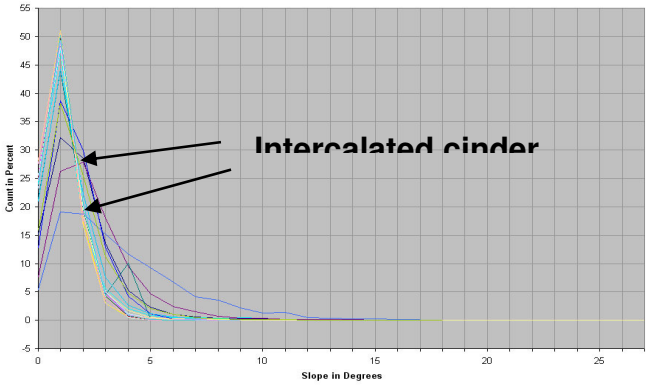


Figure 5: Plot of percentage verses count of binned slope values for each low shield in the Sentinel-Arlington Volcanic Field.

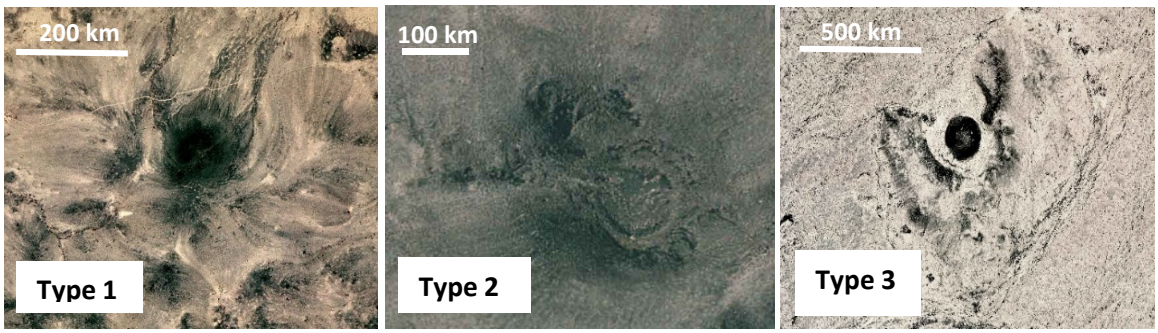


Figure 6: Aerial photographs of examples of low shield summit types, which include: Type 1: capped by thin lava flows (Sentinel LS); Type 2: eroded cinder deposits with limited spatter ramparts, and concentric and radial and feeder dikes exposed at positive relief (Arlington LS); and Type 3: rare phreatomagmatic tuff rings partially covered and preserved by lava flows (Sauceda tuff cone).

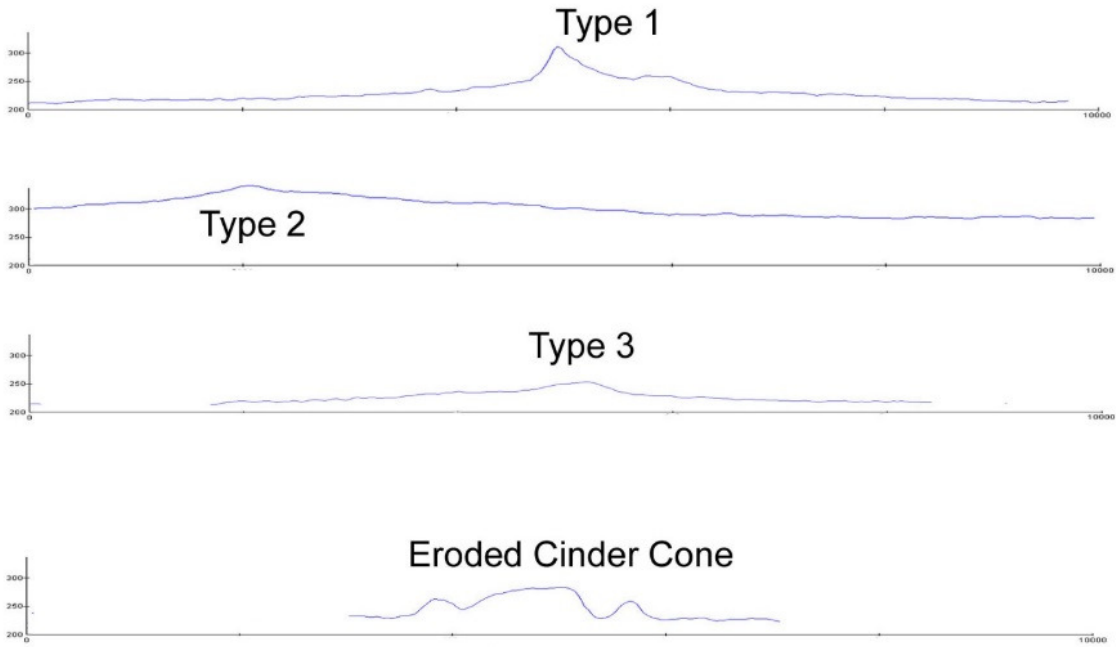


Figure 7: Cross-section of the three low shield volcano summit types at 5 times vertical exaggeration with an eroded Tertiary-age cinder cone for comparison.

Slope analysis revealed a very similar slope distribution for all of the low shields indicating summit types were most likely members of a continuum and not distinct eruptive style variations, with a possible influence from intercalated cinder deposits. Figure 6 and 7 show the three different summit and edifice types: Type 1) capped by thin lava flows (such as Sentinel low shield, Figure 3); Type 2) eroded cinder deposits with limited spatter ramparts, and concentric and radial and feeder dikes exposed at positive relief (such as Arlington low shield); and Type 3) rare phreatomagmatic tuff rings partially covered and preserved by lava flows (such as Sauceda tuff cone).

Geochemical X-ray flourence (XRF) data reveal most the SAVF lavas are alkaline olivine basalts (Figure 10, Appendix D). Viscosities and CIPW norm were calculated. (Appendix D).

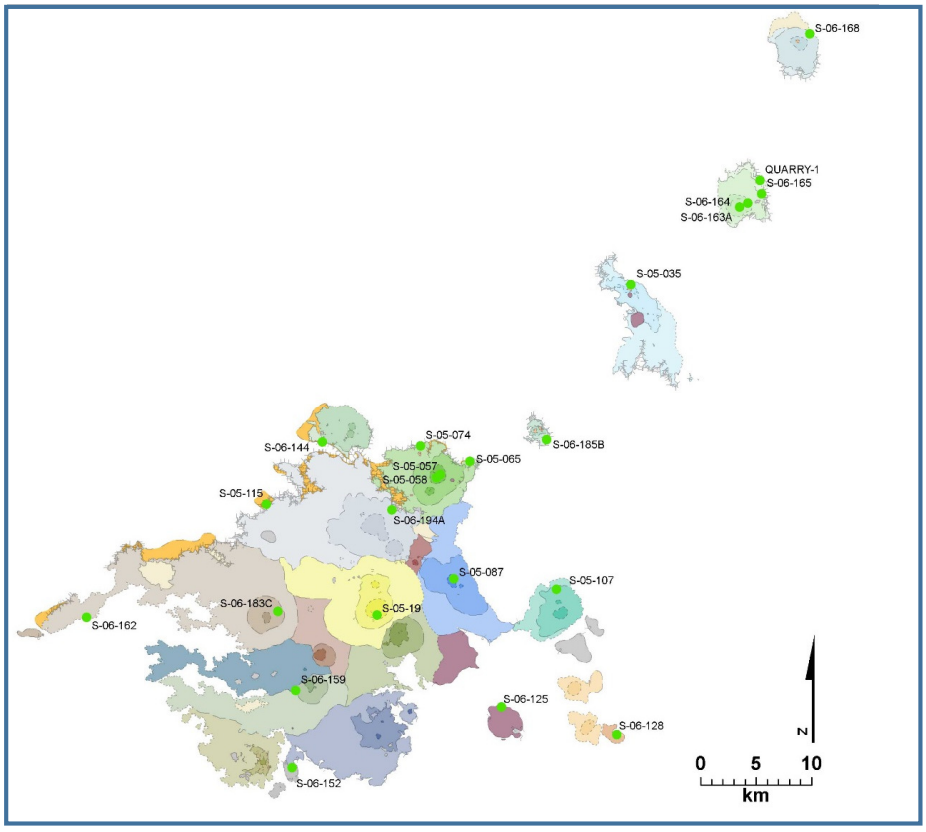


Figure 8: Location map of SAVF geochemical samples.

Sample ID	UTM NAD 27 E	UTM NAD 27 N	Low shield	Comment
S-05-035	322416	3669249	Woolsey	N summit flow scarp, mod vesicular (sanded)
S-05-057	304922	3651827	Painted Rock	Summit dike, disperse vesicles
S-05-058	305239	3652080	Painted Rock	N summit flow scarp, amygdaloidal, very vesicular
S-05-065	307898	3653272	Painted Rock	N distal flow, disperse vesicles
S-05-074	303466	3654657	Painted Rock	N distal flow, very vesicular
S-05-087	306452	3642709	Midway	N summit flow scarp, amygdaloidal, moderately vesicular (sanded)
S-05-107	315715	3641762	Theba	N distal flow, moderately vesicular
S-05-115	289602	3649422	Wild Horse	S bank of Gila River east of Sentinel Wash, very vesicular (sanded)
S-06-152	291898	3625721	Tby	Tertiary kipuka east of Ten Mile SS, gravel, disperse ves., (sanded)
S-06-159	292215	3632674	Stanwix	South distal flow, in wash north of Ten Mile SS, very vesicular, drill core
S-06-162	273394	3639244	Malpais	Western-most flow lobe N of Aztec Hills, amygdaloidal, mod to very ves.
S-06-163A	332198	3676215	Gillespie	SE summit, very vesicular, drill core
S-06-164	332918	3676574	Gillespie	N midflank, amygdaloidal, moderately vesicular (sanded)
S-06-165	334165	3677393	Gillespie	N distal flow, amygdaloidal, moderately vesicular (sanded)
S-06-168	338488	3691769	Arlington	N distal flow, amygdaloidal, moderately vesicular
QUARRY-1	334019	3678609	Gillespie	N distal flow, paleochannel, palagonite, moderately ves. (sanded)

Table 1: SAVF geochemical samples

	CAVS05 035	CAVS05 057	CAVS05 058	CAVS05 065	CAVS05 074	CAVS05 087	CAVS05 107	CAVS05 115	CAVS06 152	CAVS06 159	CAVS06 162	CAVS06 163A	CAVS06 164	CAVS06 165	CAVS06 168	CAVQUA RRY-1	CAVS06 164	CAVS06 164R
Date	6-Aug-06	6-Aug-06	6-Aug-06	6-Aug-06	6-Aug-06	6-Aug-06	6-Aug-06	6-Aug-06	6-Aug-06	6-Aug-06	6-Aug-06	6-Aug-06	6-Aug-06	6-Aug-06	6-Aug-06	6-Aug-06	6-Aug-06	6-Aug-06
SO3 >/=	0.07	0.12	0.15	0.10		0.05	0.07		0.16		0.08	0.29					0.02	0.02
	Unnormalized Major Elements (Weight %):										Unnormalized Major Elements (Weight %):							
SiO2	49.33	47.81	49.51	48.51	50.65	47.62	48.05	48.82	49.03	48.41	47.16	48.13	49.90	51.48	49.86	50.77	49.90	49.90
TiO2	2.097	2.416	1.796	1.739	1.509	2.573	1.764	1.781	1.726	1.538	1.388	1.807	1.900	1.746	2.258	1.746	1.900	1.903
Al2O3	14.27	15.79	14.33	13.87	15.05	16.67	13.80	14.61	13.96	15.47	14.61	13.79	14.40	14.02	14.36	14.17	14.40	14.45
FeO*	10.61	10.44	10.69	10.45	9.89	10.72	10.78	10.64	11.08	10.70	10.90	9.64	10.18	10.60	10.63	10.48	10.18	9.98
MnO	0.163	0.171	0.168	0.159	0.157	0.171	0.162	0.175	0.174	0.170	0.171	0.146	0.154	0.161	0.156	0.153	0.154	0.154
MgO	8.67	5.14	8.60	8.42	8.38	5.55	8.46	8.85	8.67	7.98	8.35	7.06	8.79	8.83	8.50	8.37	8.79	8.70
CaO	9.52	9.93	9.74	10.19	10.07	10.11	10.70	9.95	10.07	10.00	10.70	10.38	8.92	8.82	8.79	8.48	8.92	8.92
Na2O	3.23	3.77	3.07	2.95	2.91	3.73	2.94	3.11	3.02	3.21	3.12	3.05	3.13	3.01	3.26	2.46	3.13	3.14
K2O	0.99	1.43	0.85	0.76	0.49	1.49	0.76	0.90	0.74	0.78	0.58	0.73	1.00	0.47	0.87	0.53	1.00	1.01
P2O5	0.368	0.535	0.309	0.289	0.254	0.528	0.287	0.310	0.258	0.284	0.247	0.409	0.365	0.260	0.392	0.228	0.365	0.365
Sum	99.27	97.44	99.07	97.34	99.35	99.16	97.72	99.14	98.74	98.54	97.22	95.14	98.73	99.40	99.07	97.38	98.73	98.52
	Normalized Major Elements (Weight %):										Normalized Major Elements (Weight %):							
SiO2	49.70	49.07	49.97	49.84	50.98	48.03	49.17	49.25	49.65	49.13	48.50	50.59	50.54	51.79	50.33	52.14	50.54	50.65
TiO2	2.112	2.480	1.812	1.786	1.519	2.595	1.805	1.797	1.748	1.561	1.428	1.899	1.924	1.757	2.279	1.793	1.924	1.931
Al2O3	14.38	16.21	14.47	14.25	15.15	16.81	14.12	14.74	14.14	15.70	15.03	14.50	14.58	14.11	14.49	14.55	14.56	14.66
FeO*	10.69	10.71	10.79	10.73	9.96	10.81	11.04	10.73	11.22	10.86	11.21	10.13	10.31	10.67	10.73	10.76	10.31	10.13
MnO	0.164	0.176	0.169	0.163	0.158	0.172	0.166	0.177	0.177	0.173	0.176	0.154	0.156	0.162	0.158	0.157	0.156	0.157
MgO	8.74	5.28	8.68	8.65	8.43	5.59	8.66	8.93	8.79	8.10	8.59	7.43	8.90	8.89	8.58	8.59	8.90	8.84
CaO	9.59	10.20	9.83	10.47	10.14	10.20	10.96	10.04	10.20	10.15	11.01	10.91	9.03	8.87	8.87	8.71	9.03	9.06
Na2O	3.26	3.87	3.10	3.04	2.92	3.76	3.01	3.13	3.06	3.25	3.21	3.21	3.17	3.03	3.29	2.53	3.17	3.18
K2O	1.00	1.47	0.86	0.79	0.49	1.50	0.78	0.90	0.75	0.79	0.59	0.77	1.01	0.48	0.88	0.54	1.01	1.02
P2O5	0.371	0.549	0.311	0.297	0.256	0.533	0.294	0.312	0.261	0.288	0.254	0.430	0.370	0.261	0.395	0.234	0.370	0.371
Total	100.00	100.00	100.00	100.00	100.00	100.00	100.00	100.00	100.00	100.00	100.00	100.00	100.00	100.00	100.00	100.00	100.00	100.00

Table 2: A: XRF analysis of SAVF samples, reporting unnormalized and normalized major element oxides (weight percent), sample numbers with boxes are reported by laboratory potentially have clay content; B (next page): Unnormalized trace elements (ppm) and trace element oxides. Analysis by Washington State University GeoAnalytical Laboratory.

Table 2 cont.

Run 0106, Shelby Cave, Arizona State University

Unnormalized Trace Elements (ppm):

Ni	227	54	201	199	200	58	204	199	193	189	212	254	263	264	256	247	263	260
Cr	287	42	269	274	317	66	278	318	276	285	289	300	320	335	308	343	320	322
Sc	25	22	25	23	26	22	24	26	25	26	24	22	23	23	21	24	23	23
V	199	245	227	216	215	273	211	229	233	215	205	152	199	196	200	196	199	196
Ba	476	479	960	1785	245	464	468	288	242	643	704	395	892	228	398	295	892	900
Rb	15	26	15	13	9	27	13	15	13	13	10	14	16	13	15	10	16	16
Sr	456	505	397	396	319	594	346	370	320	373	319	436	471	315	470	318	471	473
Zr	143	190	122	114	99	189	116	122	121	112	99	129	135	112	153	111	135	136
Y	26	27	21	21	20	26	22	23	23	22	21	21	22	21	25	22	22	22
Nb	26.0	41.3	23.5	20.6	18.3	44.4	21.3	24.6	22.9	21.3	15.3	22.3	23.7	14.5	25.5	14.4	23.7	24.1
Ga	18	21	19	17	17	23	18	19	19	18	18	18	20	19	21	18	20	20
Cu	84	76	82	87	104	87	80	75	99	84	92	108	93	126	99	123	93	95
Zn	109	103	100	101	94	100	102	99	110	97	102	98	102	108	112	108	102	101
Pb	3	2	4	3	2	5	4	5	4	3	3	5	3	4	3	3	3	3
La	18	29	22	20	13	32	14	14	19	19	17	17	21	14	23	15	21	18
Ce	46	59	35	35	25	61	36	45	34	30	30	42	42	26	39	28	42	34
Th	4	4	2	1	0	5	2	2	2	1	2	4	3	2	1	0	3	1
Nd	22	30	17	19	12	30	20	20	16	17	15	22	23	14	24	18	23	20
sum tr.	2183	1955	2544	3348	1736	2104	1980	1891	1774	2167	2174	2059	2670	1833	2192	1892	2670	2664
in %	0.22	0.20	0.25	0.33	0.17	0.21	0.20	0.19	0.18	0.22	0.22	0.21	0.27	0.18	0.22	0.19	0.27	0.27
sum m+tr	99.48	97.64	99.33	97.68	99.62	99.37	97.91	99.33	98.91	98.76	97.44	95.35	98.99	99.59	99.29	97.57	98.99	98.78
#+Toxides	99.54	97.69	99.39	97.75	99.57	99.42	97.97	99.38	98.97	98.81	97.50	95.41	99.06	99.64	99.35	97.62	99.06	98.85
#+ToxFe3+	100.72	98.85	100.58	98.91	100.67	100.61	99.17	100.56	100.19	100.00	98.71	96.48	100.19	100.82	100.53	98.78	100.19	99.96

Major elements are normalized on a volatile-free basis, with total Fe expressed as FeO.
"R" denotes a duplicate bead made from the same rock powder.

NiO	289.4	68.1	256.3	253.6	254.8	73.4	259.0	252.6	245.5	239.9	269.3	323.0	334.5	335.9	325.9	314.6	334.5	330.7
Cr2O3	419.9	61.7	393.7	399.9	462.7	96.5	406.6	464.2	403.0	417.0	421.7	438.6	467.0	489.2	449.9	501.0	467.0	470.6
Sc2O3	37.9	34.4	37.7	35.3	40.3	33.3	37.4	39.4	38.3	39.6	36.8	34.1	34.5	35.4	32.1	38.0	34.5	35.6
V2O3	292.9	380.1	334.4	318.1	316.9	401.3	310.8	336.3	342.5	316.4	301.1	222.9	292.8	288.2	293.6	288.6	292.8	288.6
BaO	530.9	535.2	1071.8	1993.1	274.0	518.2	522.4	321.0	270.8	718.0	785.5	440.7	995.6	254.6	444.0	329.1	995.6	1005.0
Rb2O	16.5	28.7	16.7	14.7	10.2	29.0	14.2	16.8	14.1	13.7	11.4	15.3	17.9	14.1	15.9	10.8	17.9	17.6
SrO	536.8	597.0	469.4	467.7	377.0	701.9	409.1	437.1	378.6	440.8	376.7	515.7	556.7	372.6	556.1	375.8	556.7	559.8
ZrO2	195.0	259.1	167.1	156.0	135.3	257.5	158.8	166.3	165.6	153.3	134.9	176.5	184.6	152.6	208.7	151.3	184.6	185.7
Y2O3	31.1	34.4	27.0	27.0	24.9	32.5	28.1	29.0	29.3	27.7	26.3	27.0	27.4	26.8	31.1	28.3	27.4	28.2
Nb2O5	37.2	59.1	33.6	29.5	26.2	63.5	30.5	35.2	32.8	30.5	21.9	31.9	33.9	20.7	36.5	20.8	33.9	34.5
Ga2O3	24.5	28.1	25.0	23.3	23.0	30.4	23.5	25.7	25.4	24.1	23.9	23.7	26.8	25.1	28.6	24.1	26.8	27.3
CuO	105.7	95.4	103.1	108.9	129.9	109.4	100.0	94.0	123.3	104.5	115.0	135.2	116.2	157.9	123.6	154.2	116.2	118.5
ZnO	137.0	128.4	125.4	126.1	117.7	125.2	127.8	124.4	137.4	121.1	128.1	122.7	127.1	135.4	140.8	134.9	127.1	127.0
PbO	3.6	2.6	4.5	3.2	2.4	5.6	4.7	5.0	3.8	3.7	2.9	5.6	3.6	3.8	3.6	2.7	3.6	2.9
La2O3	21.3	34.5	25.9	23.7	15.1	36.9	16.7	16.7	22.6	22.2	19.5	19.6	25.0	15.9	26.4	17.5	25.0	20.6
CeO2	56.1	71.9	43.5	42.5	30.4	74.5	44.4	54.8	42.3	37.1	36.6	52.0	51.6	32.1	48.3	34.5	51.6	41.7
ThO2	3.9	4.2	2.0	1.1	0.1	5.7	2.1	2.5	2.4	1.5	2.4	4.5	2.9	2.2	1.2	0.0	2.9	0.8
Nd2O3	26.1	35.2	19.9	22.6	14.3	35.5	23.7	23.1	21.3	19.6	17.1	25.9	27.1	16.2	28.1	20.4	27.1	22.7
sum tr.	2768	2438	3157	4046	2255	2630	2520	2444	2299	2731	2731	2615	3325	2379	2794	2445	3325	3318
in %	0.28	0.24	0.32	0.40	0.23	0.26	0.25	0.24	0.23	0.27	0.27	0.26	0.33	0.24	0.28	0.24	0.33	0.33

WSU GeoAnalytical Laboratory *Analyses by XRF*

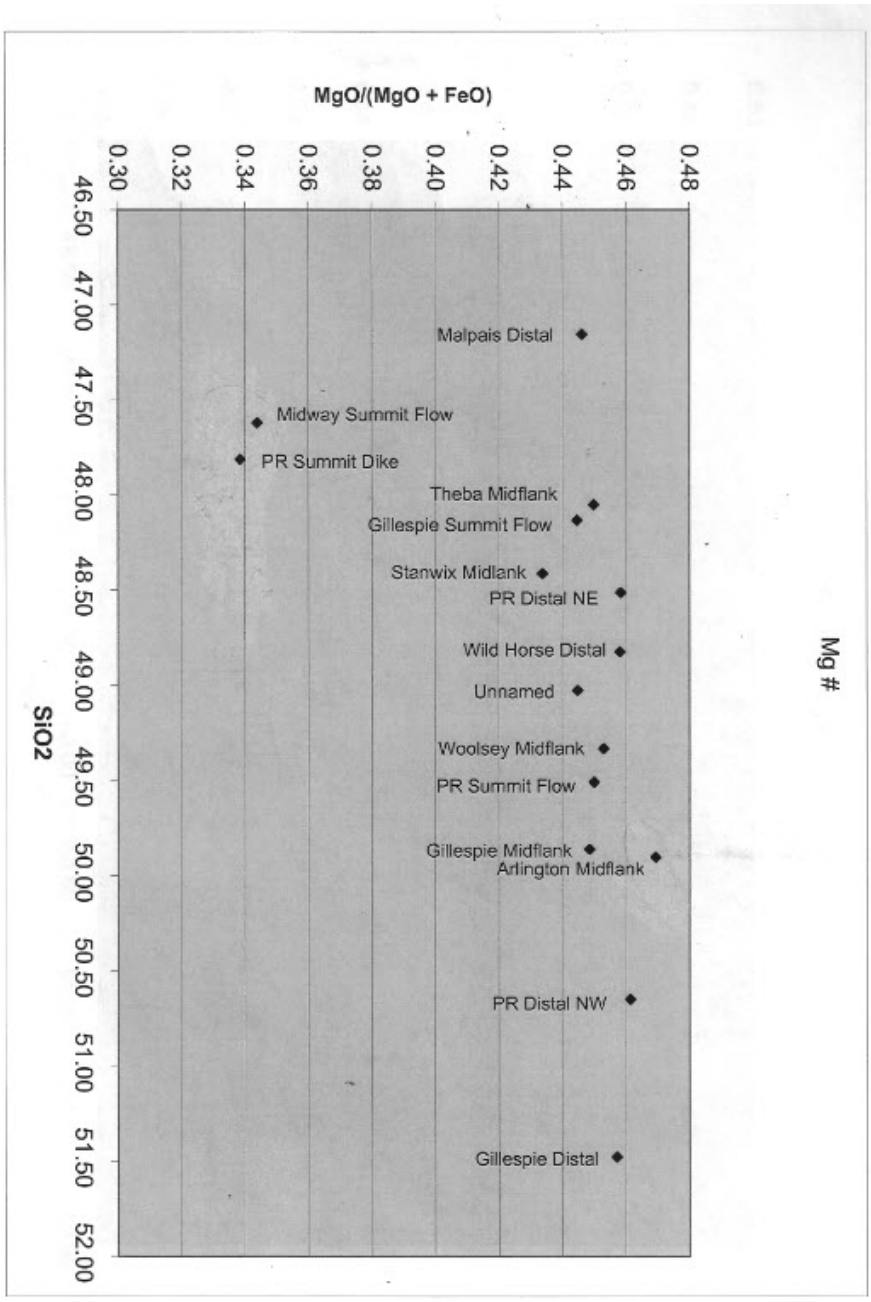


Figure 9: Magnesium number plot for the SAVF, higher Mg # is more fractionated (Arlington), and lower numbers are less fractionated, inversely related to ages.

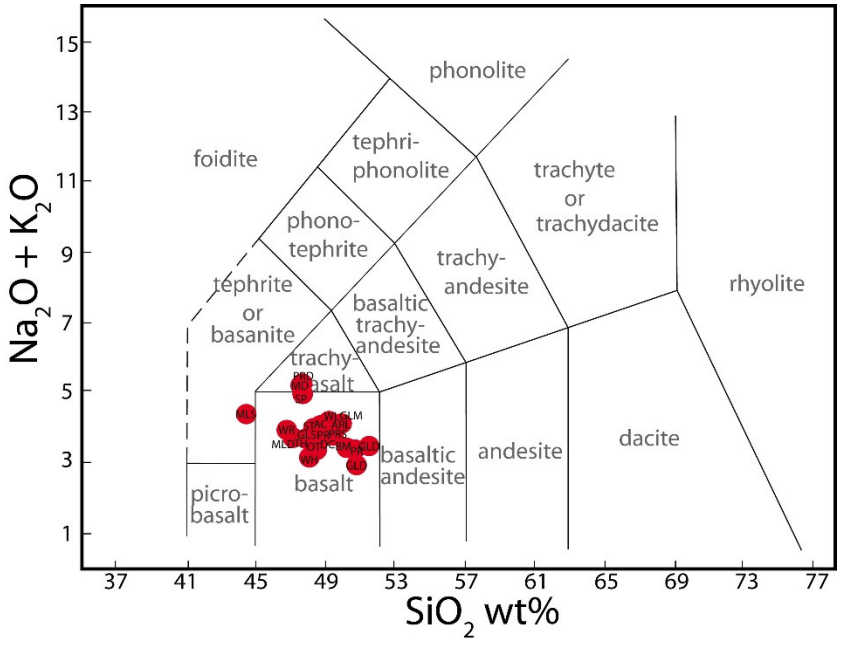


Figure 10: LeBas diagram of XRF analyses of the Sentinel-Arlington Volcanic Field with SiO2 weight percent ranging from 44 to 51%. There is a general decrease in Si content from distal to summit regions. Field observations revealed that distal degassed flows typically had more entrained granitoid xenoliths than summit regions so that may be related to crustal assimilation.

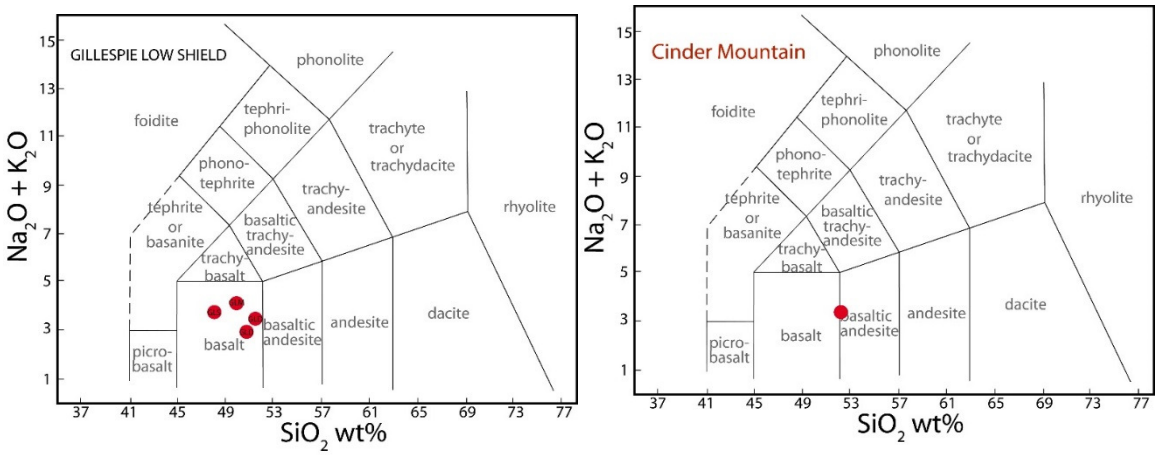


Figure 11: Left: LeBas diagram of XRF analyses of the scatter of values from a single monogenetic SAVF edifice. Right: XRF analysis of older Tertiary cinder cone near southern margin of the Sentinel-Arlington Volcanic Field for comparison.

Shallow magma ascent dynamics also influence the resultant morphology of the basaltic edifices. Vent alignments were observed in the Sentinel-Arlington Volcanic Field in the same NE and NW fabric typically observed in late Cenozoic terranes. Four of the low shield volcanoes exhibited elongation of the summit and midflank region, suggesting that the central vent built from fissure-fed flows or reactivation along a structural control. Alignments and elongations correspond to Basin and Range and Mid-Tertiary moderate to steeply dipping extensional structures in surrounding mountain ranges and pediments. No consistent vent migration was observed in SAVF, unlike eastern migration in Springerville Volcanic Field (Condit et al., 1989) and the San Francisco Volcanic Field (Tanaka et al., 1986) or the late Cenozoic migration of volcanic fields toward the Colorado Plateau (Hamblin, 1978; Luedke and Smith, 1978).

The overall low relief of the Sentinel Arlington Volcanic Field is probably due interactions between several factors, including low viscosity values from relatively mafic melts, very little crustal assimilation, low topographical relief in eruptive substrate, relatively steady long-lived eruptive events with moderate effusion rates and volumes that lead to development of lava tubes that create lava plains and lower overall relief, low magma production in areas of high rates of crustal extension, and shallow magma ascent and eruptive dynamics along pre-existing structures that encourage a disperse field of vents verses a single central conduit.

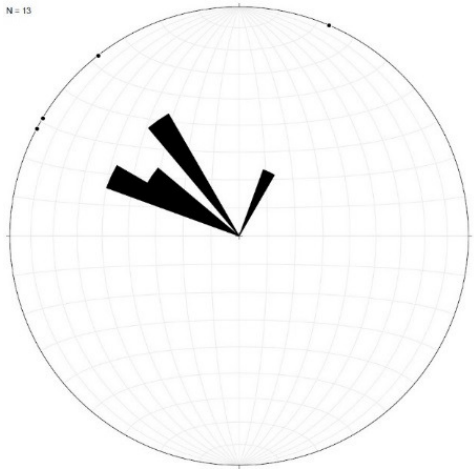


Figure 12: Base elongation of summit and midflank regions of individual edifices

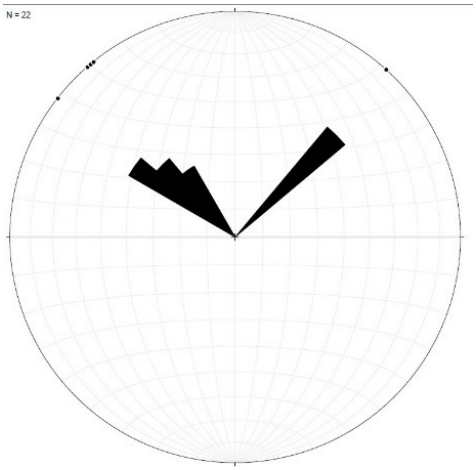


Figure 13: Vent alignments. A NE alignment crosses entire field, with 4 crosscutting NW alignments

The driving mechanism of SAVF could be a mantle hotspot, which has been suggested for the San Francisco volcanic field (SFVF) in northern Arizona (Ulrich and Nealy, 1976; Thompson and Zoback, 1979; Wolfe et al., 1983, etc.) or high-heat flow feature related to changes in lithospheric keel (Luedke and Smith, 1978). If the high heat flow feature is wider than ~35 km while the eruptions were focused on structural weak zones, then that could explain 1) the lack of a definitive vent migration with time, 2) how eruptions could be focused at certain loci over such a relatively long period of time, and 3) the observed vent alignments. The fact that the volcanic conduits do not become plugged or sealed could be a function of the rate of lithospheric extension verses the eruptive reoccurrence interval, periodic dilations in the lithospheric stress regime, and/or a result of the small volume of the eruptions.

Chapter 4

PALEOMAGNETISM AND RADIOGENIC DATING

The Earth's magnetic field is essentially dipolar (Gilbert, 1600, as translated by Price, 1958). The field polarity reverses, the intensity of the field fluctuates, and the dipole field is overlain by regional, dynamic magnetic vector components, all possibly resulting from convective processes at the core-mantle boundary (Bloxham and Gubbins, 1985; Bloxham and Jackson, 1992; Butler, 1992; Bloxham, 2000). The dipole and non-dipole fluctuations in the magnetic field result in latitudinally-dependent, random paleosecular variation (PSV) of the observed magnetic pole positions. The record of direction and intensity of Earth's magnetic field can be preserved in geologic materials. The natural remanent magnetism (NRM) of any sample will have multiple components composing its magnetic vector, which include the high-stability primary vector acquired during formation which can subsequently be overprinted by any secondary, low-stability NRM components such as lightning strikes or long-term exposure to more recent magnetic fields. Because the secondary signal is less stable, lab treatment potentially can be used to incrementally demagnetize each sample to glean the original inclination and declination vectors that were inherited at formation (even when the secondary overprint is strong) if enough of the original high-stability primary vectors remain. The inclinations and declinations of the remaining NRM vectors from all the samples at a site are then compared. If they converge to a direction, all the samples are added to yield a resultant vector, and an alpha-95 (α_{95} = 95% confidence limit) of statistical scatter is calculated using Fischer grouping (analogous to two estimated standard deviations for Gaussian dispersion distribution, from Butler, 1992). Between-site comparisons of PSV inclination, declination, and intensity 'fingerprints' (within the geological context) can reveal probable coeval events when the resultant vector of one geological collection site is completely contained within the α_{95} confidence limit of another.

The Sentinel-Arlington Volcanic Field is a good candidate for paleomagnetic studies because the volcanic units are geologically mapped at sufficient scale to delineate the sequence of

most of the eruptive events, the volcanism is relatively mafic with iron-bearing minerals, and SAVF shows little to no evidence of post-emplacement tectonic disruption resulting in rotation or tilting. SAVF also offers temporal and geographic expansion of the previous paleomagnetic studies of the southwest (for example: Heinrichs, 1967; Kono et al., 1967; Doell et al., 1968; Champion, 1980; Geismann, 1988; Geissman et al., 1990; Tanaka et al., 1990; Brown et al., 1993; Tauxe et al., 2003; Maniken, 2008).

SAVF paleomagnetic data were used to: 1) refine the eruptive history by identifying correlations between geographically independent, non-contiguous but potentially coeval eruptive events, 2) extrapolate radiogenic dates across these statistically-correlated events, and 3) to tie interfingered distal lava flows with their respective source vents where stratigraphy may be ambiguous and the lava flows were texturally and geochemically similar.

METHODS

SAMPLING

A total of 473 oriented drill core samples (Appendix A) were taken from 58 sites in the SAVF (Figure). Samples were taken from basaltic lava flows. Sites were chosen because of geologic context, inferred low lightning strike potential, and accessibility. An average of eight oriented core samples were obtained at each site. Samples were taken using a water-cooled gas-powered portable drill and oriented in place with a sun compass and a Brunton transit compass. Samples at each site were dispersed over a distance of 5-30 m. Areas that noticeably deflected the compass from magnetic north were eliminated because of inferred isothermal remanent magnetism from lightning strikes. This often precluded most of the topographically high areas such as the summit areas of the shields.

Titanomagnetites with some titanohematites are primary crystallization phases in igneous rocks, constituting 1% to 5% (by volume) of a typical basaltic lava flow (Butler, 1992). XRF analyses reveal weight percentages for TiO of 1.3% to 2.5%, and FeO of 9.6% to 11.1% for SAVF

lava flows. These were used to calculate CIPW norms, which revealed olivine normative basalts with weight percentages for ilmenite (titanohematite) ranging from 2.64 % to 4.89%, which is the modeled magnetic material for the samples collected.

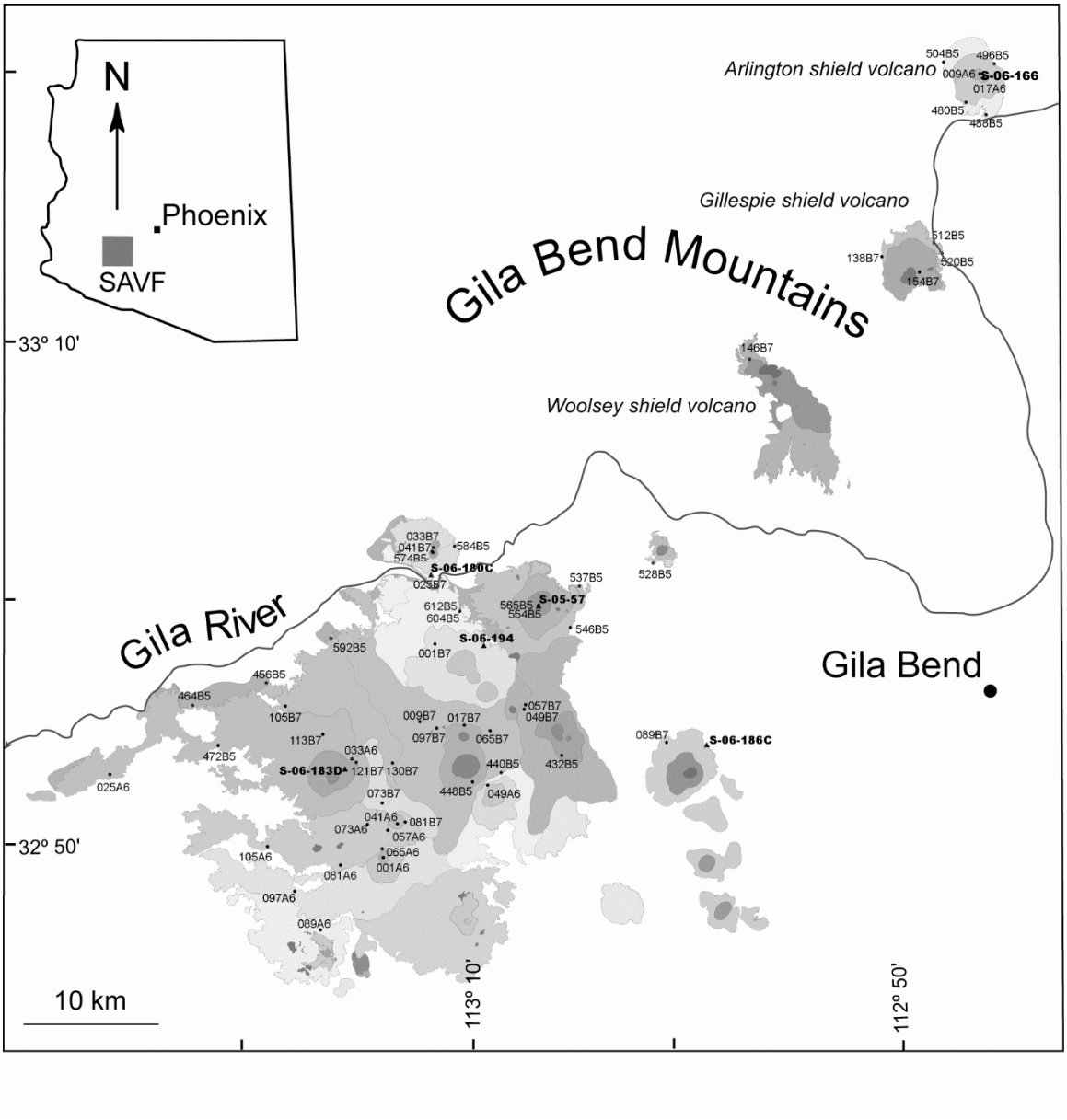


Figure 14: A Location map of the 58 paleomagnetic sample collection sites a radiogenic dating sites. The southern margin of the volcanic field is within the Barry M. Goldwater Bombing Range and sampling is restricted.

Weathering of primary titanomagnetites and titanohematites almost always includes syneruptive deuteric oxidation which decreases the grain size and enriches the Fe content, which in turn increases the saturation magnetization (Butler, 1992). Deuteric oxidation is dependent on cooling rate and oxygen fugacity and typically proceeds to higher stages in the interior of a lava flow (Butler, 1992). Other weathering includes low-temperature oxidation which decreases saturation magnetization by weathering of some magnetite into maghemite (Butler, 1992), and would possibly be more likely on exterior regions and fractures within lava flows. These weathering profiles might suggest that higher paleomagnetic moments could be preserved in the interior of lava flows when all other factors are equal. However, smaller grain size usually indicates a higher ratio of single-domain grains to multiple-domain grains (one magnetic moment per grain, similar to one small magnet versus a larger but weaker cluster of magnets). The initial paleomagnetic results revealed that the single-domain grains of the quenched exterior of the flows did generally yield the highest saturation magnetization overall and were given preference in subsequent sampling campaigns.

Samples for $^{40}Ar/^{39}Ar$ dating were chosen based on geologic context after the majority of paleomagnetic analyses had been completed. Preference was given to sites that 1) could be statistically correlated with multiple other units within a 95% confidence interval, which could potentially represent an eruptive episode (see RESULTS below), 2) represented stratigraphic end members, or 3) potentially give insight into the timing of interactions with the ancient Gila River. Samples were collected from holocrystalline interior portions of individual lava flows and petrographically examined to assess alteration and glass in the groundmass before dating.

PALEOMAGNETIC METHODS

The core samples were 10-12 cm long. Each sample was cut into 3-4 individual specimens. The NRM vector of a specimen from each sample was measured at the U.S. Geological Survey's Rock Magnetics Laboratory at Menlo Park, CA, in a uniquely-designed cryogenic Superconducting

Rock Magnetometer, which can measure the remanent magnetic vectors of rock specimens up to 10 cm^3 in volume with a practical sensitivity of 1 to 5 x 10-8 emu. The magnetometer is housed in a shielded room that reduces the ambient magnetic field to less than one percent of its normal value. Progressive demagnetizations were made using alternating field (AF) 3-axis tumbling demagnetizer operating at 400 Hz, producing a maximum magnetic field strength of 1000 Gauss (0.1 Tesla). The sample was held in a reciprocating tumbler to reduce spurious magnetization.

RADIOGENIC METHODS

Sample S-05-057 was sent to the New Mexico Geochronology Research Laboratory (NMGRL) and samples S-06-166, S-06-180C, S-06-183D, S-06-186C, and S-06-194-A were sent to the Rutgers Noble Gas Laboratory (RNGL) for $^{40}Ar/^{39}Ar$ radiogenic dating. At NMGRL the sample was crushed and rinsed with dilute acid solution. The groundmass concentrates were prepared with standard heavy liquid, handpicking, and magnetic separator techniques (Peters, 2006). The samples were loaded into 2.4 cm aluminum discs and irradiated for one hour at the Nuclear Science Center in Texas A&M University, College Station, Texas. Groundmass concentrates were analyzed with the double-vacuum Mo resistance furnace incremental heating age spectrum method using a 10W CO_2 laser. The released argon isotopes were measured on a MAP-215-50 mass spectrometer (from Peters, 2006).

At the Rutgers Noble Gas Laboratory the samples were examined petrographically, crushed, sieved, and selected fractions washed in ultrasonic baths of distilled water. Samples were irradiated in the cadmium-lined, in-Core Irradiation Tube [CLICIT] facility of the Oregon State University Triga Research Reactor [OSTR]. Incremental heating was accomplished in step-wise increments using a New Wave Research Inc. uniquely-designed 50 Watt CO_2 laser incorporating a two-color IR optical pyrometer and defocused though 2 mm and 6 mm integrator lenses. The released argon isotopes were measured on a MAP-215-50 mass spectrometer especially designed

for the measurement of He and Ar, having 90° sector extended-geometry for enhance separation of Ar isotopes.

RESULTS

Of the 58 sites paleomagnetically analyzed, two sites were irresolvable, six had magnetic vectors that did not group well after alternating field demagnetization, and 50 sites had well-grouped PSV vectors. Of the sites with well-grouped vectors, 39 were reversed polarity and 11 were normal (Figure 13). Four reversed polarity sites were $^{40}Ar/^{39}Ar$ dated (RNGL) with sufficient precision to fall within the Matuyama Chron (reversed polarity magnetic epoch, Figure 14). These results were 1.08 ± 0.15 Ma; 1.25 ±0.024 Ma; 1.71 ± 0.054 Ma, 2.30 ± 0.035 Ma, and 2.37 ± 0.02 Ma. One normal polarity site was $^{40}Ar/^{39}Ar$ dated (NMGRL) to the Olduvai normal excursion within the Matuyama Chron with an age of 1.91 ± 0.59 Ma (Figure 14, Cave et al., 2007). The value for the date is well within the Olduvai time frame, with error bars that extend beyond the beginning and end of the normal excursion into the reversed chron, but do not extend into any other normal polarity events (Figure 13). These error bars are attributed to a large initial incremental heating step during analysis combined with behavior indicative of excess argon noted later in analysis (Peters, 2006). RNGL was alerted to this issue prior to subsequent $^{40}Ar/^{39}Ar$ dating and was able to obtain higher precision. The isotopic ages and magnetic polarities are consistent with currently accepted geomagnetic polarity timescales (Ogg and Smith, 2004).

The initial paleomagnetic analysis was completed on one discrete volcanic center with a single summit and no evidence for paleosols between units known as Arlington low shield (ALS). ALS is interpreted to be essentially monogenetic, so the PSV 'fingerprint' for a single eruption sequence was investigated. The typical PSV scatter of the NRM vector for individual units was measured, and PSV correlations between units were compared. The summit region and 4 distal lava flows were sampled. Most sites correlated within the 95% confidence level, and the farthest deviation was a sweeping loop of >4º (Figure 9). These well-grouped vectors indicate that the

volcanic event may have occurred within a 100-year period given the standard behavior of secular variation documented in other locations (Shoemaker and Champion, 1977; Champion, 1980).

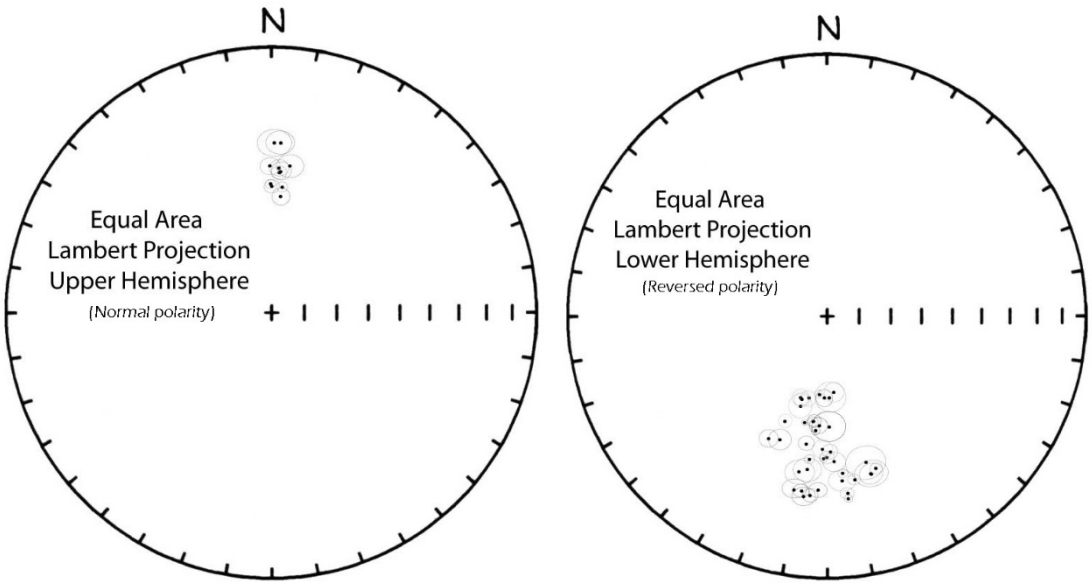


Figure 15: The resultant paleo-magnetic vectors for each sampling site displayed within their respective α_{95} confidence intervals

Across the SAVF, flows sampled from the same source vent typically had PSV vectors that similarly correspond within a 95% confidence interval, suggesting that most SAVF vents probably represent a single event. However, compound edifices typically had multiple PSV groupings, suggesting underlying fissure vents or that vents could be reactivated without migrating to a distinct edifice. Some unambiguously separate source vents correspond within a 95% confidence level (Correlations A, B, C, and D in Figure 15), suggesting that those vents were coeval. Out of 50 sites, at least 15 unique PSV directions could be identified, 12 of which were reversed and 3 were normal. Most directions were only sampled once. However, some groupings could be identified. Four reversed PSV directions were preserved by at least 2-3 volcanic events each; and 2 normal polarity directions were preserved by at least 2 volcanic events each. Some volcanic

events that were erupting at the same time were geographically widely-separated and not strongly aligned (Correlation D, Figure 15), though two NE-SW and one NW-SE alignments of coeval events were documented (Correlations A and B, and Correlation C, respectively, Figure 15).

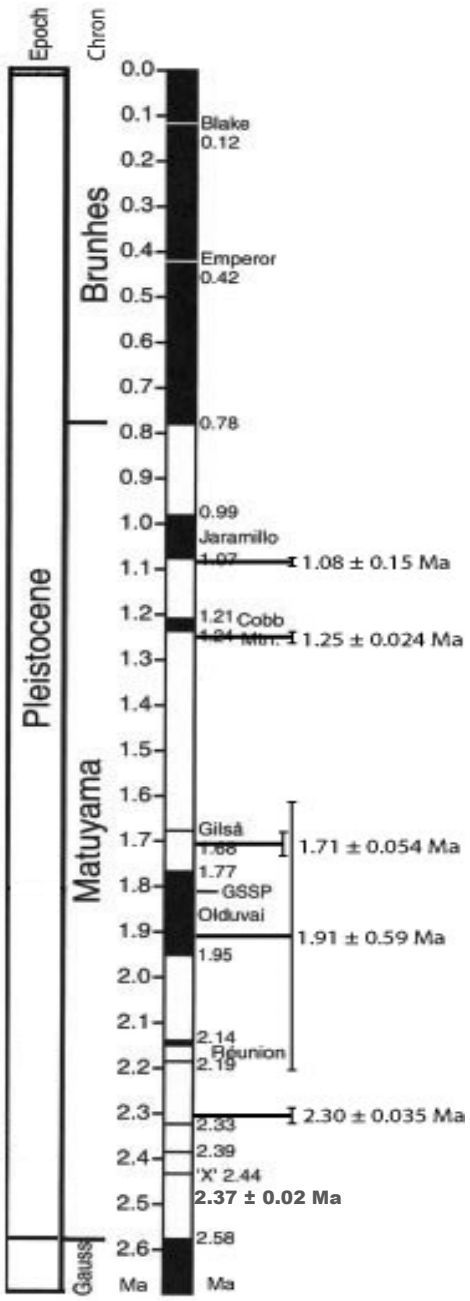


Figure 16: SAVF $^{40}Ar/^{39}Ar$ dates plotted on Pleistocene magnetic polarity scale. Four of the reversed sites were dated by Rutgers Argon Laboratories to the Matuyama Chron: 1.08 ± 0.15 Ma; 1.25 ± 0.024 Ma; 1.71 ± 0.054 Ma, 2.30 ± 0.035 Ma, and 2.37 ± 0.02 Ma; and 1 normal polarity site was dated by the New Mexico Geochronology Research Laboratory to the Olduvai normal excursion within the Matuyama Chron: 1.91 ± 0.59 Ma. Polarity scale adapted from Ogg and Smith, 2004 to reflect the change of the base of the Pleistocene from ~1.8 Ma to 2.58 Ma (Gibbard et al., 2009).

Two of the reversed polarity and one of the normal polarity sampled volcanic pulses included paleomagnetic sites that were also radiogenically dated. These dates were extrapolated to the other paleomagnetically correlated events (Figure 15). The radiogenic dates cover a time span of at least 1.2 Ma starting by the early Pleistocene. The radiogenic dates and PSV correlations were used to establish the relative ages of units in contact with each other near an ancient Gila River paleochannel, which clarified a paleo-lava dam ambiguity from the geologic map on the southern margin of Oatman low shield.

The SAVF eruptive duration (1.2 Ma+) is longer than non-dipole (<3000 yrs) and dipole secular variation (10,000-100,000 yrs). Assuming the paleosecular variation was adequately sampled, then the average of the VGP positions for each polarity represents the paleopole position during this time frame, which should begin to mimic the rotational axis according to geocentric axial dipole hypothesis (Butler, 1992). Angular dispersion of SAVF reversal VGP values is sufficient for expected values from a robust data set at this corresponding latitude (Merrill and McElhinny, 1983). However the angular dispersion of sampled normal VGP positions is only ~5 degrees and the values fail the reversal test (the antipode of the mean does not match the mean of the reversed VGP positions), suggesting that the normal polarity was not adequately sampled to determine the VGP.

The latitude and longitude of the mean of the reversal VGP positions gives a paleomagnetic pole position of λp (pole latitude)= -86.1º S and Φp (pole longitude)=13.1º E where N (number of sites) = 44; K (precision parameter) = 28.7, S (angular dispersion) = 15.1º with an α_{95} of 3.9º. The antipode of this pole position is 86.1º N, 193.1º E. The latitude of this paleopole corresponds within 2 degrees to the latitude of reference poles given by Besse and Courtillot (1991) for North America for the last 10 Ma (84.0º N, 153.1º E), and Maniken paleopole range reported for the southwestern USA during the Matuyama reversed epoch of 84.5º to 84.6º N, 58.1º to 61.0º E, but the longitude differ by ~40º and ~130º, respectively (which is comparable to the total range of the reference values).

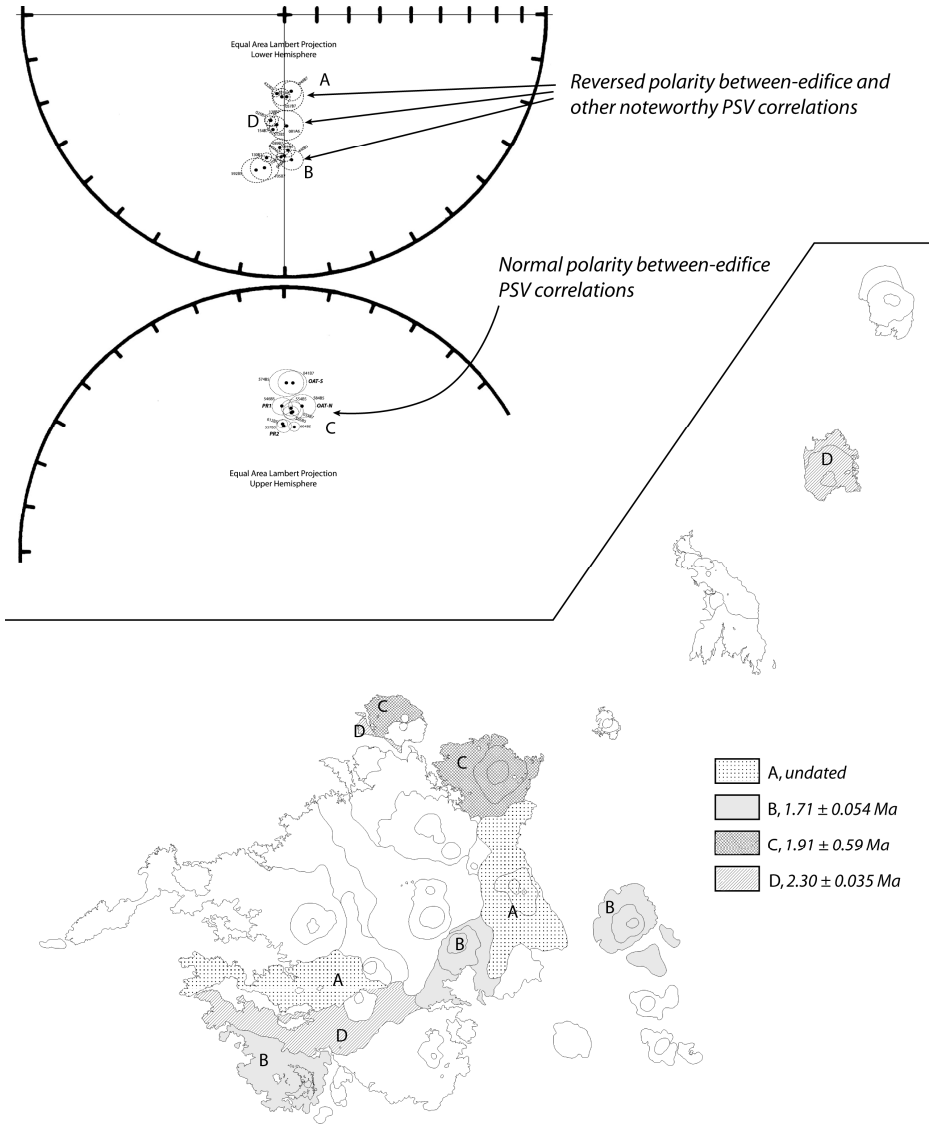


Figure 17: A) PSV vector plots of selected correlative samples with α_{95} confidence limit displayed; B) Map of selected volcanic events sharing the same PSV "fingerprint". Correlation A is stratigraphically the youngest correlation and reveals a possible NE-SW alignment of reversed polarity events separated by ~25 km. Correlation B contains a unit that is radiometrically dated at 1.71 Ma, and reveals three small reversed polarity shields across the southern sector of the field aligned to the NE-SW are probably coeval. Correlation C contains a unit radiometrically dated at 1.91 Ma, and reveals one normal polarity shield and one of the edifices of a second shield aligned to the NW-SE are probably coeval, both of which display pillow lavas associated with a lava-dam induced paleolake. Correlation D contains a unit radiometrically dated at 2.3 Ma, and shows a small reversed-polarity shield and several partially revealed lava flows across the entire SAVF are probably coeval. The broad distributions of the correlations indicate that there is no strong evidence for vent migration in SAVF, though three NE-SW alignments of coeval events and one SW-NE alignment of coeval events were noted.

The understanding of the eruptive sequence of SAVF was significantly expanded based on paleomagnetic correlations and radiogenic dates. Because radiogenic dating was limited, the paleomagnetic data were used to correlate volcanic events and expand the application of radiometric results (Correlations B, C, and D, Figure 4). Paleosecular variation correlations proved especially useful for incorporating discrete eruptive vents into the eruptive history of the main field and for unraveling the emplacement of reoccurring lava dams along the ancient Gila River. The geochronological and paleomagnetic data also reveal that all four small shields with only a single vent represent a single PSV signature for the flows that compose the edifice, and 2 small shields with at least 2 vents also were a single eruptive event based on PSV correlations, while 5 shields with at least 2 vents represent reactivated loci that preserve flows from multiple volcanic episodes with differing PSV signatures, especially along pre-existing NW-SE tectonic alignments in the geographic center of the field. Ten edifices did not have enough sampling to determine the PSV signatures where shared by flows composing the majority of the edifice. Shields composed of multiple vents erupting at basically the same time suggests that fissure eruptions may play a role in development of at least some of the small shields in SAVF.

Chapter 5

PALEOHYDROLOGY OF THE ANCIENT GILA RIVER PRESERVED BY THE SAVF

The Gila River begins in southwestern New Mexico just west of the Rio Grande rift, flows westerly across southern Arizona, and joins the Colorado River near Yuma, Arizona. The goal of this project was to determine the nature of the interactions between the lower Gila River and the Sentinel-Arlington Volcanic Field (SAVF). The lower Gila River refers here to the segment of the river channel downstream of the confluence of the Gila River and the Salt River, a major tributary that joins the Gila just west of Phoenix (Figure 16). The lower Gila-Colorado River system probably connected to the Sea of Cortez ~4 Ma (Spencer and Patchett, 1997). The small shield volcanoes of SAVF have a very low height to diameter ratio (~0.005-0.012) except where distal flows have been removed by undercutting and erosion along the Gila River. This low aspect ratio is indicative of relatively fluid lava flows, which can be strongly controlled by paleotopography. Also, basaltic volcanic constructs composed primarily of lava flows have been shown to weather slower than cinder cones (Dohrenwend et al., 1984). These factors combine to allow low shields to reveal details of remnant landscapes that are older than what would be preserved by volcanic fields composed of a higher percentage of pyroclastic material. Low shields can be a window in time, specifically SAVF is a glimpse into the geomorphology and hydrology of the Pleistocene Basin and Range province of southwestern Arizona.

METHODS

This study aimed to characterize the nature of the lava dams on the lower Gila River through detailed field mapping. This was supplemented by paleosecular variation studies of the natural remnant magnetism preserved in the lava flows, which was used to determine time stratigraphic units and correlations between volcanic events. Paleo- channel characteristics

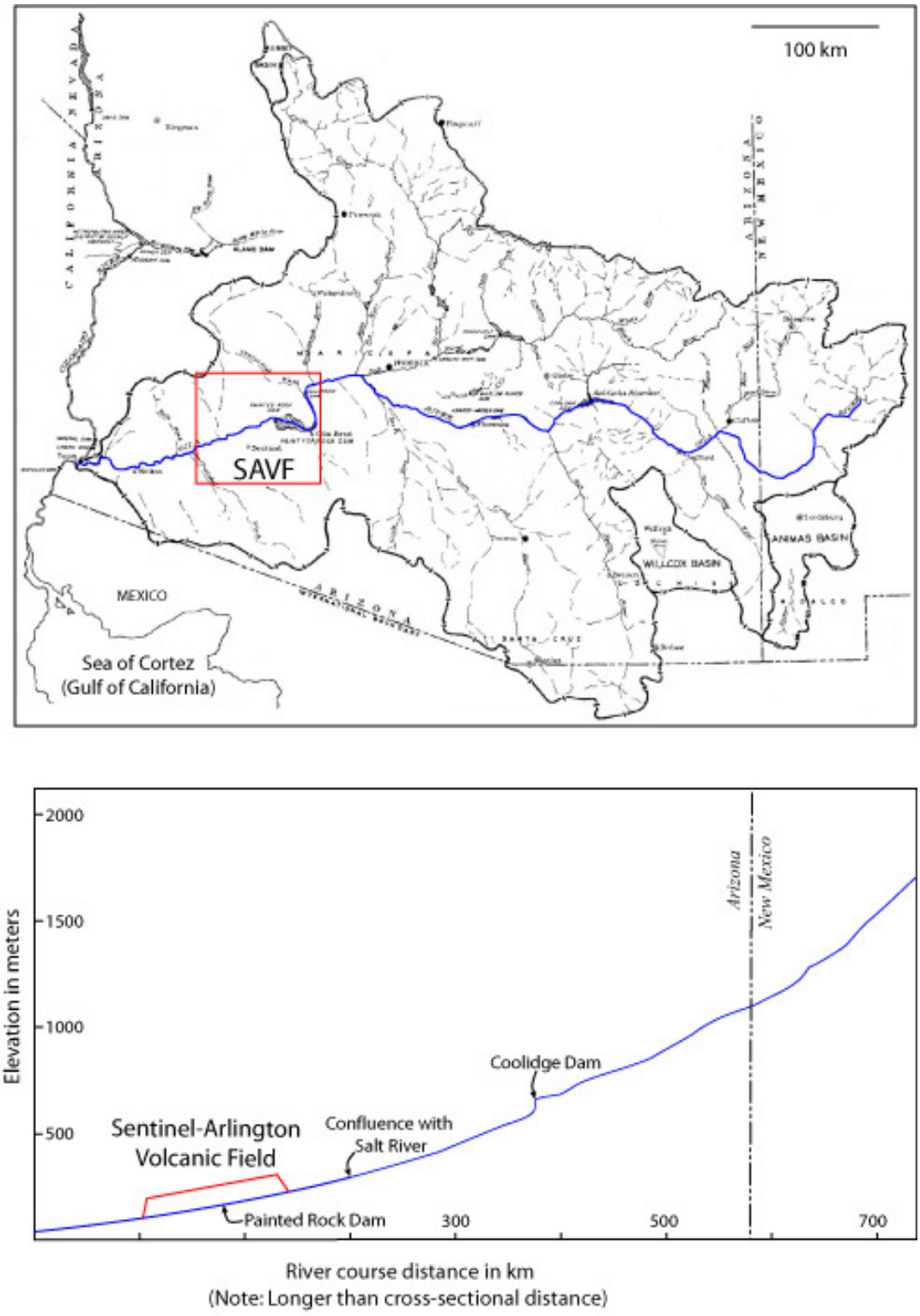


Figure 18: Drainage basin and longitudinal profile of the Gila River.

preserved by the SAVF were analyzed to estimate slope and discharge values for the ancient river. The extent of the paleolakes were mapped and field-checked based on the projected minimum heights of the lava dams. These are over-estimates of the paleolake extents because of overall lowering and fluvial incision of the alluvial surface since the lava dam events.

The base map for the field work included use of 7.5 minute digital orthophoto quadrangles (DOQQs), 7.5 minute digital raster graphics (DRGs), 1/3 arc-second digital elevation models (DEMs), USGS Landsat Orthoimagery Mosaic (false color composite using Landsat 7 Thematic Mapper bands 4, 3, 2), and SIR-C X-band radar (shuttle-born, 3.1 cm wavelength). These digital products were mosaiced and overlain using ESRI ArcGIS software. Preliminary identifications of possible paleolakes were made using the presence of water-cut canyons through lava flows, often paired with very flat agricultural areas directly upstream; lava flows that appear to divert into pronounced pre-existing topography; and direct observations of possible paleochannels visible in both the aerial photography and the shuttle radar data. Lava flows that have been eroded by the river after emplacement tend to have a very smooth, rounded edge, while more protected margins tend to be more sinuous and digitate.

Evidence used to identify interactions include lava flows lying on river gravel terraces where the lava flow thickens over a short distance, typically by the base contact lowering while the surface elevation remains steady, often accompanied by ~1 m diameter columnar fracturing. This was interpreted to be paleochannel infilling. Evidence used to identify lava dams that specifically interacted with water included palagonitic alteration rinds and pillow lavas (Figure 17). Field data used to identify ancient Gila River gravels include very rounded, polymictic gravels and cobbles up ~25 cm found at characteristic elevations. The ancient river sediments usually exhibited laminated pedogenic calcium carbonate accumulation that had fractured smaller clasts if buried by SAVF lava flows, or desert varnish accumulation on upper surfaces if undisturbed and exposed.

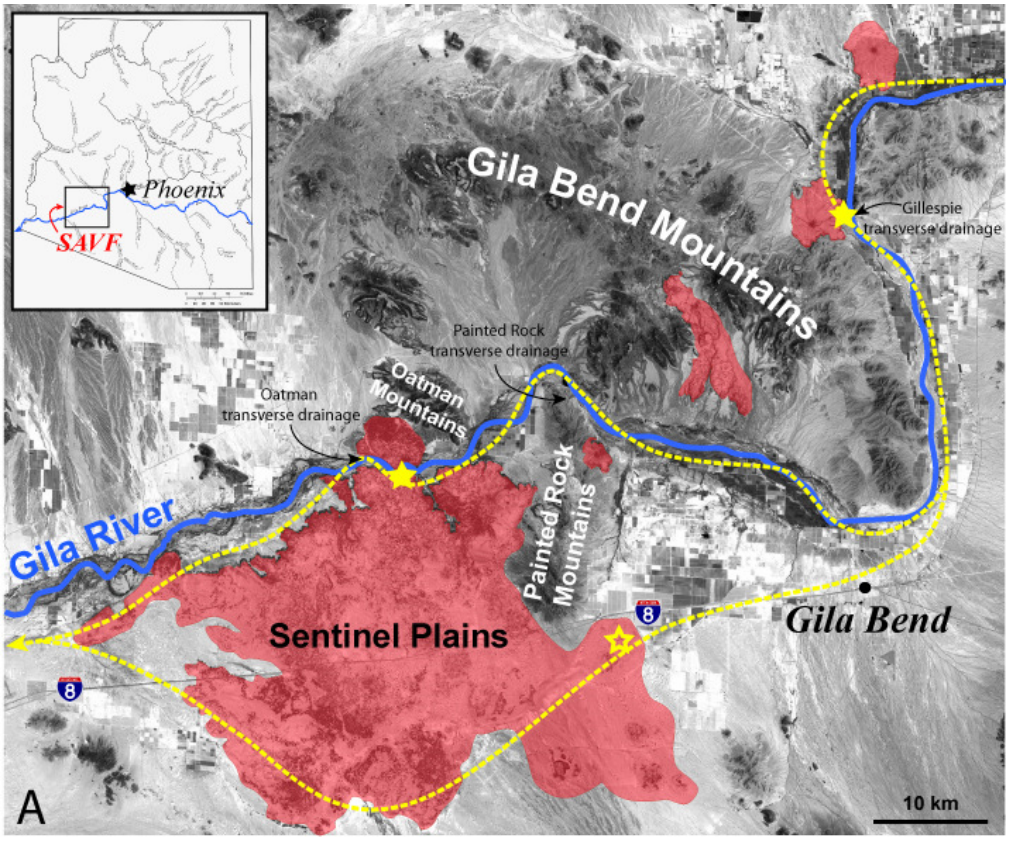




Figure 19: A: The Sentinel-Arlington Volcanic Field (SAVF). Volcanic deposits are indicated in red, lava dams identified by field evidence are indicated by solid yellow stars, proposed lava dams based on remote sensing and geomorphologic evidence are indicated by hollow yellow stars, B: Pillow lavas with glassy tan palagonitic alteration rind used as one line of field evidence for river/lava interactions.

RESULTS

SAVF-Gila River interactions identified in the field

Sentinel-Arlington Volcanic Field interacted with the ancient Gila River multiple times during its eruptive history, resulting in a series of lava dams and diversions along a 140 km stretch of the river. The upstream extent of these interactions begin near the confluence of the Hassayampa River with the Gila near Arlington Mesa, identified here as Arlington low shield (ALS) volcano. ALS lava flows rest on Gila River gravels (Péwé, 1978; Cave and Greeley, 2004) on the southern margin of the shield approximately 10 m above the current channel. It is unclear whether these gravels were a stranded terrace or an active channel at the time of ALS emplacement, because there are no indications of direct lava/water interactions preserved by Arlington lava flows. However, since the channel is bounded by the Buckeye Hills to the south and the margins of ALS lava flows to the south have been undercut and eroded laterally by the river, a lava dam cannot be completely ruled out. Arlington low shield has been dated by Ar-Ar as 2.37 Ma +- 0.02 Ma

A lava dam initiated by the Gillespie low shield (GLS) volcano ~10 km downstream of ALS (Figure 17) was proposed by Lee and Bell (1975) and investigated (Cave and Greeley, 2004). Field investigations reveal that the river was potentially dammed and diverted ~1/2 km east, cutting a new channel through a less resistant and stratigraphically older basaltic and basaltic andesite tilt block. Interactions between the river and erupting lava flows are preserved as ~1 m diameter pillow lavas coated in palagonitic rinds at the base of a ponded lava flow. The pillow lavas at the basal contact on the northeastern margin of the low shield extend for ~100 m. The lava flow distally thickens from 6 m to 11 m over the pillow lavas. The surface of the damming lava flow has a thin veneer of sand deposits, small rounded gravels and some indication of overflow and failed re-incision from downstream undercutting. Based on this observation, the potential extent of the proposed paleolake terrace was mapped based on the height of the lava dam (Figure 20). The damming lava flow that represents the Gillespie low shield lava dam displays reversed paleomagnetic polarity and has paleosecular variation that is statistically correlative to another lava

flow in the Sentinel Plains area (which possibly also represents another lava dam) and is Ar-Ar darted at 2.30 Ma +-0.035 Ma. The proposed lava dam sits on a river gravel terrace approximately 17 meters above the current channel.

Discrete low shield volcanoes make a topographic high, with distal margins 5-8 m above the ground surface, and the base level has consistently lowered in this area since the Pleistocene, as observed by the paired erosional and strath terraces long rivers in the area (Péwé, 1978; Luna et al., 1992), so most mantling material is composed of aeolian fines and calcrete rubble, unless some condition allows surface runoff access onto the SAVF volcanic deposits. Field mapping revealed that Arlington low shield has a minor alluvial veneer in elevations that should have been barely inundated by the proposed Gillespie low shield paleolake, and the Ar-Ar ages appear consistent with Arlington being older and potentially affected by paleolakes initiated by Gillespie low shield. However, field investigations at the proposed height of the dam in the intervening alluvial plain do not reveal a well-developed zero-slope terrace at that elevation, suggesting that either the lava dam terrace is not well-preserved, or that the paleolake was ephemeral and that the channel diverted east and cut a new path into its current channel relatively quickly before the paleolake completely filled with sediment. The transverse drainage cut by the new path of the river is utilized by the manmade Gillespie Dam, built in 1921 and breached in 1993. Sediment accumulation from this dam is at a lower elevation than the proposed paleolake terrace.

Ancient Gila River gravel terraces ~20 m above the current river bottom preserved along the river channel in the Sentinel Plains area are extensive (Reynolds and Scotnicki, 1993; Cave, 2014). At least one lava dam has been identified from field evidence along the current channel. Lava flows from Oatman low shield northern vent (Figure 17) flowed into standing water, forming pillow lavas approximately 40-70 cm in diameter coated in palagonitic alteration. Pillow lavas and palagonite extend along one flow margin for over 3 km, revealing that the lava flow was potentially interacting with an already established or recurring paleolake and not just a channel. The pillow lavas have normal paleomagnetic polarity, while the proposed damming flow on the south flank of

Oatman low shield has reversed magnetic polarity, has a paleosecular variation correlative to Gillespie low shield, and an Ar-Ar age of 2.30 Ma ± 0.035 Ma. The reversed polarity damming lava flow exhibits distal thickening to ~11 m and the lateral margins are vertical contacts with embedded calichified gravel deposits, indicating that this flow could be an intracanyon flow infilling an even older lava dam breach event. The damming flow was topographically traced to one of the vents of a compound low shield to the south. The field relationship between the intracanyon flow and the vent was paleomagnetically verified. Other vents from the same shield had unique directions, indicating some vent localities in the thickest part of the volcanic pile in the Sentinel Plains may be polygenetic.

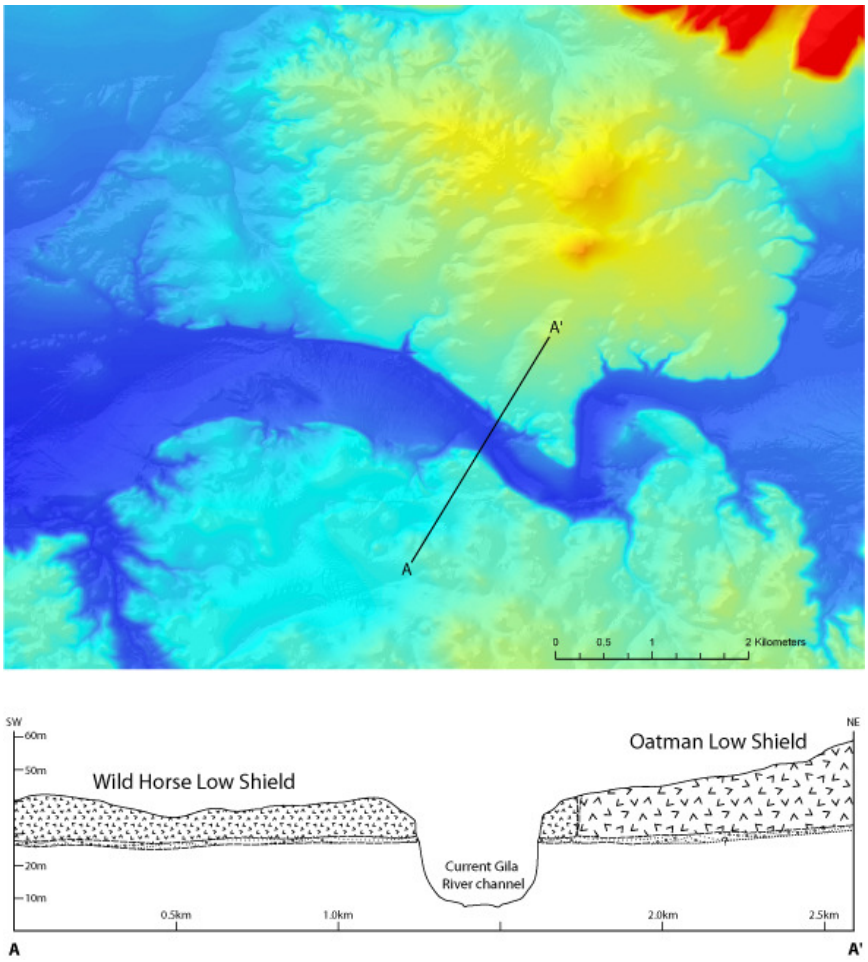


Figure 20: Location and cross-sectional profile of canyon geometry used in paleochannel calculations.

Upstream of the Oatman low shield lava dam is the Dendora Valley agricultural area that utilizes an anthropogenic terrace (~153 m) of sediments from an earth dam built in the late 1800s and early 1900s as well as a higher terrace at ~175 m from the proposed paleolake(s) from the Oatman low shield lava dam(s). The 175 m terrace extends upstream through the transverse drainage into Citrus Valley area.

Field investigations reveal that the Citrus Valley agricultural area also has a very flat plain that potentially represents an accumulation of sediment at 222 m elevation, higher than the potential terrace development in response to the Oatman low shield lava dam(s), and could potentially be an older terrace. A possible southern channel of the Gila River along the southern margins of the Sentinel Plains area has been suggested before based on geomorphology of the region (Chronic, 1983). The potential southern channel would cross the broadest, lowest local basin in the region, while the current path of the river takes an obvious dog-leg north away from the plain and across the northern Painted Rock Mountains (Figure 4, note town of 'Gila Bend'). Multiple possible paleochannels, both crosscutting and underlying SAVF deposits can be seen in remote sensing data in the southern and western regions of the study area near the Sentinel Plains region (Figure 4). Even though Theba low shield has been dated at 1.71 Ma and is probably too young to be the culprit for the initial proposed diversion of the Gila River, and no lava dam has been identified along the southern Sentinel Plains, at least one of the southern paleochannels can be tied to the ancient Gila River by the presence of polymictic, rounded large gravels identified at basal contact of one eroded spatter and cinder cone. The gravels match the lithology and dimensions of the Gila River gravels identified along the northern channel (Figure 4). Field observations and major and trace elemental analysis verify that the cinder cone matches the narrow compositional range represent by SAVF lavas, though this particular edifice has not been dated. The 222 m terrace might represent the backwater sediment accumulation in response to the earliest stages of SAVF eruptions that potentially diverted the ancient Gila River north of the Painted

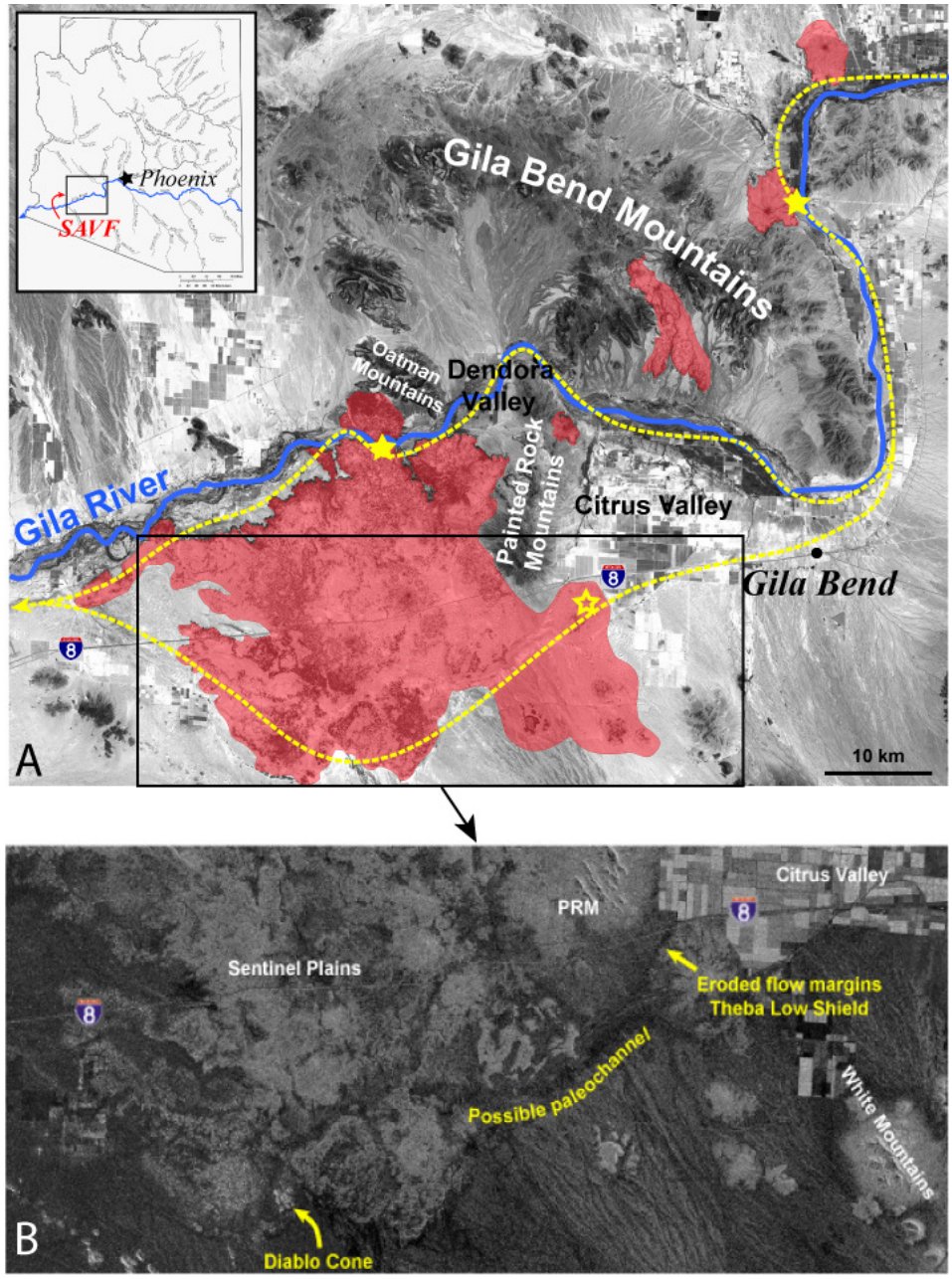


Figure 21: Paleochannels of the lower Gila River preserved by the SAVF.
A: Paleochannels of the lower Gila River in the vicinity of the SAVF.
B: C-band (3.1 cm wavelength) radar mosaic showing geomorphic evidence for southern paleochannel.
C: Gila River gravels preserved underneath Diablo Cone, exposed in a small gravel quarry.

Rock Mountains. However, the complexity of alluvium deposits, paleochannels on surface and captured in radar crossing the lower SAVF combined with the gravels underneath some volcanic deposits indicate that the interactions between the ancient Gila River with SAVF eruptions could be complex and long-lived as the river responded to variate accumulations of the volcanic sequence along multiple paleochannels. The northern knickpoint cut across the Painted Rock Mountains has been utilized by the man-made Painted Rock Dam, and the Painted Rock Reservoir is a dry catch reservoir whose capacity closely corresponds to the proposed Citrus Valley 222 m terrace. Investigations of pre-dam topographic data and field observations of reservoir margins verify that the rare flood events that occasionally fill the reservoir have not deposited any significant clastic sediment above ~168 m, outside of the Holocene river channel.

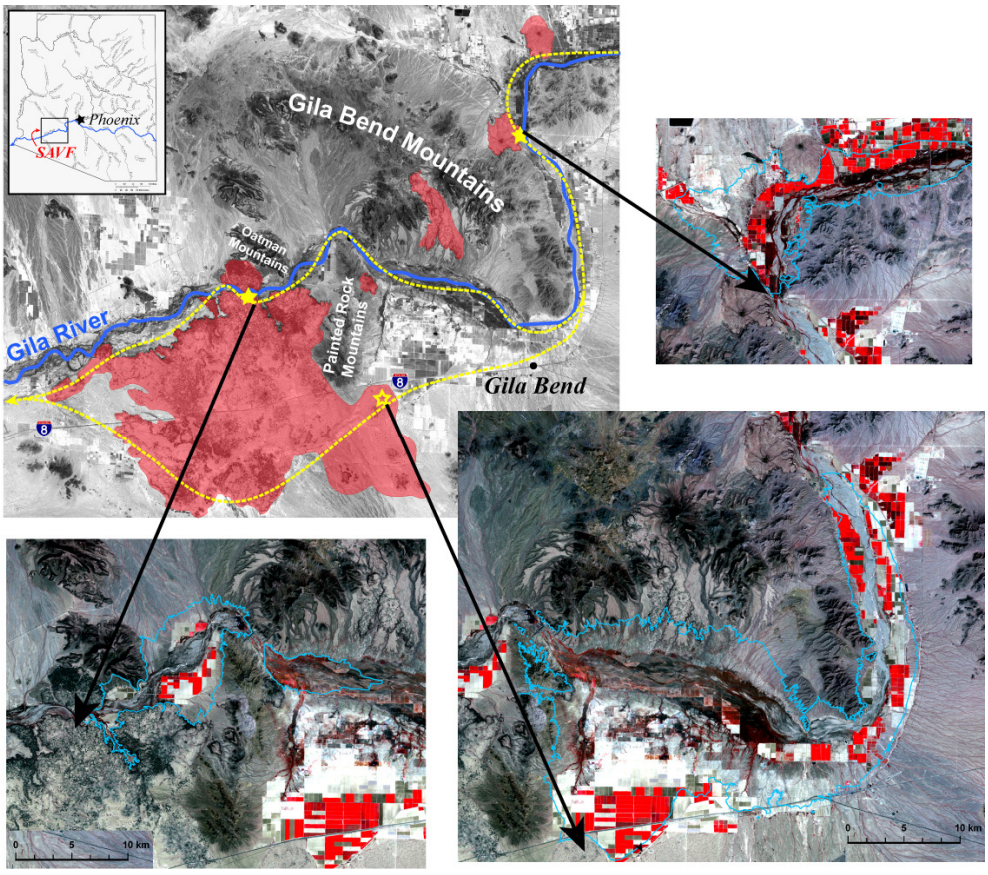


Figure 22: Possible paleolakes on the lower Gila River caused by lava dams from the Sentinel-Arlington Volcanic Field: upper right ~258 m proposed but not observed terrace from Gillespie low shield lava dam, lower right, ~222 m observed terrace in Citrus Valley, lower left ~175 m observed terrace from Oatman low shield lava dam.

Characteristics of the ancient river, field-identified and calculated

Pillow lavas on the ancient river channel bed were identified at Gillespie low shield at ~249 m elevation, and ~85 km downstream at Oatman low shield at ~164 m elevation. Assuming no incision or aggradation of the river between eruptive events (which have statistically correlative paleosecular variation) the slope value for the ancient Gila River preserved by SAVF is .001. The re-incision of the channel through the Oatman low shield lava dam was used to constrain the hydraulic radius and cross-sectional area of the paleochannel. The base of the wetted radius was extrapolated across the canyon based on elevation of the contact between SAVF lava flows and Gila River gravels. The wetted perimeter measurements assume that the canyon has not widened significantly from processes other than initial breach and the first terrace development. The lava dam cross-section is 4-5 km across that can be 40 m deep with river bed incision down to 23 m below the SAVF basal contact in some areas. There is rock fall and block-topple along the canyon, especially along upstream edges of major promontories. Measurements were taken in the straightest, narrowest portion of the canyon to minimize these effects (Figure 3).

The discharge represented by the identified geometry of the river channel cut through the Oatman low shield lava dam was calculated using the Manning Equation for open-channel, steady, uniform flow:

$Q = (1.49/n)\, AR^{2/3}S^{1/2}$, where:

Q=Discharge in cubic feet per second (cfs)

n= Manning's Roughness Coefficient

A= Cross-sectional area

R= Hydraulic radius (wetted perimeter)

S= Energy gradient, which matches the stream bed slope for uniform flow

The Manning Roughness Coefficient was calculated assuming sediment was the primary source of channel bed roughness using:

$n = [0.1129R^{1/6}*(1.15 + 2 \log(R/D_{84})]$ (Limerinos, 1970), where:

D_{84} = Sediment diameter that is larger than 84% of clasts

A minimum discharge of ~400,000 cfs is necessary to entrain the observed gravels using the Manning Equation, assuming the canyon width and 11 m height (top of lava flow to basal contact on both banks) represents the wetted perimeter of the paleoriver. The discharge calculation presented here includes several assumptions. First the calculation assumes constant velocity (steady), and constant depth (uniform, i.e., no bedforms) in a graded (Mackin, 1948) gravel river where the canyon is assumed to represent the remnant signature of a morphology from an episode of stability the river established after the final lava dam breach, representing dynamic equilibrium (Strahler, 1957) between sediment and water where local pools and riffles developed and the river librated laterally, but maintained a certain longitudinal profile over a period of years preceding later episodes of incision (Luna et al., 1992). Backwater deposition upstream of the dam suggests that the lava dam persisted for some length of time so the breach event potentially represents a catastrophic event. Alternatively, the length (4-5 km) of the canyon suggests it might have formed from long-lived overflow that incised upstream by undercutting the loose alluvium underneath the lava dam. Given the geology of the Gila River drainage basin, spring-time snow melt from the headwaters in the Colorado Plateau and Transition Zone is a possible culprit for the breach event, even during the Pleistocene. The calculation does not include any flow exceeding canyon bankfull.

Observed dimensionless Shields-type shear stress for gravel bed streams is typically measured at ~0.047 (Paola and Mohrig, 1996). Using this value Shields-type criterion for threshold of motion was calculated to compare to results from the Manning Equation for open-channel steady flow using Parker (1979):

$$\tau^* = \tau / \rho R g D_{50}$$

where:

τ= sheer stress= $\rho g H S$

ρ= density

H= depth

S= slope

R= submerged specific gravity [$(\rho_{sediment}/\rho_{water})$-1]

In order for the calculated Shields-type sheer stress to match the dimensionless value, the current width of the canyon would need to be flowing at 7.5 m depth to move the size of gravels preserved underneath the SAVF lava flows. However, the threshold sheer stress calculation is very sensitive to median grain size and should be viewed as an estimate. An increase of D_{50} from 10 cm to 15 cm would fill the canyon to 11 m. Clast counts were taken at only 3 (meter-square) exposures of the paleogravels and there could be a sampling or preservation bias. However, the calculated sheer stress for the threshold of movement of the observed Gila River sediment reasonably corresponds to expected values derived from observations of stable, graded gravel channels. This, along with the lithologies and rounding, implies that the canyon morphology and the resulting discharge values may represent a new stable channel developed by Gila River after the breach of the lava dam, and not just the catastrophic breach event itself.

Modeling paleolake terrace development

Lava dams would initiate backwater sediment aggradation, accumulating from an elevation range corresponding to the basal contact of the damming lava flow(s) to the maximum elevation of the damming lava flow(s). These paleolake terraces would be very flat and show no downstream grade, unlike paired erosional or strath terraces along a river channel. Local grade could also be affected even beyond the maximum extent of the sediment terrace if the paleolake sediment

terrace completely established. The upstream extent of the local knickpoint created by SAVF lava dams was modeled using 1-D backwater sediment calculations from Parker (2006). This was to check to see if slope values and extrapolated energy gradient at Gillespie low shield lava dam was potentially affected by emplacement of the Oatman low shield lava dam, because their exact relative timing is unknown. Ten to 11 m deep lava dams on the ancient Gila River would be felt ~50-100 km upstream (depending on flow rate), so the upstream energy gradient near Gillespie Dam was probably only minimally affected, if at all, by any downstream interactions between the river and SAVF eruptions. However, the alluvial deposits on the northern margin of Arlington low shield, 5 km upstream of Gillespie low shield lava dam, are well within the modeled sediment accumulation of Gillespie low shield lava dam. Modeled times for terrace development varied based on river characteristics, but typically were in the modeled time frame of months to a few years.

Interactions between the river and the Late Pliocene to early Pleistocene basaltic lava flows of the Sentinel-Arlington Volcanic Field (SAVF) provide insight into the hydrology of the ancient Gila River. The ancient Gila River was potentially similar in size and location to the current Gila River, with the exception that it potentially initially flowed south of the Painted Rock Mountains, ~20 km south of where it currently crosses the northern Painted Rock Mountains. Early SAVF eruptions interacted with the now abandoned southern paleochannel, potentially forming the Citrus Valley paleolake at ~222 m, and eventually diverted it to a new channel that crossed the northern Painted Rock Mountains. The SAVF then dammed the northern channel multiple times, forming a potentially reoccurring paleolake at ~175 m elevation in the Dendora lava dam area as evidenced by pillow lavas, lava dams, and very flat sediment terraces. The river discharge calculated to establish the youngest canyon incised through the SAVF in the Oatman low shield lava dam area was calculated to be ~400,000 cfs based on channel morphology and grain size of Gila River gravels. Notably, this value is comparable to historic records of the maximum flood event along the Gila River in 1891 of 300,000+ cfs. SAVF also dammed and diverted the Gila River in the Gillespie low shield lava dam locality. The relative timing of this event is unclear, but can be

paleomagnetically correlated with the Oatman LS lava dam locality, which was dated as 2.30 Ma ± 0.035 Ma. Also, the Arlington low shield volcano erupted onto the Sawik terrace of Péwé (1978), and has been dated to 2.37 Ma +- 0.02 Ma, which means the terrace is at least of early Pleistocene age and potentially older.

Chapter 6

SUMMARY AND CONCLUSIONS

SAVF began eruptive activity by at least ~2.3 Ma and lasted until ~1.1 Ma, damming and diverting the lower Gila River at least twice. The North American plate has been moving northwest to west 2-3 cm/yr since the Pliocene (Luedke and Smith, 1978; Smith and Luedke, 1984; Tanaka et al., 1986), which would result in a 35+ km migration to the west during the eruption period of SAVF, but there is no obvious eastward migration of SAVF vents recorded in the current geochronology data. In fact, the 5 radiogenic results alone might suggest a temporal-geographic trend of older events beginning on the northeast quadrant of the field with and younger events extending to the southwest. However, the paleomagnetic correlations connect multiple eruptive events and reveal that this trend is probably an artifact of sampling (for example: Correlation E in Figure 4 shows events occurring in both the NE and SW sectors simultaneously). In Arizona, eastward migrations of volcanic vents have been documented by Luedke and Smith (1978) who noted an eastward migration in the general trend of volcanic fields since the Miocene, by Tanaka et al. (1986) within the San Francisco volcanic field, and Best and Brimhall (1974) for the Uinkaret volcanic field, though most preserved fields along the Jemez structural Zone and the Colorado Plateau do not show vent migration (Laughlin, 1976; Tanaka, et al., 1986). The lack of vent migrations was suggested by Tanaka et al. (1986) to be primarily related to intersections of major structural weaknesses with high heat flow from the mantle or lower crust. Structural weaknesses influencing SAVF could be NW-SE trending Basin and Range structures, NE-SW trending Paleozoic crustal suture (Goetz et al., 1985; Karlstrom and Humphreys, 1998, correlative with the Jemez lineament of volcanic fields from Sonora, Mexico to New Mexico (Laughlin et al., 1979)); and/or the Sea of Cortez spreading zone (Gastil et al., 1979; Angelier et al., 1981; Dokka et al., 1982; etc.).

SAVF is a good potential analogue to small-volume effusive volcanic centers on Mars, such as those seen the southern flank of Pavonis Mons and in the Tempe Terra region on Mars in

Mars Express High Resolution Stereo Camera (HRSC) images and Thermal Emission Imaging System (THEMIS) visible images, for several reasons. The SAVF lavas are lightly mantled by aeolian dust and basaltic rubble, similar to martian surfaces. The SAVF also represent basaltic plains-style volcanism, an emplacement style of volcanism intermediate between classic flood volcanism and large shield-building volcanism which has been previously recognized on Mars.

REFERENCES

Anderson, K., Wells, S., and Graham, R., 2002, Pedogenesis of vesicular horizons, Cima Volcanic Field, Mojave Desert, California: Soil Science Society of America Journal, v. 66, p. 878–887, doi:10.2136/sssaj2002.8780

Angelier, J., Colleta, B., Chorowicz, L., Ortlieb, L., and Rangin, C., 1981, Fault tectonics of the Baja California peninsula and the opening of the Sea of Cortez, Mexico: Journal of Structural Geology, v. 3, pp. 347–357.

Bachman, G.O., and Machette, M.N., 1977, Calcic soils and calcretes in the southwestern United States: U.S. Geological Survey Open-File Report 77–794, 163 p.

Best, M. G., and Brimhall, W. H., 1974, Late Cenozoic alkalic basaltic magmas in the western Colorado Plateau and the Basin and Range transition zone, U.S.A., and their bearing on mantle dynamics, Geol. Soc. Of America Bull., v. 85, p. 1677-1690.

Bloxham, J., and Gubbins, D.,1985, The secular variation of the Earth's magnetic field, Nature v. 317, pp. 777-781.

Bloxham, J., and Jackson, A., 1992, Time-dependent mapping of the magnetic field at the core-mantle boundary, J. Geophys. Res., v. 97, pp. 19537-19563.

Bloxham, J., 2000, The effect of thermal core-mantle interactions on the paleomagnetic secular variation, Phil. Trans. R. Soc. Lond., A358, pp. 1171-1179.

Brown, L., Caffall, N., and Golombek, M., 1993, Paleomagnetism and tectonic interpretations of the Taos Plateau Volcanic Field, Rio Grande Rift, New Mexico, J. Geophys. Res., v. 98, no. 22, pp. 401–422.

Butler, R. F., 1992, Paleomagnetism: Magnetic Domains to Geologic Terranes, Blackwell Sci., Malden, Mass.

Cave, S. R., Greeley, R., Champion, D. E., Turrin, B. D., 2007, 40Ar/39Ar ages for the Sentinel-Arlington Volcanic Field, southwestern Arizona, Eos Trans. AGU, 88(52) Fall Meeting Suppl., Abstract V23B-1439.

Cave, S. R., and Greeley, R., 2004, The geology of two small Cenozoic volcanoes in southwestern Arizona, J. of Arizona-Nevada Academy of Science, Vol. 37, No. 2, pp. 105-110.

Cave, S.R., 2004, The geology of two small Cenozoic volcanoes in southwestern Arizona: Phoenix, Arizona State University, M.S. thesis, 49 p.

Champion, D., 1980, Holocene geomagnetic secular variation in the Western United States: Implications for the global geomagnetic field, U.S. Geol. Surv. Open File Rep. 80-824, pp. 314–354.

Chronic, H., 1983, *Roadside Geology of Arizona*, Mountain Press: Missoula, MT, 314 p.

Connor, C.B., Condit, C.D., Crumpler, L.S., and Aubele, J.C., 1992, Evidence of regional structural controls on vent distribution: Springerville volcanic field, Arizona: Journal of Geophysical Research, v. 97, p. 12,349-12,359.

Conway, F.M., Ferrill, D.A., Hall, C.M., Morris, A.P., Stamatakos, J.A., Connor, C.B., Halliday, A.N. and Condit, C., 1997, Timing of basaltic volcanism along the Mesa Butte Fault in the San Francisco Volcanic Field, Arizona, from 40Ar/39Ar dates: Implications for longevity of cinder cone alignments: Journal of Geophysical Research, v. 102: doi: 10.1029/96JB02853.

Crumpler, L.S., Aubele, J.C., and Condit, C.D., 1994, Volcanoes and neotectonic characteristics of the Springerville volcanic field, Arizona, *in* Chamberlin, R.M., Kues, B.S., Cather, S.M., Barker, J.M., and McIntosh, W.C., eds., Mogollon Slope, west-central New Mexico and east-central Arizona: New Mexico Geological Society 45th Field Conference Guidebook, p. 147-164.

Damon P.E., Lynch, D.J., and Shafiquallah, M., 1984, Cenozoic landscape development in the Basin and Range province of Arizona, *in* Smiley, T.L., and others, eds., Landscapes of Arizona, the Geologic Story: Lanham, Maryland, University Press of America, p. 175-206.

Demsey, K.A., 1989, Geologic map of Quaternary and upper Tertiary alluvium in the Phoenix South 30' x 60' quadrangle, Arizona (revised August, 1990): Arizona Geological Survey, Open-File Report OFR 89-07, scale 1:100,000.

Demsey, K.A., 1990, Geologic map of Quaternary and upper Tertiary alluvium in the Little Horn Mountains 30' x 60' quadrangle, Arizona: Arizona Geological Survey, Open-File Report OFR 90-08, scale 1:100,000.

Doell, R., Dalrymple, G., Smith, R., and Bailey, R.,1968, Geology of rhyolites and associated rocks of the Valles Caldera, New Mexico, Mem. Geol. Soc. Am., v. 116, pp. 211–248.

Dohrenwend, J.C., Wells, S.G., Turrin, B.D., and McFadden, L.D., 1984, Rates and trends of late Cenozoic landscape degradation in the area of the Cima volcanic field, Mojave Desert, California, in, *Surficial Geology of the Eastern Mojave Desert, California*: Dohrenwend, J.C. (ed.),Geological Society of America, 1984 Annual Meeting, Field Trip 14 Guidebook, p. 101-115.

Dokka, R. K., and Merriam, R. H., 1982, Late Cenozoic extension of northeastern Baja California, Mexico: Geol. Soc. of America Bull., v. 93, pp. 371–378.

Eberly, L.D. and Stanley, T.B., 1978, Cenozoic stratigraphy and geologic history of southwestern Arizona, Geol. Soc. of America Bull., v. 89, no. 6, pp. 921-940.

Francis, P., and Oppenheimer, C., 2004, Volcanoes, 2nd edition, Oxford University Press: New York, New York, 521 p.

Gastil, R. G., Krummenacher, D., and Minch, J., 1979, The record of Cenozoic volcanism around the Gulf of California: Geol. Soc. of America Bull., v. 90, p. 839–857.

Geissman, J., 1988, Paleomagnetism and rock magnetism of Quaternary volcanic rocks and Late Paleozoic strata, VC-1 Core Hole, Valles Caldera, New Mexico, with emphasis on remagnetization of Late Paleozoic strata, J. Geophys. Res., v. 93, pp. 6001–6025.

Geissman, J., Brown, L., Turrin, B., McFadden, L., and Harlan, S., 1990, Brunhes chron excursion/polarity episode recorded during the late Pleistocene, Albuquerque Volcanoes, New Mexico, USA, Geophys. J. Int., v. 102, pp. 73–88.

Gibbard, P. L., Head, M. J., and Walker, M. J. C., 2009, Formal ratification of the Quaternary System/Period and the Pleistocene Series/Epoch with a base at 2.58 Ma, J. of Quat. Sci., vol. 25, no. 2, pp. 96-102.

Gile, L. H., Peterson, F. F., and Grossman, R. B., 1966, Morphological and genetic sequences of carbonate accumulation in desert soils: Soil Science, v. 101, no. 5, p. 347-360.

Goetz, L.K. and Dickerson, P.W., 1985, A Paleozoic transform margin in Arizona, New Mexico, west Texas and northern Mexico. In: Dickerson, P.W. and Muehlberger, W.R., Editors, 1985, Structure and tectonics of Trans-Pecos Texas, West Texas Geological Society, Midland, TX, Publication 85-81, pp. 173–184.

Greeley, R., 1977, Basaltic "Plains" Volcanism, in Greeley, R., and King, J.S., eds., Volcanism of the eastern Snake River Plain: A Comparative Planetary Geology Guidebook, NASA CR-154621.

Greeley, R., 1982, The Snake River Plain, Idaho: Representative of a new category of volcanism, Journal J. Geophys. Res., v. 87, pp. 2705-2712.

Heinrichs, D., 1967, Paleomagnetism of the Plio-Pleistocene Lousetown Formation, Virginia City, Nevada, J. Geophys. Res., v. 72, pp. 3277–3293.

Karlstrom, K., E, and Humphreys, E., D., 1998, Persistent influence of the Proterozoic accretionary boundaries in the tectonic evolution of the southwestern North America: Interaction of cratonic grain and mantle modification events, Rocky Mtn. Geol., v. 33, no. 2, pp. 161-179.

Kono, M., K. Kobayashi, M. Ozima, H. Kinoshita, T. Nagata, E. Larson, and Strangway, D., 1967, Paleomagnetism of Pliocene basalts from the south-western U.S.A., J. Geomagn. Geoelectr., v. 19, pp. 357–375.

Lee, G. K. and Bell, J., 1975, Late Cenozoic geology along the Gila River near Gillespie Dam, Central Arizona, [abstract] *GSA Abs w/Programs*, v. 7, no. 3, p. 340.

Leeman, W. P., 1970, The isotopic composition of strontium in late-Cenozoic basalts from the Basin-Range province, western United States, Geoch. et Cosmoch. Acta, v. 34, no. 8, pp. 857-872.

Laughlin, A. W., 1976, Late Cenozoic volcanism along the Jemez zone of New Mexico and Arizona: Geol. Soc. Of America Abs. w/Programs, v. 8, p. 598.

Laughlin, A. W., Brookins, D. G., Damon, P. E., and Shafiqullah, M., 1979, Late-Cenozoic volcanism of the central Jemez zone, Arizona-New Mexico, Isochron/ West no. 25, pp. 5-8.
Limerinos, J. T., 1970, Determination of the manning coefficient from measured bed roughness in natural channels, *U.S. Geological Survey Water- Supply Paper 1898-B*., 47 p.

Luedke, R. G., and Smith, R. L., 1978, Map showing distribution, composition, and age of late Cenozoic volcanic centers in Arizona and New Mexico, U. S. Geol. Surv. Misc. Investigations Series Map I-1091-A.
Luna, L., 1992,

Lynch, D. J., 1989, Neogene volcanism in Arizona: The recognizable volcanoes, in Jenney, J.P., and Reynolds, S.J., eds., Geologic evolution of Arizona: Arizona Geological Society Digest 17, pp. 681-700.

Lynch, D. J., 1990, in Wood, C. A., and Kienle, J., eds., Volcanoes of North America: United States and Canada, Cambridge University Press, 354 p.

Machette, M.N., 1985, Calcic soils of the southwestern United States, *in* Weide, D.L., and Faber, M.L., eds., Soils and Quaternary geology of the southwestern United States: Geological Society of America Special Paper 203, p. 1-21.

Maniken, E. A., 2008, Paleomagnetic study of late Miocene through Pleistocene igneous rocks from the southwestern USA: Results from the historic collections of the U.S. Geologica Survey Menlo Park Laboratory, Geochem. Geophys. Geosyst., v. 9, no. 5, Q05017.

Morrison, R. B., 1985, Pliocene/Quaternary geology, geomorphology, and tectonics of Arizona, Geologic Society of America Special Paper 203, pp. 123-146.

Ogg, J. G., and Smith, A. G., 2004, The geomagnetic polarity time scale, in Gradstein, F., Ogg, J., and Smith A., eds., 2004, A geologic time scale 2004: Cambridge, U.K., Cambridge University Press, 589 p., 1 pl..

Paola, C. and Mohrig, D., 1996, Paleohydraulics revistited: paleoslope estimation in coarse-grained braided rivers, *Basin Research*, Vol. 8, pp. 243-254.

Parker, G., (in press) 1D sediment transport morphodynamics with applications to rivers and turbidity currents, http://cee.uiuc.edu/people/parkerg/morphodynamics_e-book.htm
Parker, G., 1979, Hydraulic geometry of active gravel rivers, *Journal of the Hydraulics Div: ASCE*, v. 105, no. HY9, pp. 1185-1200.

Peters, L., 2006, $^{40}Ar/^{39}Ar$ Geochronology Results from Southwestern Arizona Basalts, NMGRL-IR-523, 4 p.

Peterson, J.A., Miller, R.J., and Jones, S.L, 1989, Geologic Map of the Woolsey Peak Wilderness Study Area, Maricopa County, Arizona: United States Geological Survey Map, scale 1:48,000.

Péwé, T.L., 1978, Terraces of the lower Salt River Valley in relation to the late Cenozoic history of the Phoenix basin, Arizona, *in Guidebook to the Geology of Central Arizona*: *Arizona Bureau of Geology and Mineral Technology Special Paper 2*, edited by D. M. Burt and T. L. Péwé, p. 221-226.

Price, D., 1958, William Gilbert and his De Magnete, Basic Books, New York, New York.

Reynolds, S. J., Florence, F. P., Welty, J. W., Roddy, M. S., Currier, D. A., Anderson, A. V., and Keith, S. B., 1986, Compilation of K-Ar age determinations in Arizona, Arizona Bureau of Geology and Mineral Tech. Open-File Report 85-8, 320 p.

Reynolds, S. J., 1988, Geologic Map of Arizona, Arizona Geological Survey Map 26, 1:1,000,000.

Reynolds, S. J., and Skotnicki, S. J., 1993, Geologic map of the Phoenix South 30' x 60' quadrangle, central Arizona, Arizona Geological Survey Open-File Report 93-18, 1:100,000.

Richard, S.M., Reynolds, S.J., Spencer, J.E., and Pearthree, P.A., 2000, Geologic Map of Arizona: Arizona Geological Survey Map, scale 1:1,000,000.

Scarborough, R. B., Menges, C., M., and Pearthree, P. A., 1986, Map of late Pliocene-Quaternary (post 4 Ma) faults, folds, and volcanic outcrops in Arizona: AZ Bureau of Geology and Mineral Tech., Map 22, scale 1:1, 000, 000.

Schoustra, J.J., Smith, J.L., Scott, J.D., Strand, R.L., and Duff, D., 1976, Radiometric age dating: Palo
Verde Nuclear Generating Station 1, 2, and 3, Preliminary safety analysis report: Arizona Public Service Commission, v. 8, Appendix 2Q.

Scotnicki, S., 1993a, Geologic Map of Face Mountain and Oatman Mountain, South-Central Gila Bend Mountains, Maricopa County, Arizona: Arizona Geological Survey Map, scale 1:50,000.

Scotnicki, S., 1993b, Geologic Map of the Painted Rock Mountains, Maricopa County, Arizona: Arizona Geological Survey Map, scale 1:24,000.

Scotnicki, S., 1994, Compilation Geologic Map of the Central Gila Bend Mountains, Maricopa County, Arizona: Arizona Geological Survey Map, scale 1:50,000.

Scott, R. F. and Schoustra, J. J., 1974, Nuclear power plant sitting on deep alluvium, J. of the Geotech. Eng. Div., v. 100, no. 4, pp. 449-459.

Shafiqullah, M., Damon, P. E., Lynch, D. J., Reynolds, S. J., Rehrig, W. A., and Raymond, R. H., 1980, K-Ar geochronology and geologic history of southwestern Arizona and adjacent areas, in Jenney, J.P., and Stone, Claudia, eds., Studies in western Arizona: Arizona Geological Society Digest, v. 12, pp. 201-260.

Sheridan, M. F., 1984, Volcanic landforms, in Smiley, T. L., Nations, J. D., Pewé, T. L., and Schafer, J. P., eds., Landscapes of Arizona - The geological story: Lanham, Md., University Press of America, pp. 79-109.

Shoemaker, E. M., and Champion, D. E., 1977, Eruption history of Sunset Crater, Arizona, Investigator's annual report. Manuscript on file, Area National Monuments Headquarters, Wupatki, Sunset Crater Volcano, and Walnut Canyon National Monuments, Flagstaff, Arizona.

Smith, R. L., and Luedke, R. G., 1984, Potentially active volcanic lineaments and loci in western conterminous United States, in Geophysics Study Committee, ed., Explosive volcanism: Inception, evolution, and hazards, Washington, D. C., Nat'l Academy Press, pp. 47-66.

Spencer, J.E., 1995, Geologic map of the Little Horn 30' x 60' Quadrangle, southwestern Arizona: Arizona Geological Survey, Open-File Report 95-1, scale 1:100,000.

Spencer, J.E., 2013, A review of late Cenozoic volcanic activity in the Gila Bend – Buckeye area of western Maricopa County, Arizona: Arizona Geological Survey Open-File Report OFR-13-07, 34 p.

Spencer, J. E., Patchett, P. J., 1997, Sr isotope evidence for a lacustrine origin for the upper Miocene to Pliocene Bouse Formation, lower Colorado trough, and implications for timing of Colorado Plateau uplift, *Geol. Soc. Am. Bull.* v. 109, pp. 767–778.

Tanaka, K., Onstott, T., and Shoemaker, E., 1990, Magnetostratigraphy of the San Francisco Volcanic Field, Arizona, U.S. Geol. Surv. Bull., v. 1929, 1–35.

Tanaka, K., Shoemaker, E., Ulrich, G., and Wolfe, E., 1986, Migration of volcanism in the San Francisco volcanic field, Arizona: Geological Society of America Bulletin, v. 97, pp, 129-141.

Tauxe, L., C. Constable, C. L. Johnson, A. A. P. Koppers, W. R. Miller, and H. Staudigel, 2003, Paleomagnetism of the southwestern U.S.A. recorded by 0–5 Ma igneous rocks, Geochem. Geophys. Geosyst., v. 4, no. 4, 8802.

Thompson, G. A., and Zoback, M. L., 1979, Regional geophysics of the Colorado Plateau, in McGetchin, T. R., and Merril, R. B., eds., Plateau uplift: Mode and mechanism, Tectonphysics, v. 61, pp. 149-191.

Ulrich, G. E., and Nealy, L. D., 1976, Structural and eruptive patterns in the San Francisco volcanic field, northern Arizona, Geologic Society of America Abstracts with Programs, v. 8, pp. 641-642.

Wells, S.G., Dohrenwend, J.C., McFadden, L.D., Turrin, B.D., and Mahrer, K.D., 2005, 1985, Late Cenozoic landscape evolution on lava flow surfaces of the Cima volcanic field, Mojave Desert, California: Geological Society of America Bulletin, v. 96, p. 1518-1529.

Wilson, E. D., 1960, Geologic map of Yuma County, Arizona: Arizona Bureau of Mines, 1 sheet, scale 1:375,000.

Wilson E. D., Moore, R. T., and Copper, J. R., 1969, Geologic map of the State of Arizona: Arizona Bureau of Mines, Univ. of Arizona, scale 1: 500,000.

Wilson, E. D., Moore, R. T., and Peirce, H. W., 1957, Geologic map of Maricopa County, Arizona: Arizona Bureau of Mines, 1 sheet, scale 1:375,000.

Wolfe, E. W., Ulrich, G. E., and Moore, R. B., 1983, San Francisco volcanic field, Arizona, Volcano News, no. 13, pp. 1-3.

APPENDIX A

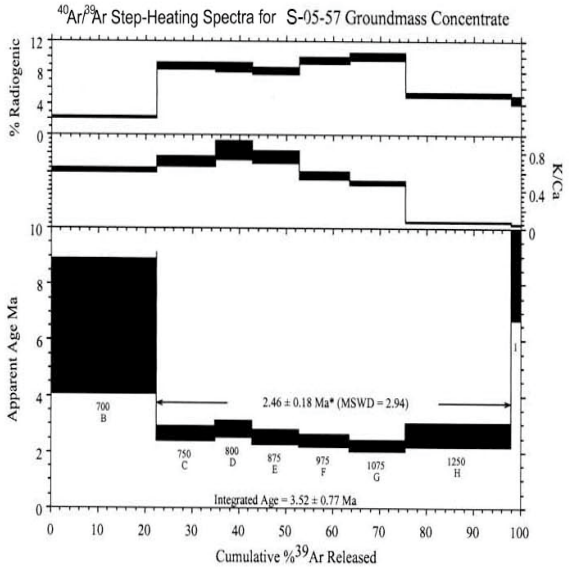
PALEOMAGNETIC DATA TABLES

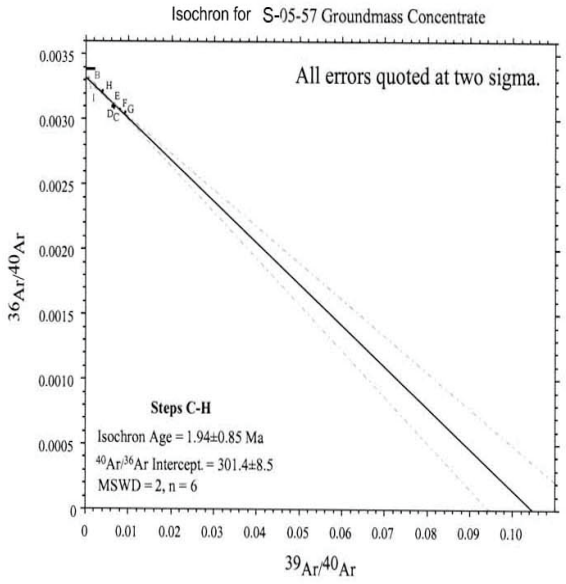
Site	Lat.	Long.	N/No	Exp.	I	D	a95	k	R	Plat.	Plong.
448B5	32.871°	246.863°	8/8	Pl	-65.8°	226.4°	12.5°	66	.----	-52.3°	119.1°
009B7	32.911°	246.820°	8/8	Pl	-38.1°	161.8°	1.8°	1149	.----	-70.2°	305.9°
065B7	32.906°	246.876°	8/8	Pl	-36.8°	164.2°	3.4°	216	.----	-71.3°	299.41°
065A6	32.826°	246.793°	7/8	20+	-62.6°	196.5°	2.2°	785	6.99235	-73.0°	111.1°
073A6	32.842°	246.781°	7/8	Pl	-64.1°	181.4°	2.6°	439	.----	-77.0°	71.1°
081A6	32.814°	246.760°	8/8	Pl	-54.9°	178.6°	4.9°	109	.----	-87.1°	43.3°
097A6	32.796°	246.725°	8/8	Pl	-60.3°	196.3°	3.8°	190	.----	-74.5°	119.0°
057A6	32.838°	246.797°	8/8	Pl	-63.0°	197.6°	2.5°	472	.----	-72.1°	111.3°
105A6	32.825°	246.703°	8/8	Pl	-63.4°	192.3°	2.4°	927	.----	-74.6°	101.3°
432B5	32.890°	246.933°	8/8	20	-65.1°	186.3°	1.2°	2232	7.99686	-75.0°	83.6°
049B7	32.923°	246.904°	8/8	Pl	-65.9°	175.0°	3.1°	420	.----	-74.3°	54.5°
057B7	32.920°	246.902°	8/8	Pl	-64.3°	178.3°	4.8°	127	.----	-74.3°	61.8°
001A6	32.820°	246.794°	8/8	Pl	-54.4°	201.5°	2.1°	577	.----	-72.1°	144.1°
073B7	32.856°	246.791°	8/8	Pl	-48.9°	189.6°	2.4°	523	.----	-81.3°	174.6°
081B7	32.844°	246.811°	8/8	Pl	-47.7°	201.1°	3.3°	565	.----	-71.5°	163.8°
025B7	33.008°	246.827°	8/8	Pl	-56.1°	187.8°	1.3°	1632	.----	-82.6°	125.0°
001B7	32.962°	246.831°	8/8	Pl	-55.4°	191.8°	1.1°	2078	.----	-79.8°	136.6°
017B7	32.909°	246.856°	8/8	Pl	-41.1°	165.0°	5.7°	102	.----	-73.9°	305.4°
097B7	32.906°	246.838°	8/8	Pl	-37.1°	164.3°	4.7°	129	.----	-71.5°	299.6°
105B7	32.919°	246.714°	8/8	Pl	-40.1°	187.3°	4.0°	300	.----	-78.0°	212.3°
130B7	32.883°	246.800°	8/8	Pl	-43.7°	187.0°	1.5°	1242	.----	-80.5°	205.3°
456B5	32.934°	246.699°	7/8	Pl	-43.1°	195.4°	3.5°	323	.----	-74.4°	183.0°
592B5	32.965°	246.749°	12/12	Pl	-38.8°	190.0°	4.2°	111	.----	-75.8°	205.6°
440B5	32.878°	246.885°	8/8	Pl	-43.5°	177.1°	3.3°	281	.----	-82.1°	266.3°
049A6	32.869°	246.875°	8/8	Pl	-45.0°	179.9°	2.1°	743	.----	-83.7°	247.7°
089A6	32.771°	246.746°	7/8	20	-46.6°	178.8°	2.3°	704	6.99148	-85.0°	258.8°
464B5	32.918°	246.641°	7/8	Pl	-38.8°	174.6°	1.4°	1501	.----	-78.0°	271.5°
472B5	32.892°	246.662°	8/8	Pl	-36.3°	170.8°	1.8°	819	.----	-74.9°	281.7°
033A6	32.885°	246.767°	7/8	Pl	-26.1°	160.4°	6.1°	108	.----	-63.8°	294.4°
025A6	32.871°	246.577°	6/8	20+	-36.4°	175.0°	3.8°	316	5.9842	-72.0°	51.2°
113B7	32.901°	246.744°	8/8	20+	-31.9°	173.8°	1.9°	900	7.99223	-73.4°	268.1°
512B5	33.236°	247.219°	8/8	Pl	-55.3°	184.7°	2.7°	527	.----	-85.3°	122.1°
520B5	33.229°	247.225°	8/8	Pl	-48.9°	187.4°	1.4°	1461	.----	-82.8°	183.6°
138B7	33.226°	247.178°	8/8	30+	-56.6°	187.2°	2.0°	811	7.99137	-82.9°	121.3°
154B7	33.216°	247.208°	8/8	20	-53.7°	185.9°	1.3°	1976	7.99646	-85.0°	144.2°
480B5	33.328°	247.242°	8/8	Pl	-31.4°	185.7°	2.3°	642	.----	-72.9°	228.4°
488B5	33.321°	247.258°	8/8	Pl	-33.0°	190.8°	3.4°	738	.----	-71.9°	212.3°
496B5	33.355°	247.264°	8/8	30+	-32.7°	188.6°	2.2°	637	7.989	-72.6°	218.7°
504B5	33.353°	247.224°	8/8	Pl	-33.4°	183.2°	2.6°	710	.----	-74.6°	235.7°
009A6	33.348°	247.253°	5/8	Pl	-30.7°	187.6°	3.2°	576	.----	-71.9°	223.2°
528B5	33.019°	247.002°	7/9	Pl	-30.0°	173.4°	1.1°	3035	.----	-72.2°	266.8°

089B7	32.900°	247.014°	8/8	Pl	-44.4°	181.6°	1.2°	2166	.----	-83.1°	235.1°
170B7	32.899°	247.046°	8/8	30+	-47.5°	182.2°	2.9°	360	7.98053	-85.4°	222.3°
146B7	33.156°	247.075°	8/8	30	-47.1°	205.7°	2.8°	393	7.98221	-67.4°	162.7°
537B5	33.003°	246.944°	9/9	Pl	50.3°	359.9°	2.2°	486	.----	88.1°	69.5°
546B5	32.975°	246.938°	8/8	Pl	43.7°	359.3°	2.9°	320	.----	82.5°	71.8°
554B5	32.989°	246.912°	10/11	Pl	44.2°	3.1°	2.7°	362	.----	82.4°	45.2°
565B5	32.989°	246.912°	8/8	Pl	45.6°	2.8°	2.1°	685	.----	83.6°	44.0°
604B5	32.984°	246.850°	8/8	30	50.4°	4.6°	1.5°	1310	7.99466	85.7°	1.3°
612B5	32.984°	246.850°	8/8	30	49.6°	359.5°	1.4°	1497	7.99532	87.4°	77.2°
574B5	33.024°	246.828°	5/8	Pl	35.9°	0.8°	4.7°	199	.----	76.9°	63.5°
584B5	33.029°	246.845°	7/8	Pl	43.4°	6.8°	3.9°	267	.----	80.3°	27.6°
033B7	33.027°	246.828°	7/8	Pl	45.2°	3.6°	3.0°	328	.----	83.0°	39.6°
041B7	33.024°	246.827°	8/8	Pl	35.7°	2.7°	3.9°	233	.----	76.5°	55.9°
162B7	32.849°	246.926°	8/8	30+	53.6°	4.4°	2.7°	416	7.98318	86.1°	315.8°

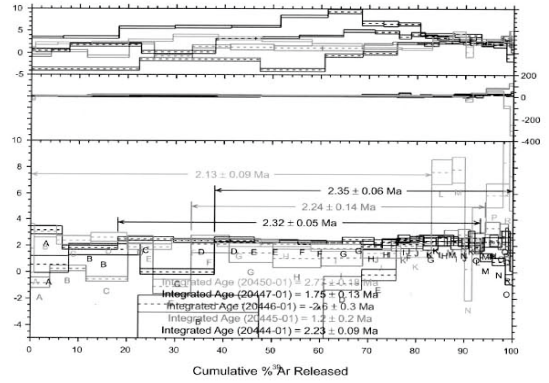
APPENDIX B

AGE SPECTRA AND ISOCRON PLOTS FOR S-05-57 (NEW MEXICO GEOCHRONOLOGICAL RESEARCH LABORATORY; AND S-06-180C, S-06-183D, S-06-186C, AND S-06-194 (RUTGERS NOBLE GAS LABORATORY)

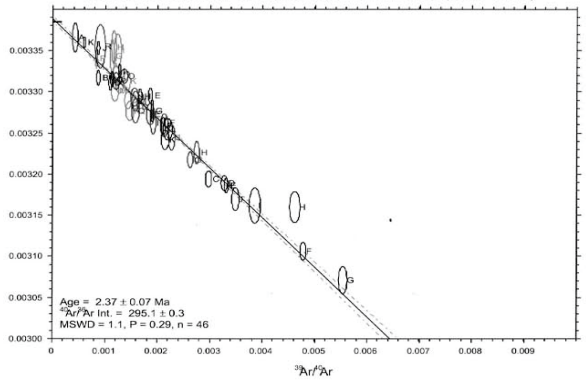

$^{40}Ar/^{39}Ar$ Step-Heating Spectra for S-05-57 Groundmass Concentrate
% Radiogenic
K/Ca
Apparent Age Ma
2.46 ± 0.18 Ma* (MSWD = 2.94)
Integrated Age = 3.52 ± 0.77 Ma
700 B
750 C
800 D
875 E
975 F
1075 G
1250 H
I
Cumulative $\%^{39}Ar$ Released


Isochron for S-05-57 Groundmass Concentrate
All errors quoted at two sigma.
$^{36}Ar/^{40}Ar$
$^{39}Ar/^{40}Ar$
Steps C-H
Isochron Age = 1.94±0.85 Ma
$^{40}Ar/^{36}Ar$ Intercept. = 301.4±8.5
MSWD = 2, n = 6

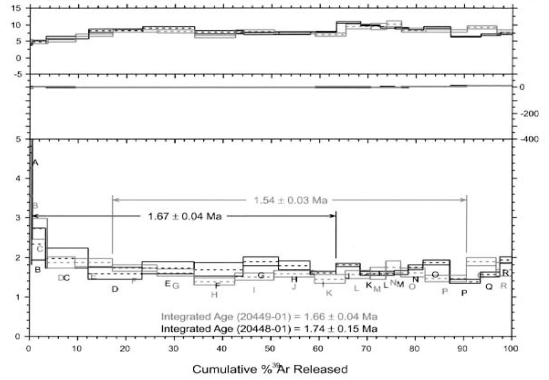
$^{40}Ar/^{39}Ar$ Step-Heating Spectra for Runs 20444, 20445, 20447, 20450 (S-06-180C)



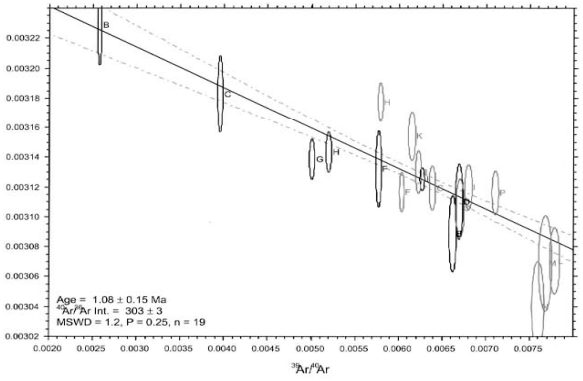
Isochron for Runs 20444, 20445, 20447, 20450 (S-06-180C)



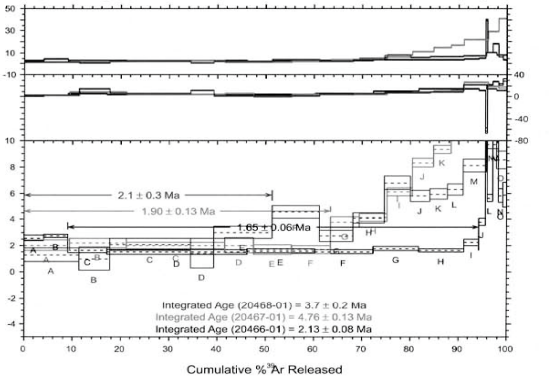
$^{40}Ar/^{39}Ar$ Step-Heating Spectra for Runs 20448-01, 20449-01 (S-06-183D)



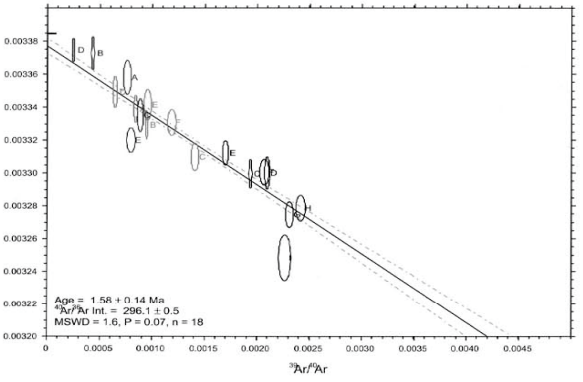
Isochron for Runs 20448, 20449 (S-06-183D)



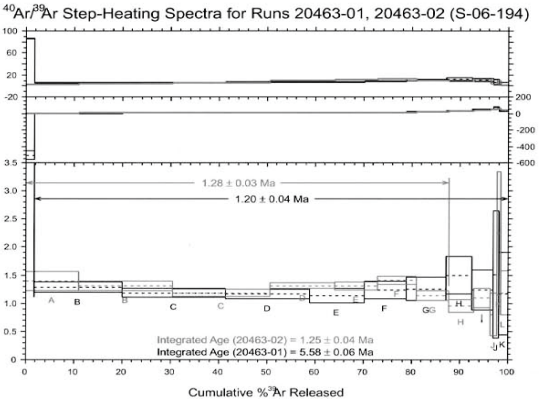
$^{40}Ar/^{39}Ar$ Step-Heating Spectra for Runs 20466-01, 20467-01, 20468-01 (S-06-186C)



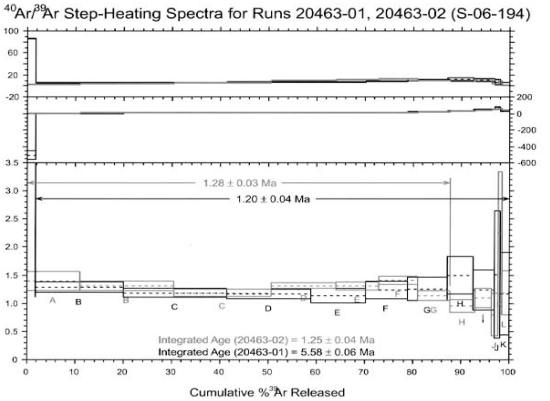
Isochron for Runs 20466, 20467, 20468 (S-06-186C)



$^{40}Ar/^{39}Ar$ Step-Heating Spectra for Runs 20463-01, 20463-02 (S-06-194)



$^{40}Ar/^{39}Ar$ Step-Heating Spectra for Runs 20463-01, 20463-02 (S-06-194)



APPENDIX C

GEOCHRONOLOGY RESULTS FROM SOUTHWESTERN ARIZONA BASALTS

NMGRL

$^{40}Ar/^{39}Ar$ Geochronology Results from Southwestern Arizona Basalts

By

Lisa Peters

MAY 11, 2006

Prepared for

Shelby Cave
Department of Geological Sciences
Planetary Geology Group
Box 871404
Tempe, AZ 85287-1404

NEW MEXICO
GEOCHRONOLOGY RESEARCH LABORATORY
(NMGRL)

CO-DIRECTORS

DR. MATTHEW T. HEIZLER

DR. WILLIAM C. MCINTOSH

LABORATORY TECHNICIANS

LISA PETERS

RICHARD P. ESSER

Internal Report #: NMGRL-IR-523

Introduction

Two basalt samples from southwestern Arizona were submitted for dating by Shelby Cave of Arizona State University. The sample numbers, materials dated and age assignments are briefly summarized in Table 1.

Table 1. Brief summary of results.

Sample	Phase	Location	Age±2σ (Ma)	Comments
505-57	Groundmass Concentrate	southwestern Arizona	1.94±0.85	isochron age
505-66	Groundmass Concentrate	southwestern Arizona	22.4±1.0	isochron age

$^{40}Ar/^{39}Ar$ Analytical Methods and Results

The rock samples were crushed and cleaned with dilute HCl and distilled water. The groundmass concentrates were then prepared with standard heavy liquid, magnetic separator and handpicking techniques. The samples were loaded into aluminum discs and irradiated for 1 hour at the Nuclear Science Center in College Station, Texas.

Groundmass concentrates were analyzed with the furnace incremental heating age spectrum method. Abbreviated analytical methods for the dated samples are given in Table 2, and details of the overall operation of the New Mexico Geochronology Research Laboratory are provided in the Appendix. The age results are summarized in Tables 1 and 2 and argon isotopic data are given in Table 3.

505-57 Isochron Age=1.94±0.85 Ma n/n_{total} =6/8 MSWD=2
Sample 505-57 yielded a somewhat disturbed saddle-shaped age spectrum with old apparent ages in the early and late heating steps (Figure 1a). A weighted mean age of 2.46±0.18 Ma is calculated from the flattest mid-portion of the age spectrum. The radiogenic yields and K/Ca values exhibit an inverse correlation with the apparent ages, rising dramatically where the apparent ages decrease and dropping as the apparent ages begin to rise. Points C-H were evaluated with the inverse isochron technique and revealed an isochron age of 1.94±0.85 Ma with a $^{40}Ar/^{36}Ar$ intercept of 301.4±8.5, within error of the atmospheric intercept of 295.5 (Figure 1b). The data form a fairly well defined linear array as indicated by the MSWD value of 2 (a value over one indicates scatter in the data not attributable to analytical error alone).

505-66 Isochron Age=22.4±1.0 Ma n/n_{total} =10/10 MSWD=8.7

Sample 505-66 also yielded a somewhat disturbed age spectrum with old apparent ages in the early steps and to a lesser extent in the final heating steps (Figure 2a). A weighted mean age of 22.46±0.18 Ma is calculated from the flattest mid-portion of the age spectrum. As with 505-57, the radiogenic yields and K/Ca values reveal an inverse correlation with the apparent ages. Inverse isochron analysis of steps A-J reveals an isochron age of 22.4±1.0 Ma with a $^{40}Ar/^{36}Ar$ intercept of 299±12 (Figure 2b). We note that the large MSWD value (8.7) indicates scatter in the data well outside of analytical error.

Discussion

Saddle-shaped age spectra, such as these, have been shown to be the result of excess Ar, also indicated by $^{40}Ar/^{36}Ar$ isochron intercept values greater than the atmospheric intercept (Harrrison and McDougall, 1981). Although the $^{40}Ar/^{36}Ar$ intercepts are within error of the atmospheric ratio we feel the isochron ages are our best estimates of the age of eruption for these basalts (1.94±0.85 Ma, 505-57 and 22.4±1.0 Ma, 505-66). We also feel the larger error is more representative of the precision to which we know these eruption ages. We note that the radiogenic yields revealed by these samples are lower than expected. Values well over 50% radiogenic would be expected for unaltered basalts of this age. This implies these basalts may contain hydrated groundmass glass or some other alteration product.

References Cited

Deino, A., and Potts, R., 1992. Age-probability spectra from examination of singlecrystal $^{40}Ar/^{39}Ar$ dating results: Examples from Olorgesailie, Southern Kenya Rift, Quat. International, 13/14, 47-53.

Harrison, T.M., and McDougall, I. 1981. Excess ^{40}Ar in metamorphic rocks from Broken Hill, New South Wales: Implications for $^{40}Ar/^{39}Ar$ age spectra and the thermal history of the region. Earth Planet. Sci. Lett., 55, 123-149.

Renne, P.R., Owens, T.L., DePaolo, D.J., Swisher, C.C., Deino, A.L., and Darner, D.B., 1998. Intercalibration of standards, absolute ages and uncertainties in $^{40}Ar.39AR$ dating, 145, 117-152.

Samson, S.D., and, Alexander, E.C., Jr., 1987. Calibration of the interlaboratory $^{40}Ar/^{39}Ar$ dating standard, Mmhb-1, Chem. Geol., 66, 27-34.

Steiger, R.H., and Jäger, E., 1977. Subcommission on geochronology: Convention on the use of decay constants in geo- and cosmochronology. Earth and Planet. Sci. Lett., 36, 359-362.

Table 3. $^{40}Ar/^{39}Ar$ analytical data.

	ID	Temp (°C)	$^{40}Ar/^{39}Ar$	$^{37}Ar/^{39}Ar$	$^{36}Ar/^{39}Ar$ (x 10^{-3})	$^{39}Ar_K$ x 10^{-15} mol)	K/Ca	$^{40}Ar^*$ (%)	^{39}Ar (%)	Age (Ma)	±1σ (Ma)
	505-66, Groundmass Concentrate, 89.91 mg, J=0.0001126±0.16%, D=1.004±0.001, NM-190B, Lab#=55698-01										
X	A	800	6947.7	2.587	22803.0	3.0	0.20	3.0	10.4	42.19	5.57
X	BB	940	188.7	1.151	252.3	8.3	0.44	60.6	38.8	23.11	0.10
	C	1000	139.1	0.7049	94.11	7.4	0.72	80.1	64.1	22.51	0.06
	D	1120	193.2	0.7862	280.4	7.0	0.65	57.2	88.0	22.31	0.10
X	E	1150	262.5	1.050	503.7	1.3	0.49	43.4	92.4	23.00	0.20
X	F	1180	310.8	1.525	694.7	0.4	0.33	34.1	93.8	21.39	0.37
X	G	1190	314.4	2.540	704.3	0.3	0.20	34.0	94.7	21.58	0.50
X	H	1220	350.3	6.166	823.7	0.4	0.083	30.9	96.0	21.87	0.43
X	I	1300	487.4	20.18	1255.8	0.8	0.025	24.7	98.9	24.44	0.43
X	J	1650	557.6	17.39	1491.3	0.3	0.029	21.6	100.0	24.42	0.62
	Integrated age ± 2σ			n=10		29.1	0.27		K2O=1.10%	24.74	1.33
	Plateau ± 2σ	steps C-D		n=2	MSWD=2.73	14.3	0.69 ±0.11		49.2	22.46	0.18
	Isochron±2σ	steps A-J		n=10	MSWD=8.65		$^{40}Ar/^{36}Ar$=	299±12		22.4	1.0
	505-57, Groundmass Concentrate, 98.98 mg, J=0.0001127±0.16%, D=1.004±0.001, NM-190B, Lab#=55699-01										
Xi	B	700	1481.9	0.8264	4907.7	6.7	0.62	2.1	22.4	6.46	1.21
	C	750	150.1	0.7247	464.2	3.7	0.70	8.7	34.9	2.65	0.13
	D	800	160.6	0.6163	497.3	2.3	0.83	8.6	42.7	2.80	0.15
	E	875	152.0	0.6752	472.8	3.0	0.76	8.2	52.9	2.52	0.14
	F	975	124.7	0.9118	382.7	3.2	0.56	9.4	63.6	2.39	0.11
	G	1075	108.4	1.060	331.1	3.5	0.48	10.0	75.5	2.20	0.10
	H	1250	251.0	7.151	810.8	6.7	0.071	5.1	98.0	2.61	0.21
Xi	I	1700	932.2	13.04	3023.3	0.6	0.039	4.4	100.0	8.43	0.87
	Integrated age ± 2σ			n=8		29.7	0.21		K2O=1.02%	3.53	0.77
	Plateau ± 2σ	steps C-H		n=6	MSWD=2.94	22.5	0.48 ±0.55		75.6	2.46	0.18
	Isochron±2σ	steps C-H		n=6	MSWD=1.96		$^{40}Ar/^{36}Ar$=	301.4±8.5		1.94	0.85

Notes:
Isotopic ratios corrected for blank, radioactive decay, and mass discrimination, not corrected for interfering reactions.
Errors quoted for individual analyses include analytical error only, without interfering reaction or J uncertainties.
Integrated age calculated by summing isotopic measurements of all steps.
Integrated age error calculated by quadratically combining errors of isotopic measurements of all steps.
Plateau age is inverse-variance-weighted mean of selected steps.
Plateau age error is inverse-variance-weighted mean error (Taylor, 1982) times root MSWD where MSWD>1.
Decay constants and isotopic abundances after Steiger and Jäger (1977).
X symbol preceeding sample ID denotes analyses excluded from plateau age calculations.
i symbol preceeding sample ID denotes samples excluded from isochron age calculations.
Weight percent K_2O calculated from ^{39}Ar signal, sample weight, and instrument sensitivity.
Ages calculated relative to FC-2 Fish Canyon Tuff sanidine interlaboratory standard at 28.02 Ma
Decay Constant (LambdaK (total)) = 5.543e-10/a
Correction factors:
$(^{39}Ar/^{37}Ar)_{Ca}$ = 0.000289 ± 5e-06
$(^{36}Ar/^{37}Ar)_{Ca}$ = 0.00068 ± 2e-05
$(^{38}Ar/^{39}Ar)_K$ = 0.013
$(^{40}Ar/^{39}Ar)_K$ = 0 ± 0.0004

Taylor, J.R., 1982. An Introduction to Error Analysis: The Study of Uncertainties in Physical Measurements,. Univ. Sci. Books, Mill Valley, Calif., 270 p.

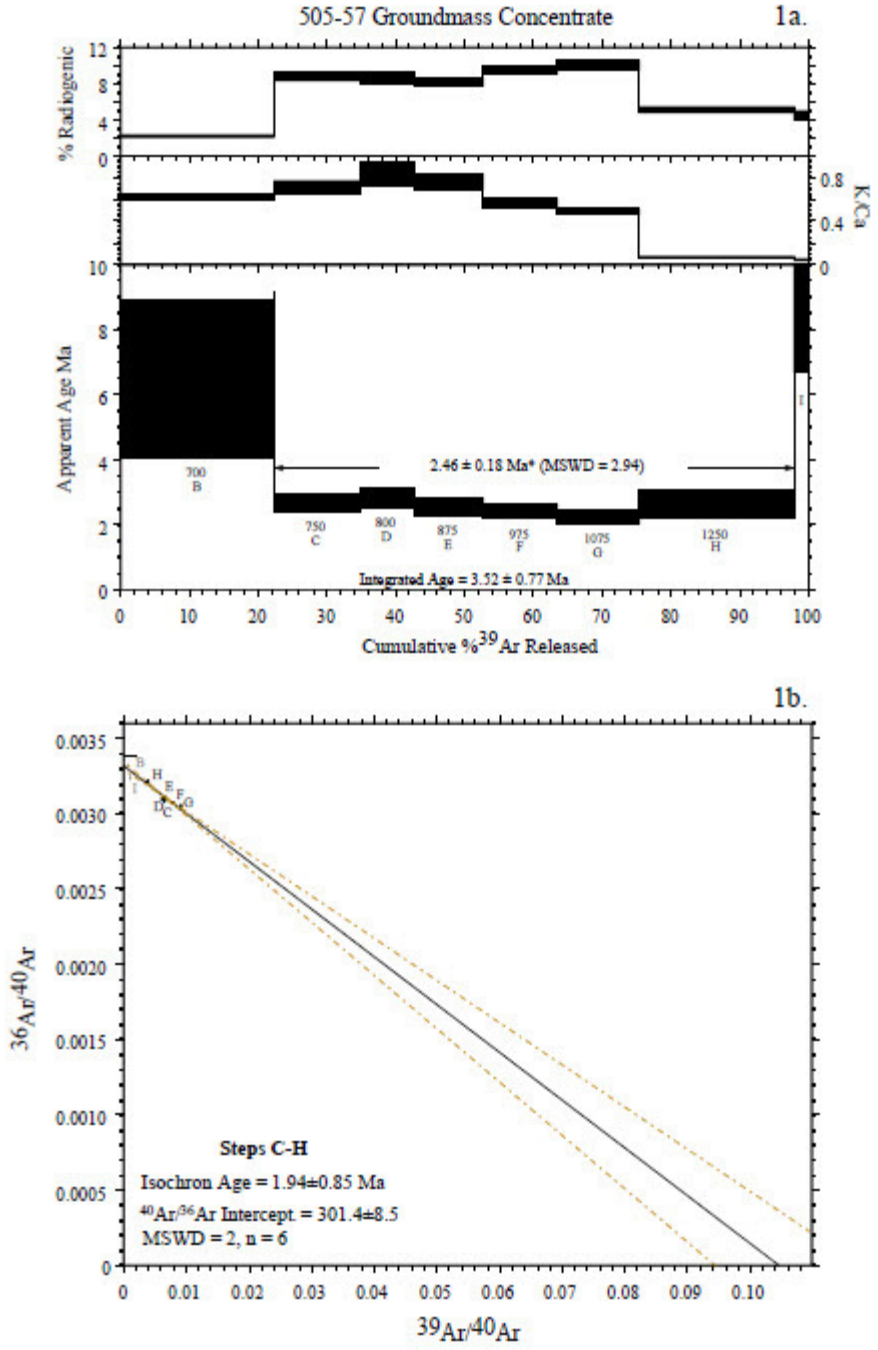


Figure 1. Age spectrum (1a) and isochron (1b) for 505-57 groundmass concentrate. All errors quoted at two sigma.

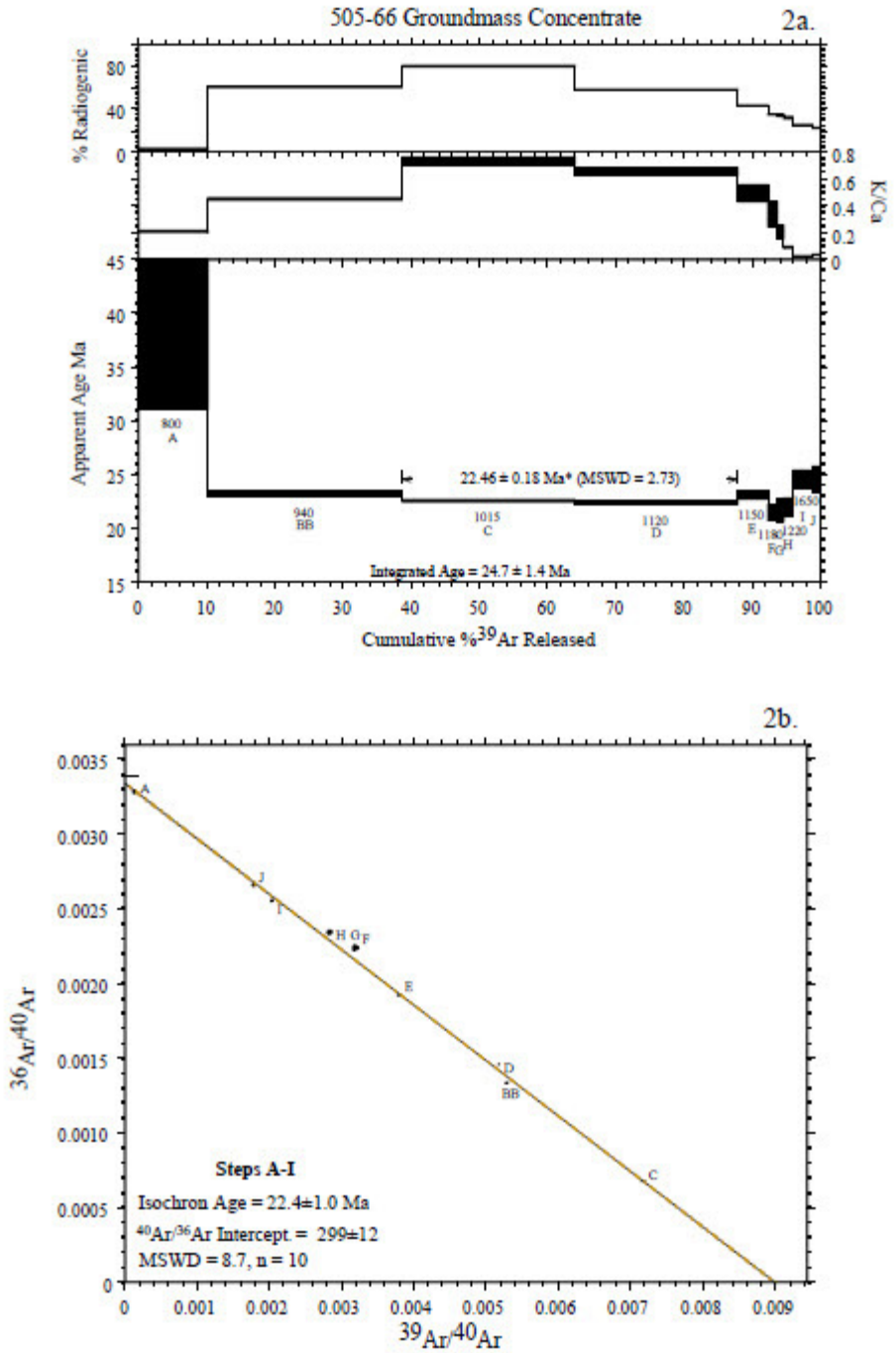


Figure 2. Age spectrum (2a) and isochron (2b) for 505-57 groundmass concentrate. All errors quoted at two sigma.

New Mexico Bureau of Mines and Mineral Resources
Procedures of the New Mexico Geochronology Research Laboratory
For the Period June 1998 – present
Matthew Heizler
William C. McIntosh
Richard Esser
Lisa Peters
2

$^{40}Ar/^{39}Ar$ and K-Ar dating

Often, large bulk samples (either minerals or whole rocks) are required for K-Ar dating and even small amounts of xenocrystic, authigenic, or other non-ideal behavior can lead to inaccuracy. The K-Ar technique is susceptible to sample inhomogeneity as separate aliquots are required for the potassium and argon determinations. The need to determine absolute quantities (i.e. moles of $^{40}Ar^*$ and ^{40}K) limits the precision of the K-Ar method to approximately 1% and also, the technique provides limited potential to evaluate underlying assumptions. In the $^{40}Ar/^{39}Ar$ variant of the K-Ar technique, a sample is irradiated with fast neutrons thereby converting ^{39}K to ^{39}Ar through a (n,p) reaction. Following irradiation, the sample is either fused or incrementally heated and the gas analyzed in the same manner as in the conventional K-Ar procedure, with one exception, no argon spike need be added.

Some of the advantages of the $^{40}Ar/^{39}Ar$ method over the conventional K-Ar technique are:1. A single analysis is conducted on one aliquot of sample thereby reducing the sample sizeand eliminating sample inhomogeneity.
2. Analytical error incurred in determining absolute abundances is reduced by measuring only isotopic ratios. This also eliminates the need to know the exact weight of the sample.
3. The addition of an argon spike is not necessary.
4. The sample does not need to be completely fused, but rather can be incrementally heated.

The $^{40}Ar/^{39}Ar$ ratio (age) can be measured for each fraction of argon released and this allows for the generation of an age spectrum. The age of a sample as determined with the $^{40}Ar/^{39}Ar$ method requires comparison of the measured $^{40}Ar/^{39}Ar$ ratio with that of a standard of known age. Also, several isotopes of other elements (Ca, K, Cl, Ar) produce argon during the irradiation procedure and must be corrected for. Far more in-depth details of the determination of an apparent age via the $^{40}Ar/^{39}Ar$ method
are given in Dalrymple et al. (1981) and McDougall and Harrison (1988).

Analytical techniques

Sample Preparation and irradiation details

Mineral separates are obtained in various fashions depending upon the mineral of interest, rock type and grain size. In almost all cases the sample is crushed in a jaw crusher and ground in a disc grinder and then sized. The size fraction used generally

corresponds to the largest size possible which will permit obtaining a pure mineral separate. Following sizing, the sample is washed and dried. For plutonic and metamorphic rocks and lavas, crystals are separated using standard heavy liquid, Franz magnetic and hand-picking techniques. For volcanic sanidine and plagioclase, the sized sample is reacted with 15% HF acid to remove glass and/or matrix and then thoroughly washed prior to heavy liquid and magnetic separation. For groundmass concentrates, rock fragments are selected which do not contain any visible phenocrysts.

The NMGRL uses either the Ford reactor at the University of Michigan or the Nuclear Science Center reactor at Texas A&M University. At the Ford reactor, the L67 position is used (unless otherwise noted) and the D-3 position is always used at the Texas A&M reactor. All of the Michigan irradiations are carried out underwater without any shielding for thermal neutrons, whereas the Texas irradiations are in a dry location which is shielded with B and Cd. Depending upon the reactor used, the mineral separates are loaded into either holes drilled into Al discs or into 6 mm I.D. quartz tubes. Various Al discs are used. For Michigan, either six hole or twelve hole, 1 cm diameter discs are used and all holes are of equal size. Samples are placed in the 0, 120 and 240° locations and standards in the 60, 180 and 300° locations for the six hole disc. For the twelve hole disc, samples are located at 30, 60, 120, 150, 210, 240, 300, and 330° and standards at 0, 90, 180 and 270 degrees. If samples are loaded into the quartz tubes, they are wrapped in Cu foil with standards interleaved at ~0.5 cm intervals. For Texas, 2.4 cm diameter discs contain either sixteen or six sample holes with smaller holes used to hold the standards. For the six hole disc, sample locations are 30, 90, 150, 210, 270 and 330° and standards are at 0, 60, 120, 180, 240 and 300°. Samples are located at 18, 36, 54, 72, 108, 126, 144, 162, 198, 216, 234, 252, 288, 306, 324, 342 degrees and standards at 0, 90, 180 and 270 degrees in the sixteen hole disc. Following sample loading into the discs, the discs are stacked, screwed together and sealedin vacuo in either quartz (Michigan) or Pyrex (Texas) tubes.

Extraction Line and Mass Spectrometer details

The NMGRL argon extraction line has both a double vacuum Mo resistance furnace and a CO_2 laser to heat samples. The Mo furnace crucible is heated with a W heating element and the temperature is monitored with a W-Re thermocouple placed in a hole drilled into the bottom of the crucible. A one inch long Mo liner is placed in the bottom of the crucible to collect the melted samples. The furnace temperature is calibrated by either/or melting Cu foil or with an additional thermocouple inserted in the top of the furnace down to the liner. The CO_2 laser is a Synrad 10W laser equipped with a He-Ne pointing laser. The laser chamber is constructed from a 3 3/8" stainless steel conflat and the window material is ZnS. The extraction line is a two stage design. The first stage is equipped with a SAES GP-50 getter, whereas the second stage houses two SAES GP-50 getters and a tungsten filament. The first stage getter is operated at 450°C as is one of the second stage getters. The other second stage getter is operated at room temperature
and the tungsten filament is operated at ~2000°C. Gases evolved from samples heated in the furnace are reacted with the first stage getter during heating. Following heating, the

gas is expanded into the second stage for two minutes and then isolated from the first stage. During second stage cleaning, the first stage and furnace are pumped out. After gettering in the second stage, the gas is expanded into the mass spectrometer. Gases evolved from samples heated in the laser are expanded through a cold finger operated at -140°C and directly into the second stage. Following cleanup, the gas in the second stage and laser chamber is expanded into the mass spectrometer for analysis.

The NMGRL employs a MAP-215-50 mass spectrometer which is operated in static mode. The mass spectrometer is operated with a resolution ranging between 450 to 600 at mass40 and isotopes are detected on a Johnston electron multiplier operated at ~2.1 kV with an overall gain of about 10,000 over the Faraday collector. Final isotopic intensities are determined by linear regression to time zero of the peak height versus time following gas introduction for each mass. Each mass intensity is corrected for mass spectrometer baseline and background and the extraction system blank.

Blanks for the furnace are generally determined at the beginning of a run while the furnace is cold and then between heating steps while the furnace is cooling. Typically, a blank is run every three to six heating steps. Periodic furnace hot blank analysis reveals that the cold blank is equivalent to the hot blank for temperatures less than about 1300°C. Laser system blanks are generally determined between every four analyses. Mass discrimination is measured using atmospheric argon which has been dried using a Ti-sublimation pump. Typically, 10 to 15 replicate air analyses are measured to determine a mean mass discrimination value. Air pipette analyses are generally conducted 2-3 times per month, but more often when samples sensitive to the mass discrimination value are analyzed. Correction factors for interfering nuclear reactions on K and Ca are determined using K-glass and CaF_2, respectively. Typically, 3-5 individual pieces of the salt or glass are fused with the CO_2 laser and the correction factors are calculated from the weighted mean of the individual determinations.

Data acquisition, presentation and age calculation

Samples are either step-heated or fused in a single increment (total fusion). Bulk samples are often step-heated and the data are generally displayed on an age spectrum or isochron diagram. Single crystals are often analyzed by the total fusion method and the results are typically displayed on probability distribution diagrams or isochron diagrams.
The Age Spectrum Diagram Age spectra plot apparent age of each incrementally heated gas fraction versus the cumulative % $^{39}Ar_K$ released, with steps increasing in temperature from left to right. Each apparent age is calculated assuming that the trapped argon (argon not produced by *in situ* decay of ^{40}K) has the modern day atmospheric $^{40}Ar/^{36}Ar$ value of 295.5. Additional parameters for each heating step are often plotted versus the cumulative $\%^{39}Ar_K$ released. These auxiliary parameters can aid age spectra interpretation and may include radiogenic yield (percent of ^{40}Ar which is not atmospheric), K/Ca (determined from measured Ca-derived ^{37}Ar and K-derived ^{39}Ar) and/or K/Cl (determined from measured Cl-derived ^{38}Ar and K-derived ^{39}Ar). Incremental heating analysis is often effective at revealing complex argon systematics related to excess argon, alteration, contamination, ^{39}Ar recoil, argon loss, etc. Often low-temperature heating steps have low

radiogenic yields and apparent ages with relatively high errors due mainly to 6 loosely held, non-radiogenic argon residing on grain surfaces or along grain boundaries. An entirely or partially flat spectrum, in which apparent ages are the same within analytical error, may indicate that the sample is homogeneous with respect to K and Ar and has had a simple thermal and geological history. A drawback to the age spectrum technique is encountered when hydrous minerals such as micas and amphiboles are analyzed. These minerals are not stable in the ultra-high vacuum extraction system and thus step-heating can homogenize important details of the true ^{40}Ar distribution. In other words, a flat age spectrum may result even if a hydrous sample has a complex argon distribution.

The Isochron Diagram

Argon data can be plotted on isotope correlation diagrams to help assess the isotopic composition of Ar trapped at the time of argon closure, thereby testing the assumption that trapped argon isotopes have the composition of modern atmosphere which is implicit in age spectra. To construct an "inverse isochron" the $^{36}Ar/^{40}Ar$ ratio is plotted versus the $^{39}Ar/^{40}Ar$ ratio. A best fit line can be calculated for the data array which yields the value for the trapped argon (Y-axis intercept) and the $^{40}Ar^*/^{39}Ar_K$ value (age) from the X-axis intercept. Isochron analysis is most useful for step-heated or total fusion data which have a significant spread in radiogenic yield. For young or low K samples, the calculated apparent age can be very sensitive to the composition of the trapped argon and therefore isochron analysis should be preformed routinely on these samples (cf. Heizler and Harrison, 1988). For very old (>Mesozoic) samples or relatively old sanidines (>mid-Cenozoic) the data are often highly radiogenic and cluster near the X-axis thereby making isochron analysis of little value.

The Probability Distribution Diagram

The probability distribution diagram, which is sometimes referred to as an ideogram, is a plot of apparent age versus the summation of the normal distribution of each individual analysis (Deino and Potts, 1992). This diagram is most effective at displaying single crystal laser fusion data to assess the distribution of the population. The K/Ca, radiogenic yield, and the moles of ^{39}Ar for each analysis are also often displayed for each sample as this allows for visual ease in identifying apparent age correlations between, for instance, plagioclase contamination, signal size and/or radiogenic concentrations. The error (1σ) for each age analysis is generally shown by the horizontal lines in the moles of ^{39}Ar section. Solid symbols represent the analyses used for the weighted mean age calculation and the generation of the solid line on the ideogram, whereas open symbols represent data omitted from the age calculation. If shown, a dashed line represents the probability distribution of all of the displayed data. The diagram is most effective for displaying the form of the age distribution (i.e. gaussian, skewed, etc.) and for identifying xenocrystic or other grains which fall outside of the main population.

Error Calculations

For step-heated samples, a plateau for the age spectrum is defined by the steps indicated. The plateau age is calculated by weighting each step on the plateau by the inverse of the variance and the error is calculated by either the method of Samson and Alexander (1987)

or Taylor (1982). A mean sum weighted deviates (MSWD) value is determined by dividing the Chisquared value by n-1 degrees of freedom for the plateau ages. If the MSWD value is outside the 95% confidence window (cf. Mahon, 1996; Table 1), the plateau or preferred age error is multiplied by the square root of the MSWD.

For single crystal fusion data, a weighted mean is calculated using the inverse of the variance to weight each age determination (Taylor, 1982). Errors are calculated as described for the plateau ages above.
Isochron ages, $^{40}Ar/^{36}Ar_i$ values and MSWD values are calculated from the regression results obtained by the York (1969) method.

References cited

Dalrymple, G.B., Alexander, E.C., Jr., Lanphere, M.A., and Kraker, G.P., 1981. Irradiation of samples for $^{40}Ar/^{39}Ar$ dating using the Geological Survey TRIGA reactor. U.S.G.S., Prof. Paper, 1176.

Deino, A., and Potts, R., 1990. Single-Crystal $^{40}Ar/^{39}Ar$ dating of the Olorgesailie Formation, Southern Kenya Rift, J. Geophys. Res., 95, 8453-8470.

Deino, A., and Potts, R., 1992. Age-probability spectra from examination of single-crystal $^{40}Ar/^{39}Ar$ dating results: Examples from Olorgesailie, Southern Kenya Rift, Quat. International, 13/14, 47-53.

Fleck, R.J., Sutter, J.F., and Elliot, D.H., 1977. Interpretation of discordant $^{40}Ar/^{39}Ar$ age-spectra of Mesozoic tholieiites from Antarctica, Geochim. Cosmochim. Acta, 41, 15-32.
Heizler, M. T., and Harrison, T. M., 1988. Multiple trapped argon components revealed by $^{40}Ar/^{39}Ar$ analysis, Geochim. Cosmochim. Acta, 52, 295-1303.

Mahon, K.I., 1996. The New "York" regression: Application of an improved statistical method to geochemistry, International Geology Review, 38, 293-303.

McDougall, I., and Harrison, T.M., 1988. Geochronology and thermochronology by the ^{40}Ar- ^{39}Ar method. Oxford University Press.

Samson, S.D., and, Alexander, E.C., Jr., 1987. Calibration of the interlaboratory $^{40}Ar/^{39}Ar$ dating standard, Mmhb-1, Chem. Geol., 66, 27-34.

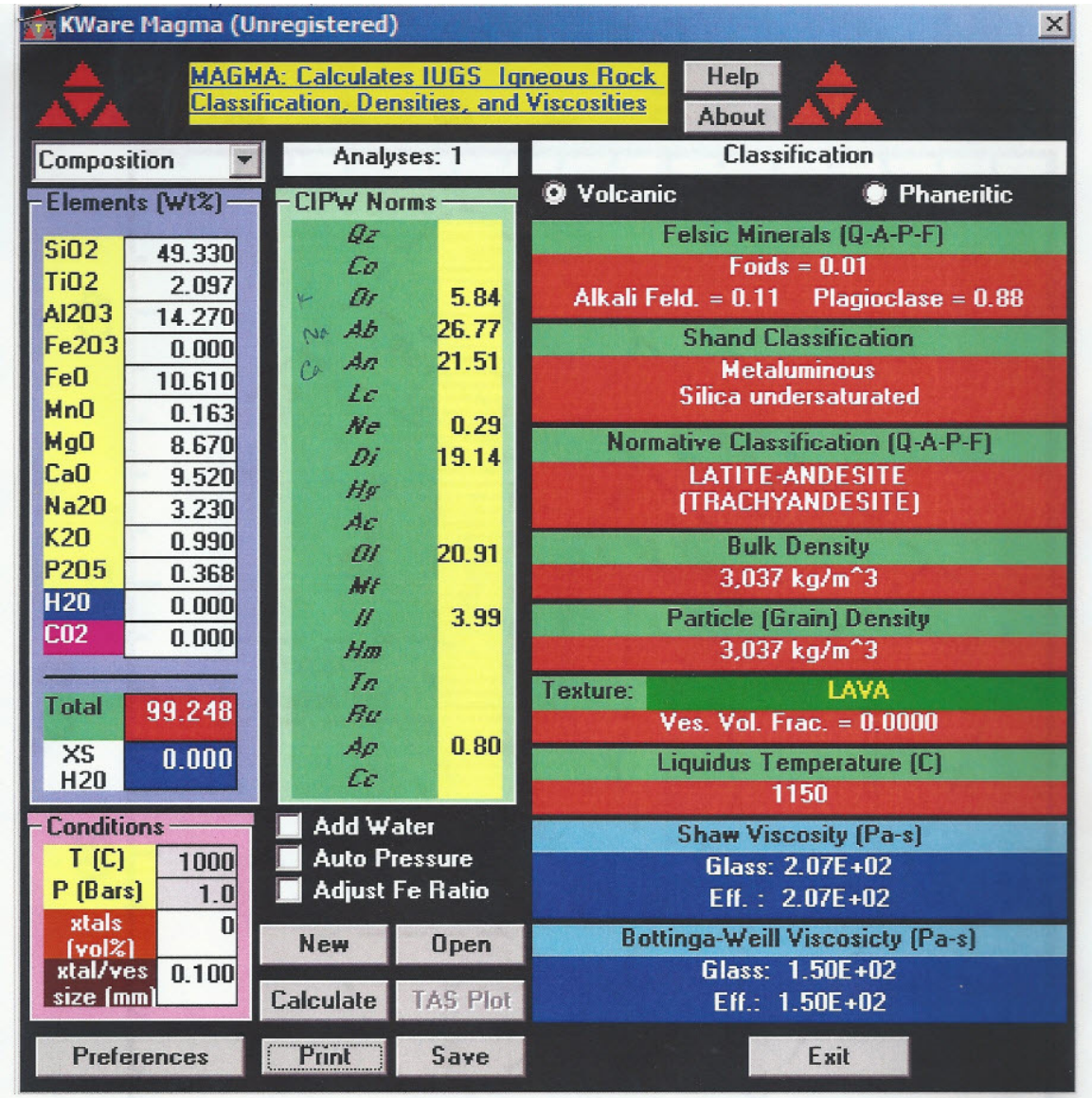
Steiger, R.H., and Jäger, E., 1977. Subcommission on geochronology: Convention on the use of decay constants in geo- and cosmochronology. Earth and Planet. Sci. Lett., 36, 359-362.
Taylor, J.R., 1982. An Introduction to Error Analysis: The Study of Uncertainties in Physical Measurements,. Univ. Sci. Books, Mill Valley, Calif., 270 p.

York, D., 1969. Least squares fitting of a straight line with correlated errors, Earth and Planet. Sci. Lett.., 5, 320-324.

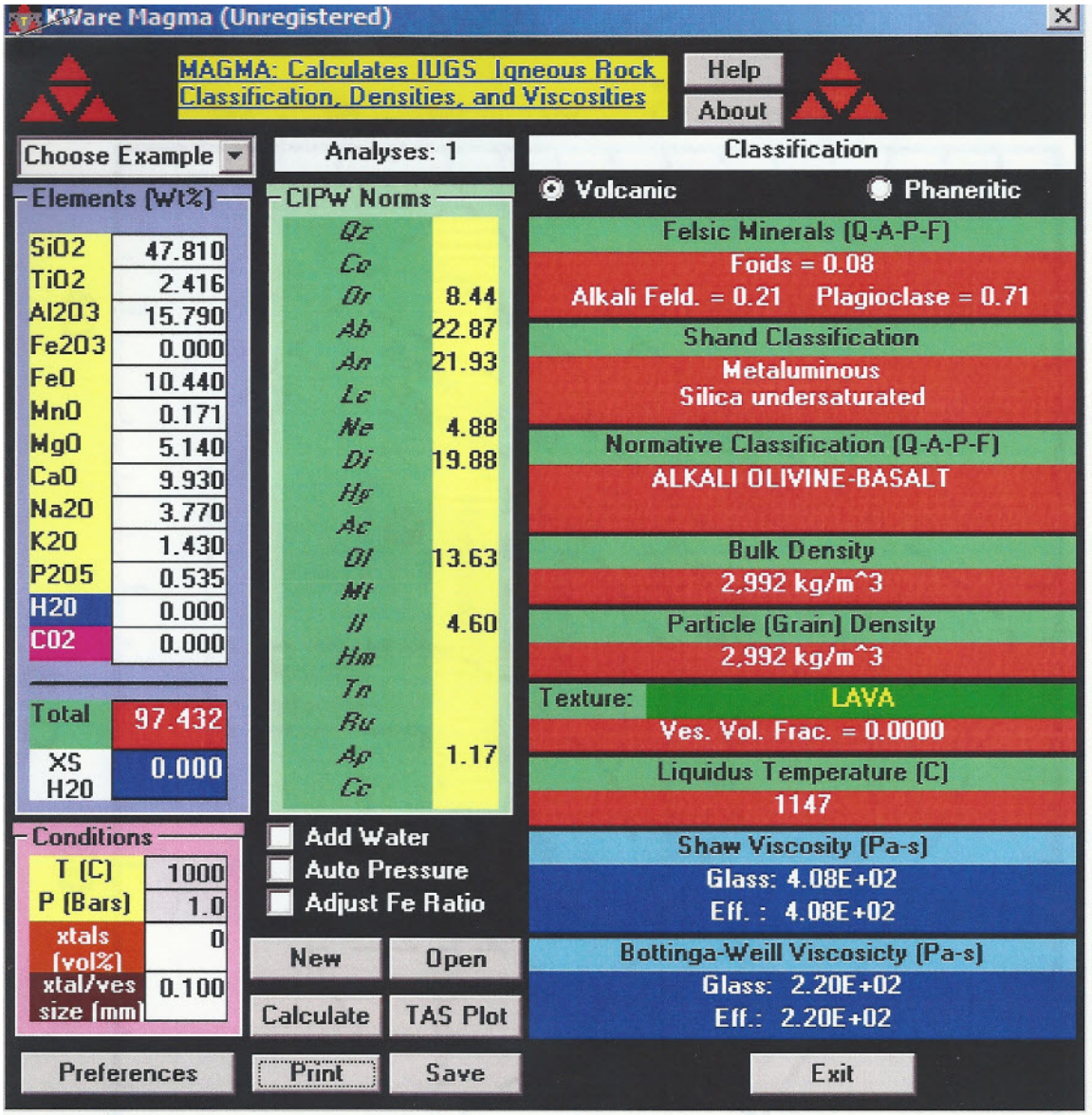
APPENDIX D

CIPW NORM AND VISCOSITY CALCULATIONS FROM XFR RESULTS

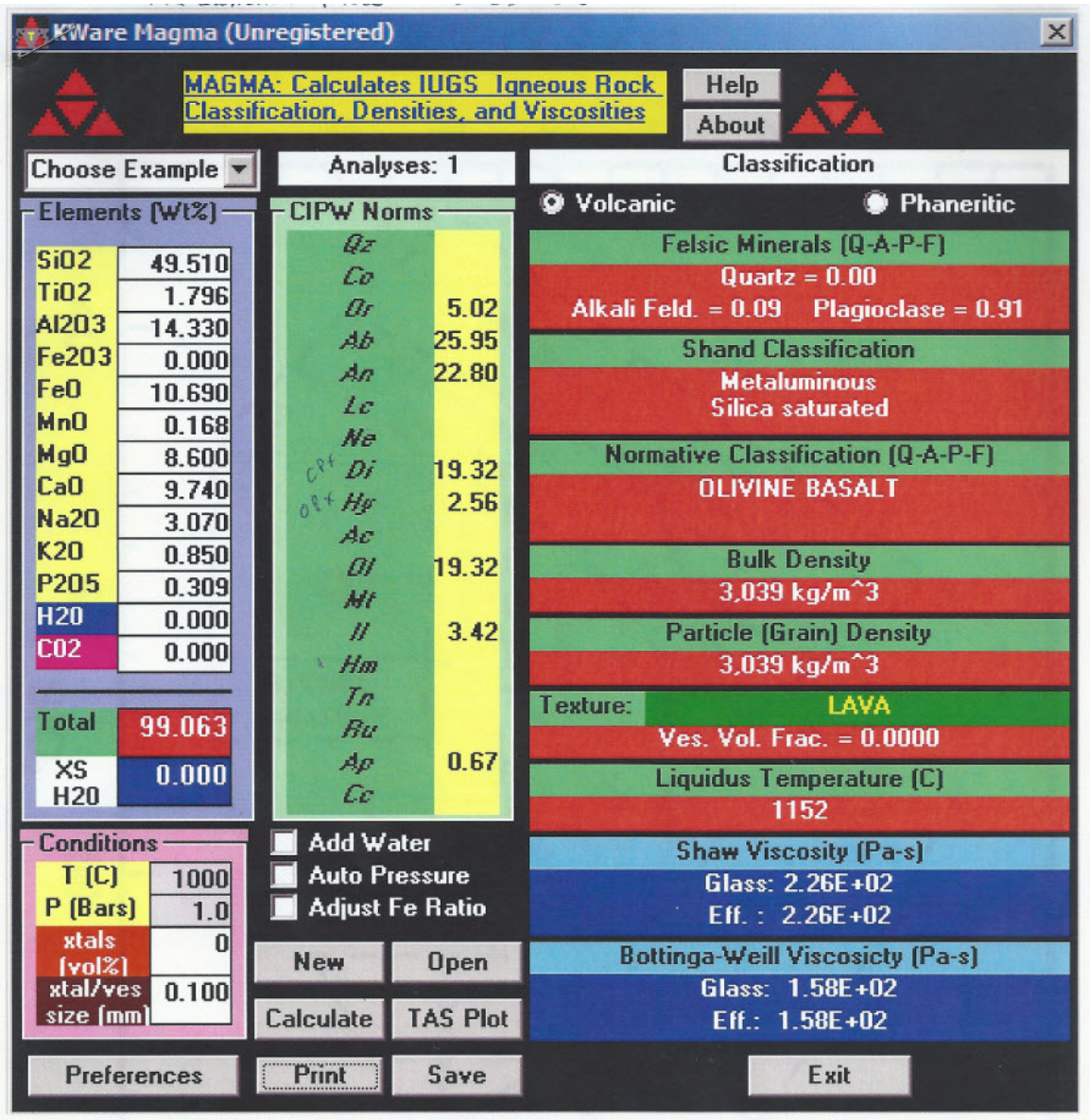
Sample number S-05-035



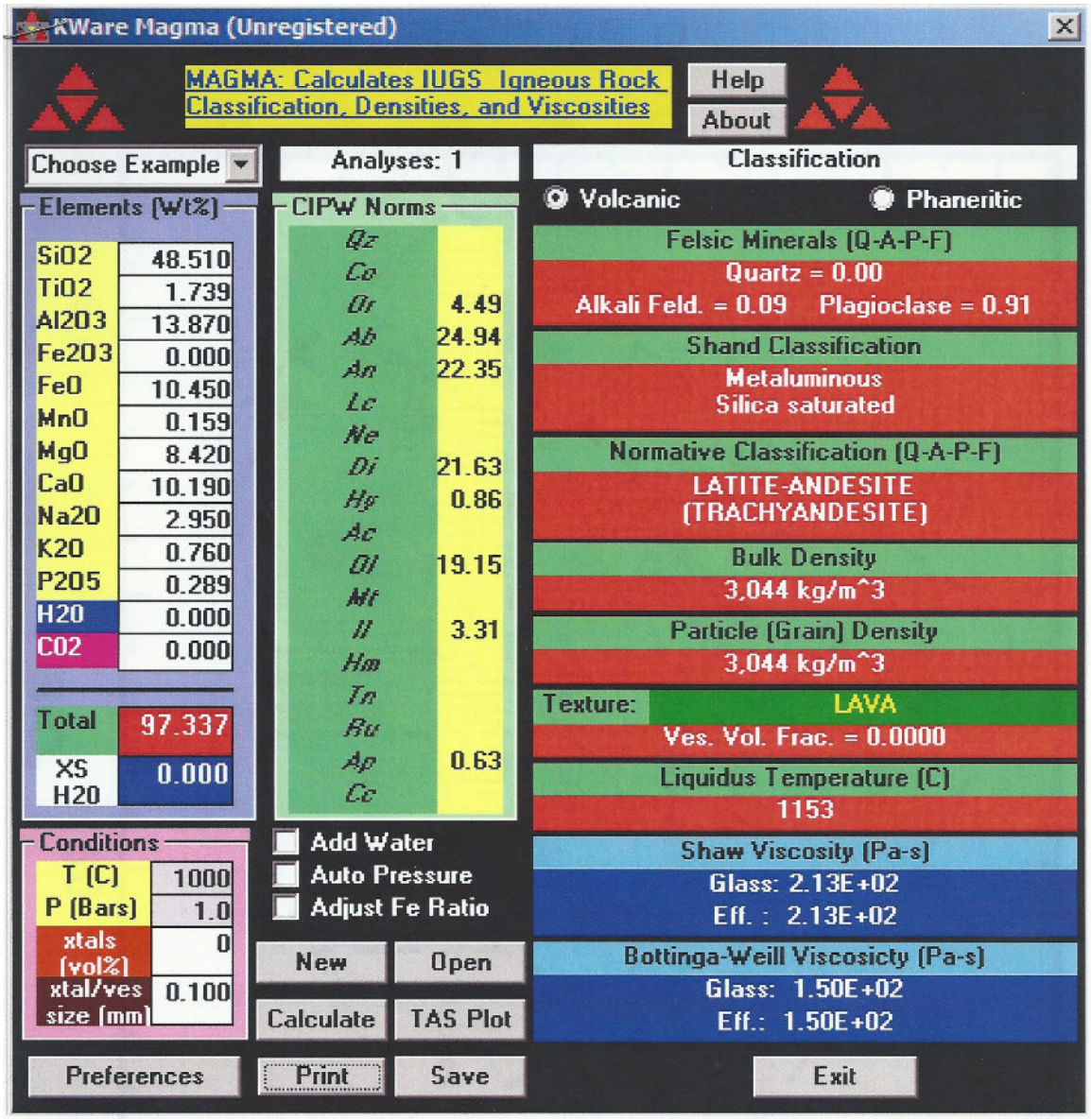
Sample number S-05-057



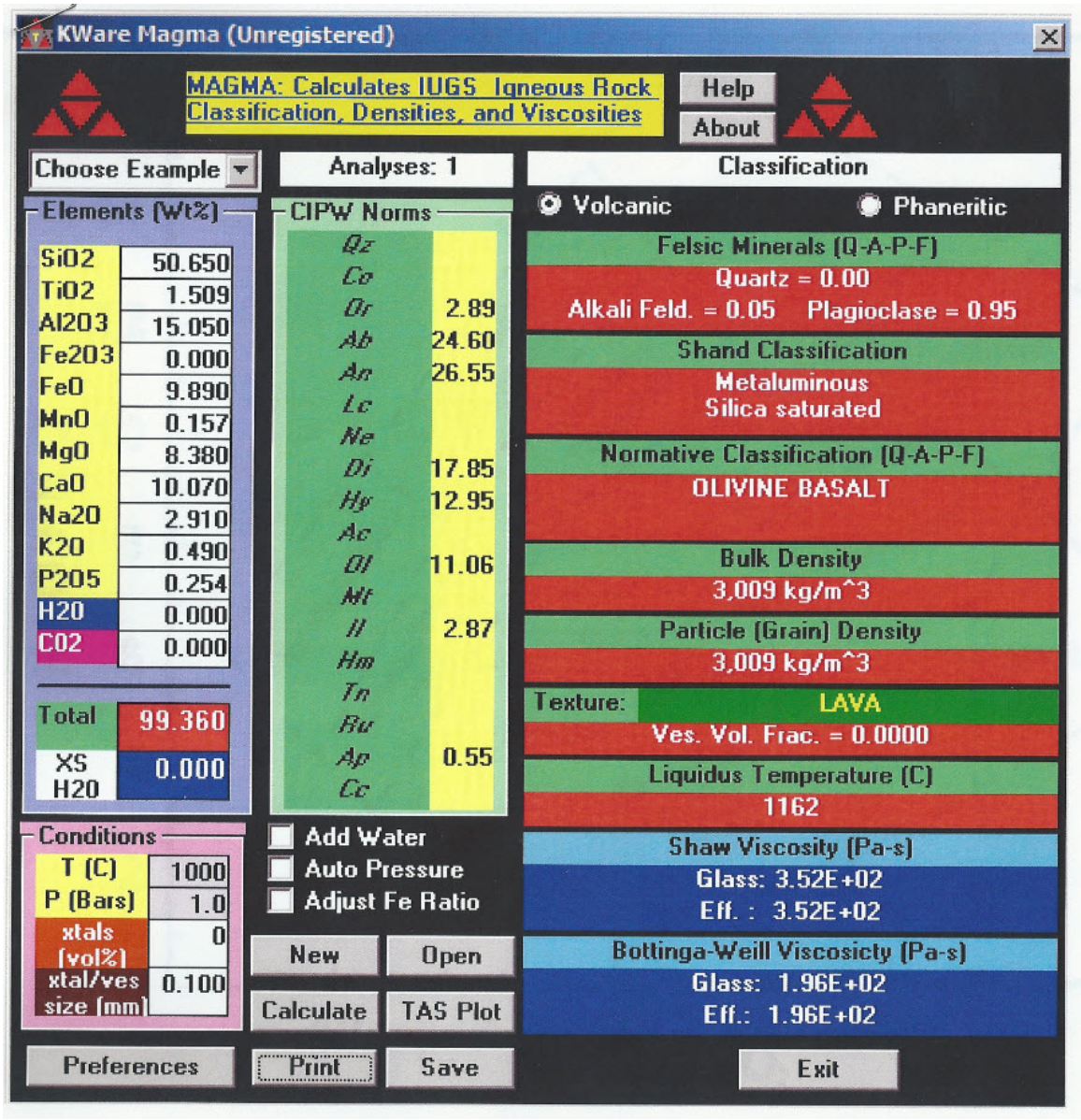
Sample number S-05-058



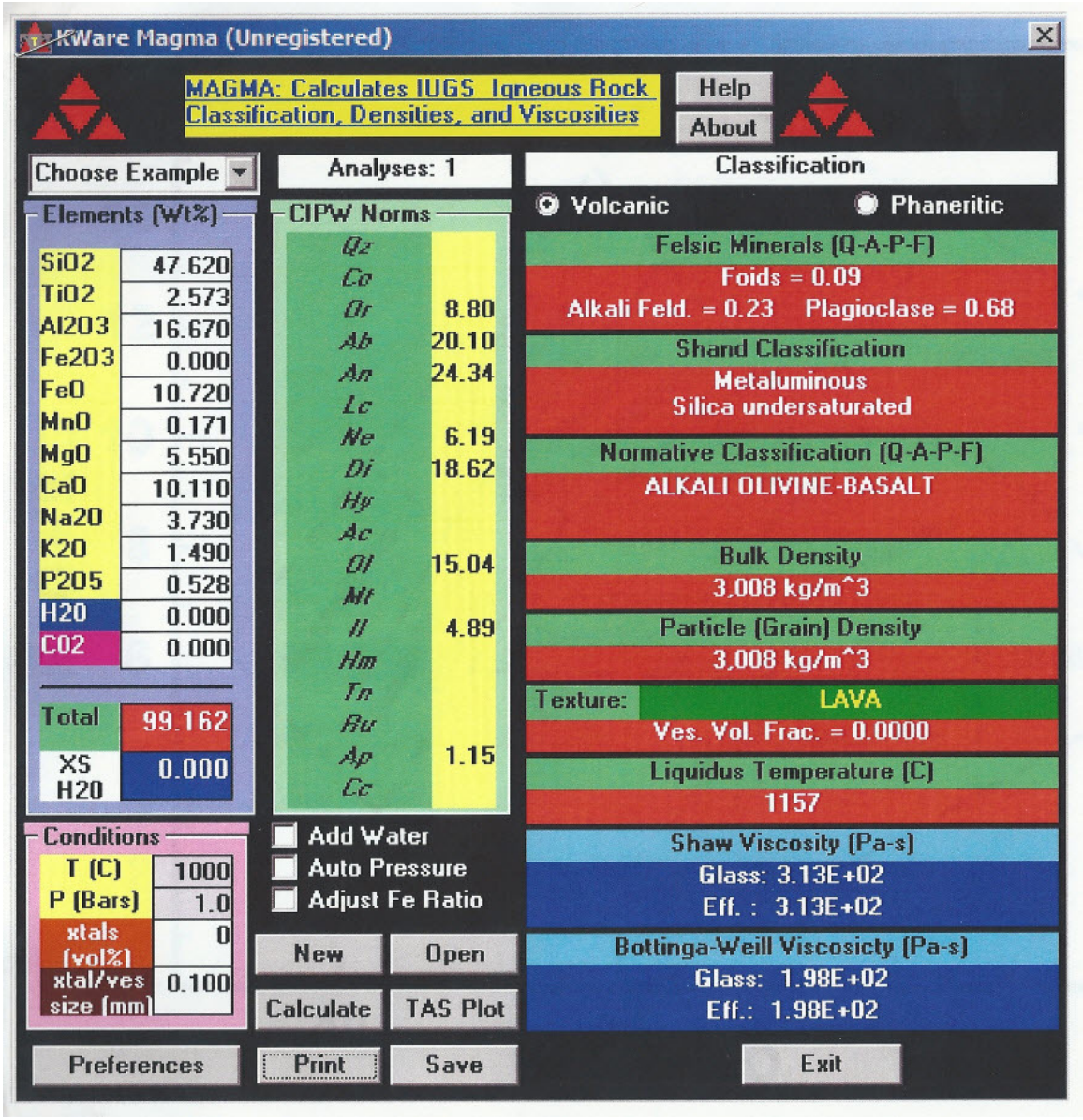
Sample number S-05-065



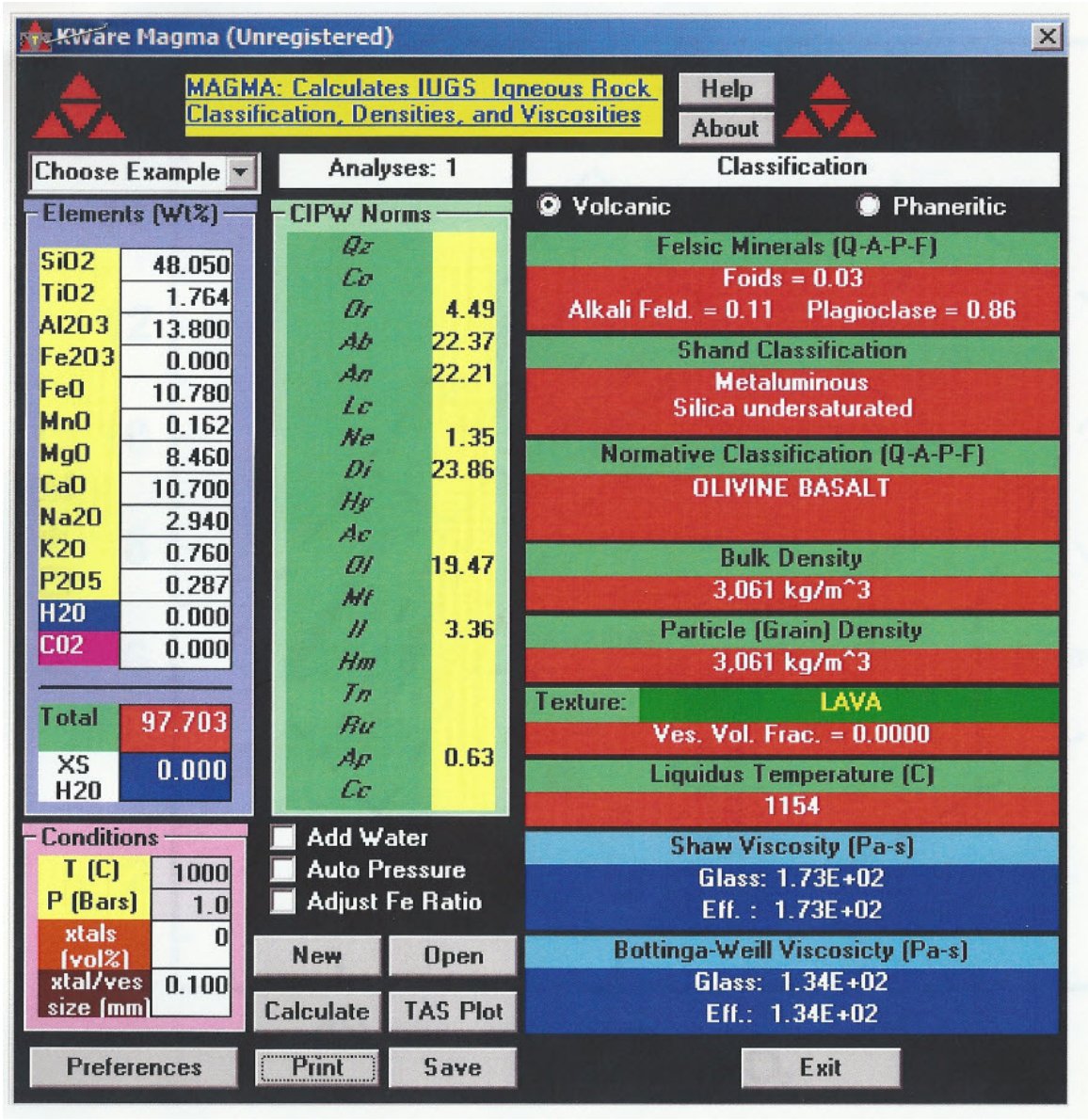
Sample number S-05-074



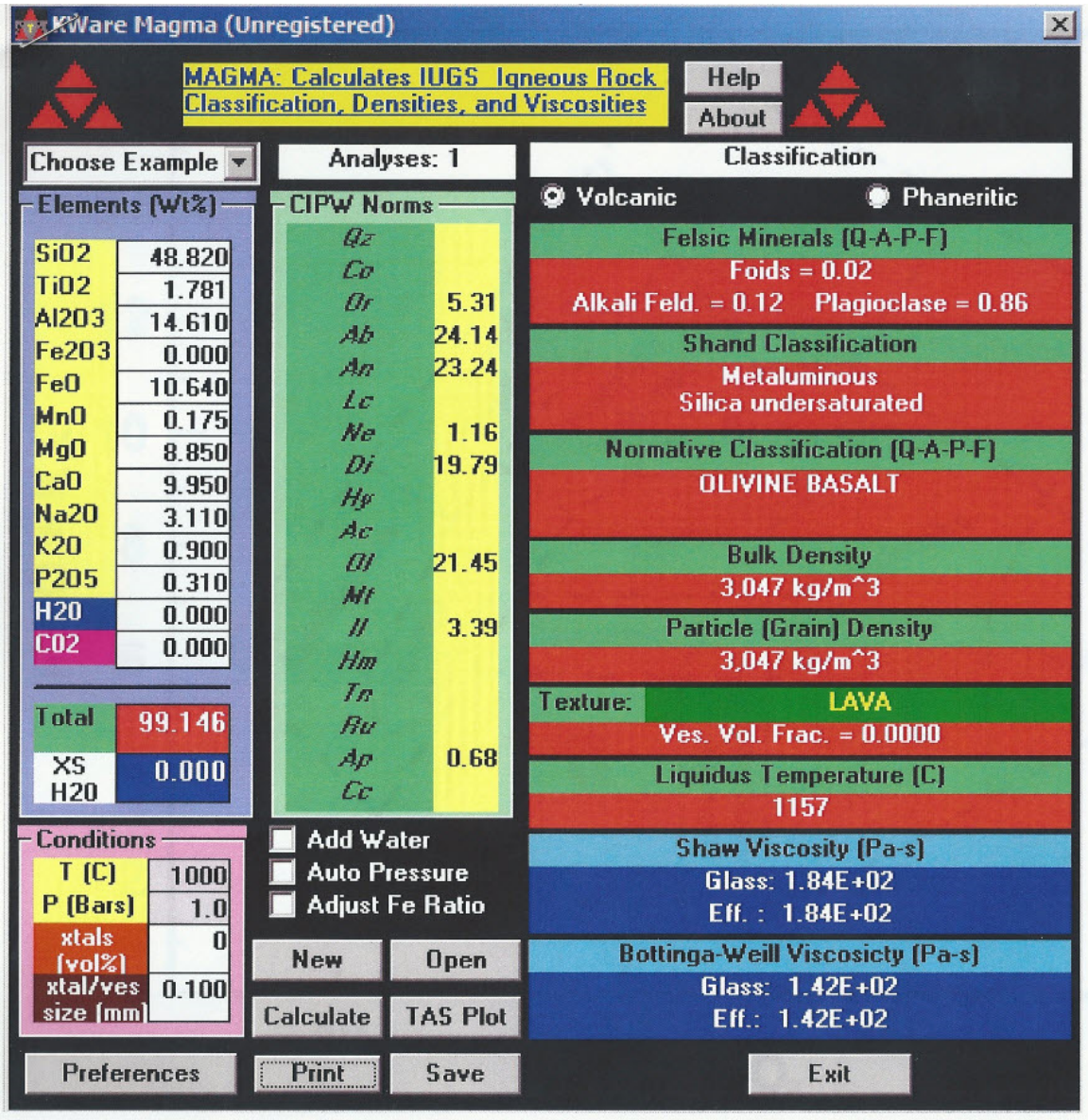
Sample number S-05-087



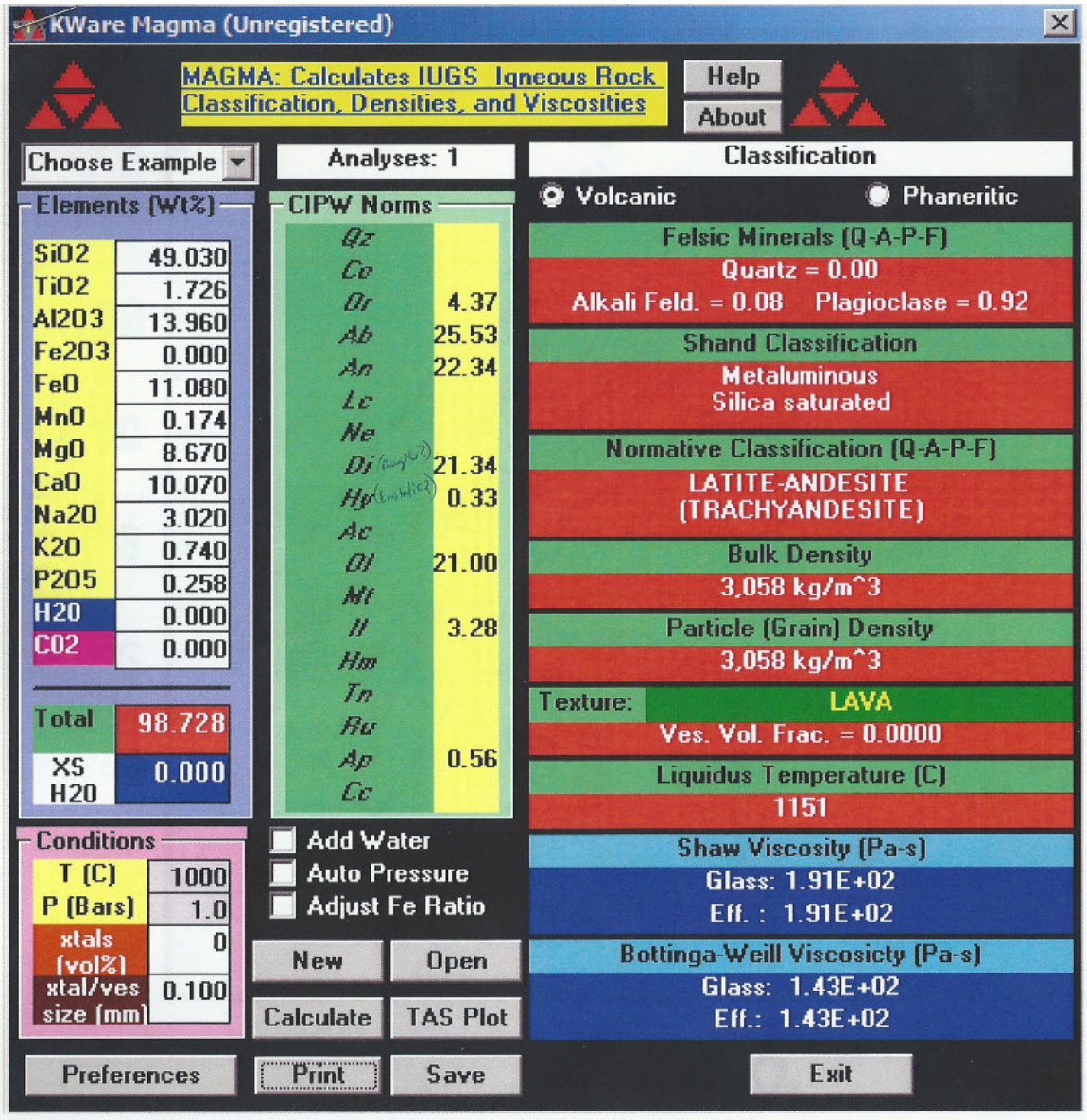
Sample number S-05-107



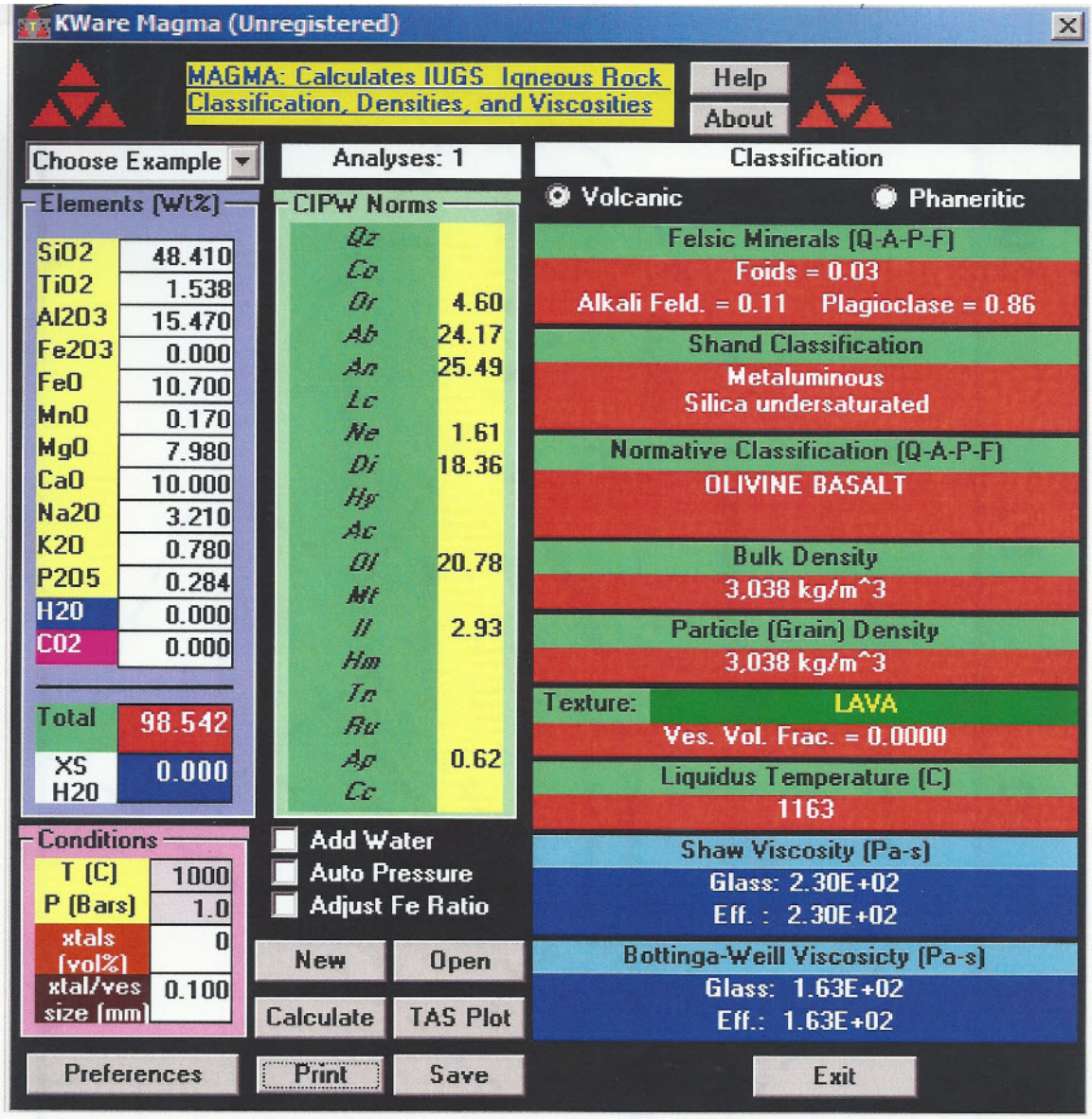
Sample number S-05-115



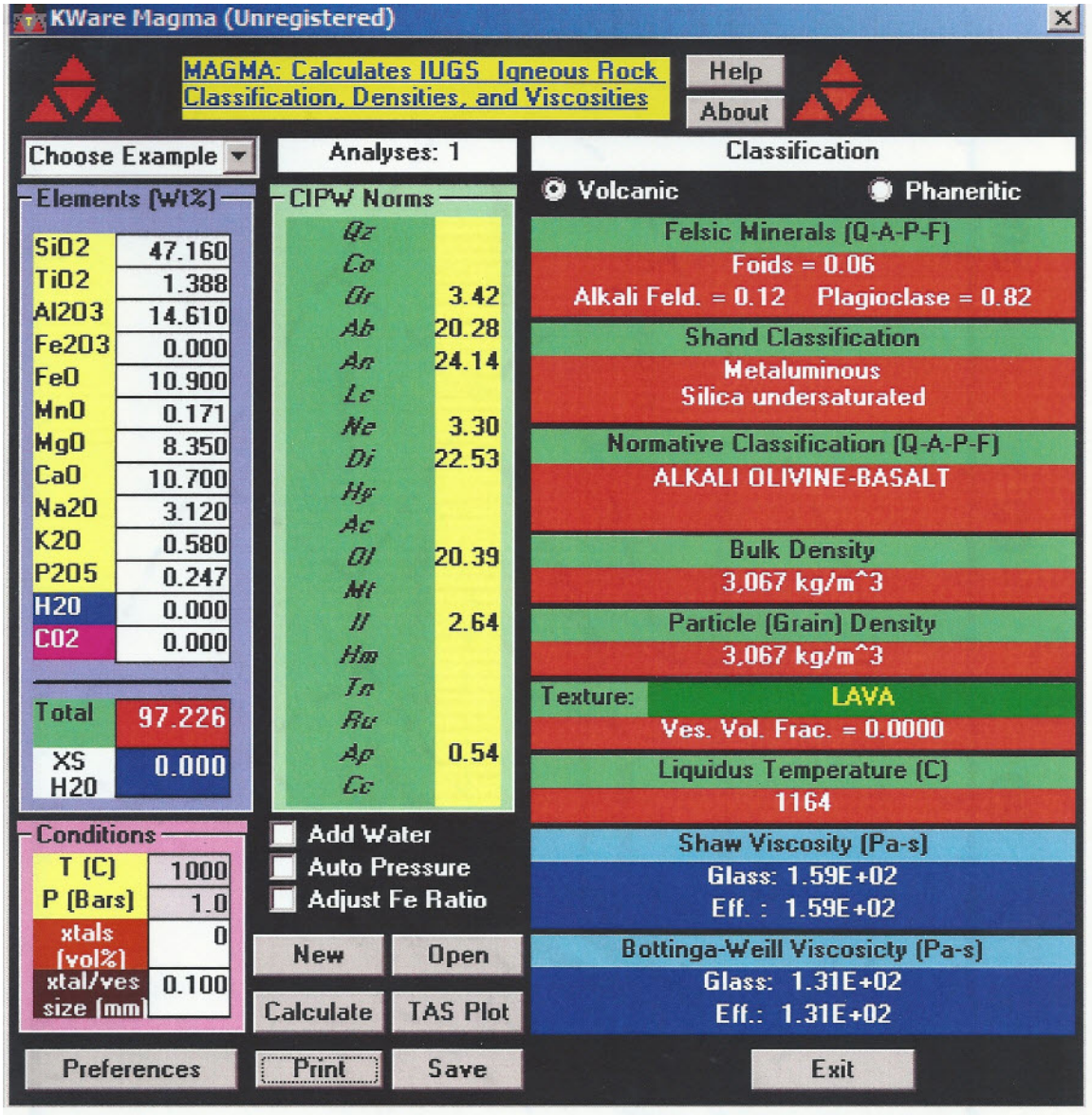
Sample number S-06-152



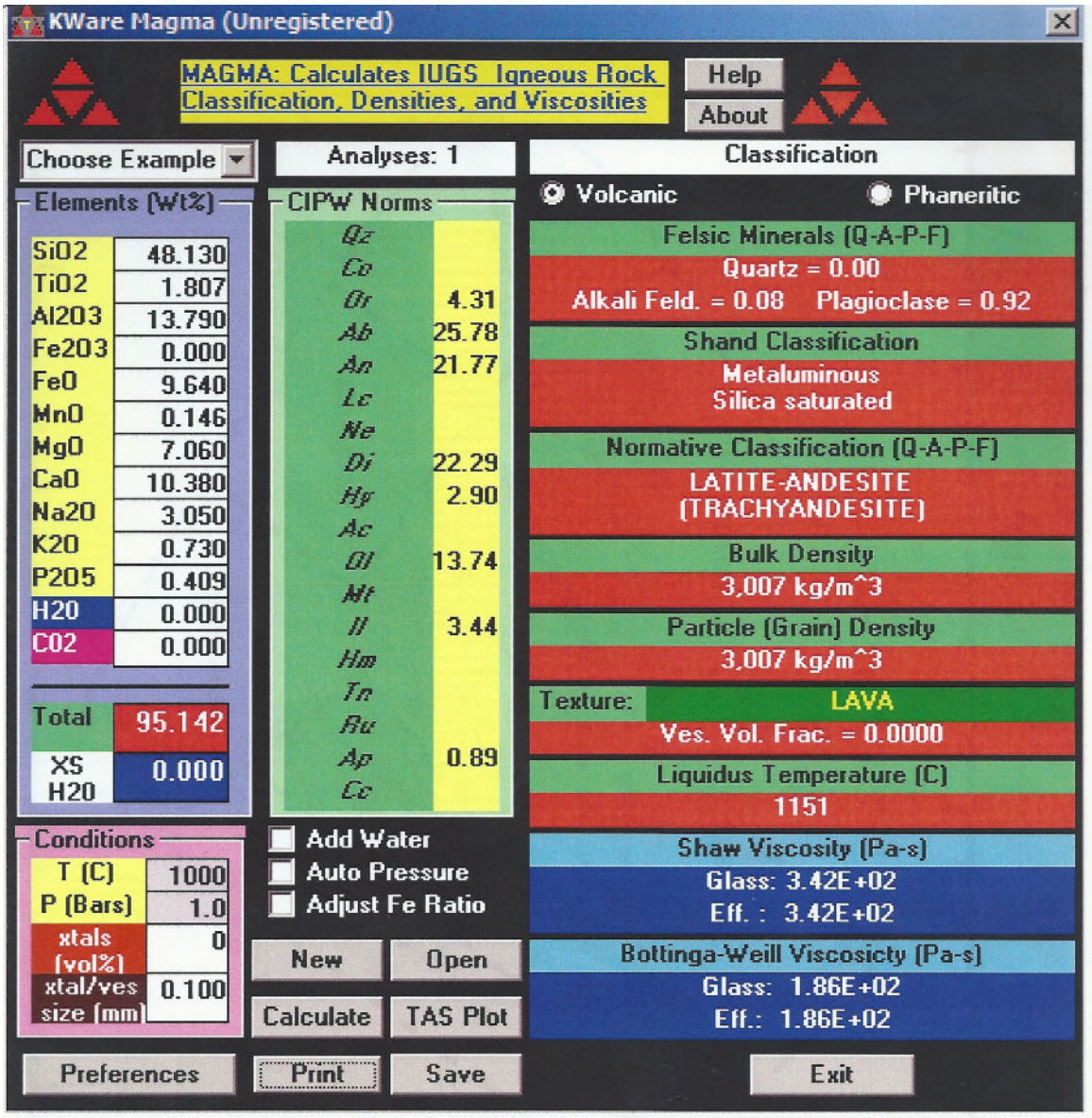
Sample number S-06-159



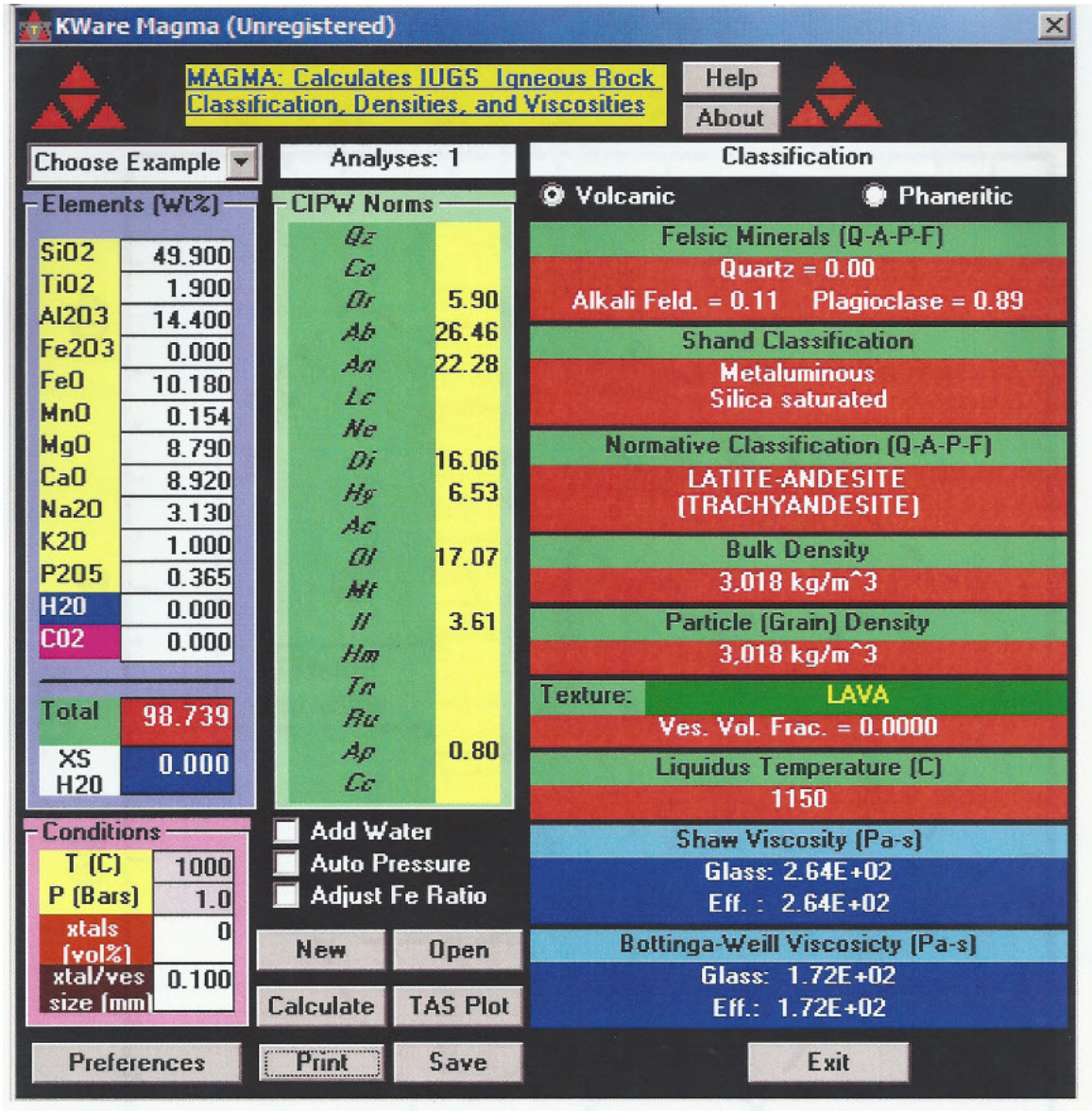
Sample number S-06-162



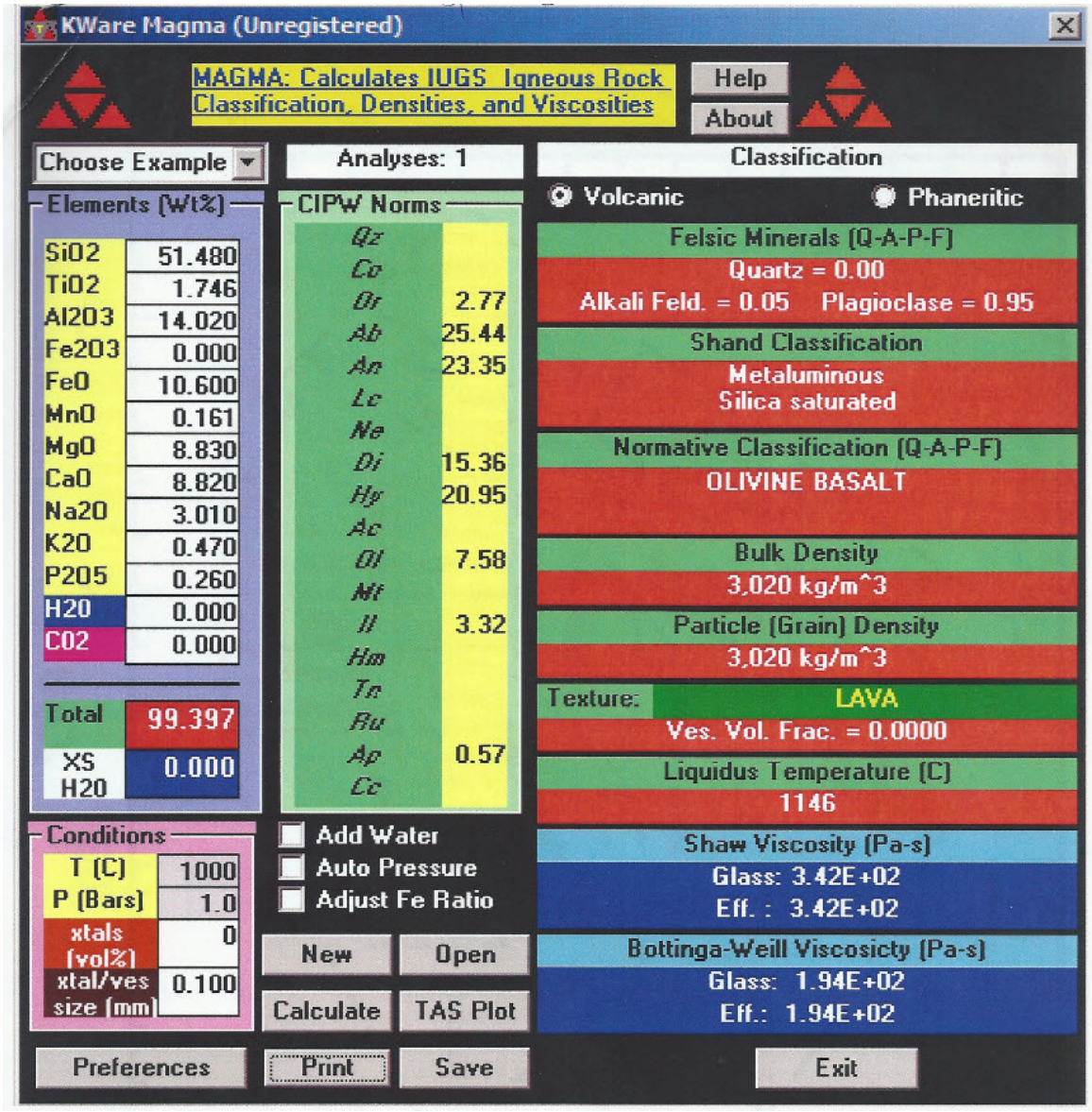
Sample number S-06-163A



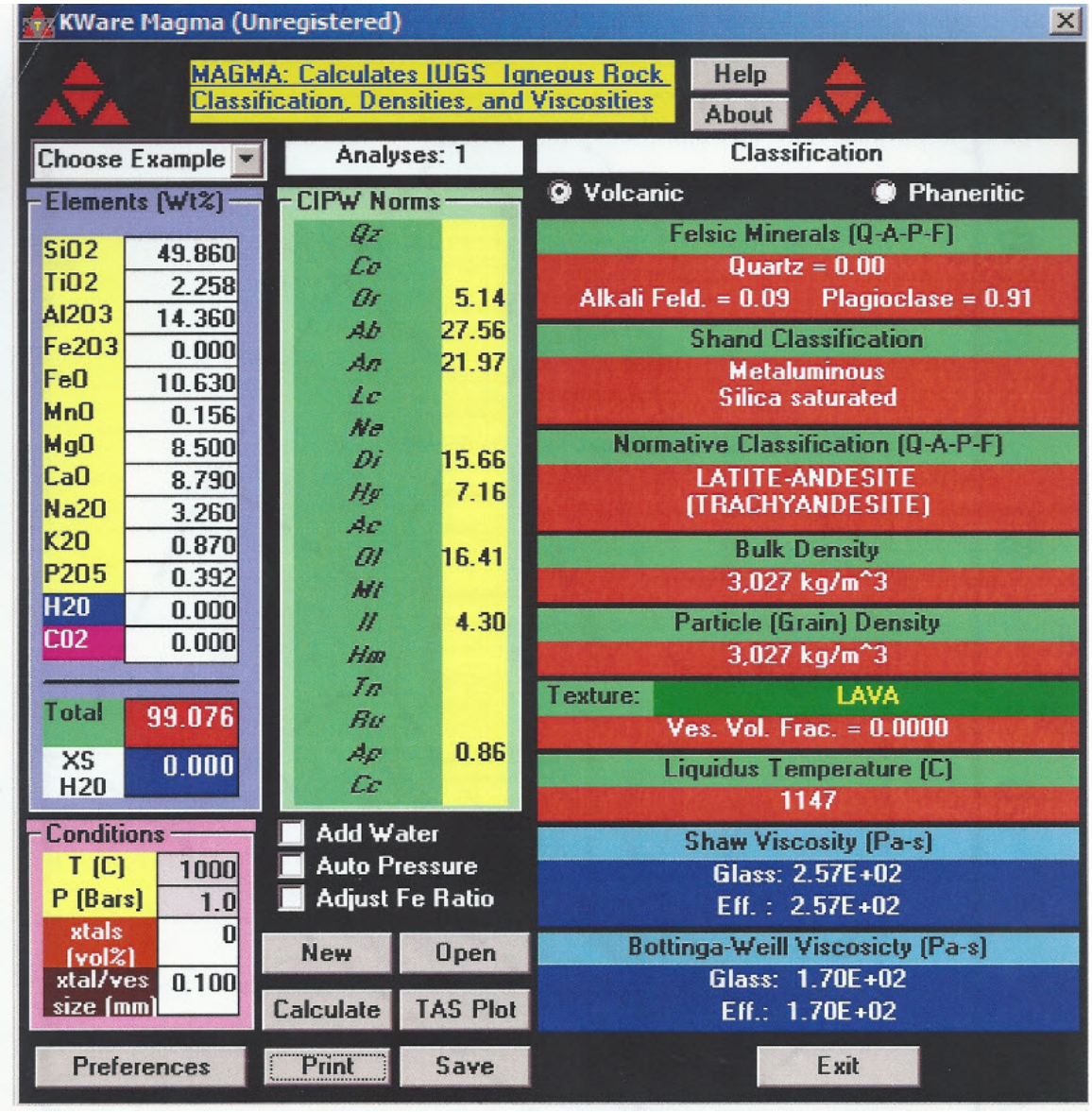
Sample number S-06-164



Sample number S-06-165



Sample number S-06-168



Sample number QUARRY-1

